APPLICATION OF COMPUTATIONAL FLUID DYNAMICS TO AEROSOL

SAMPLING AND CONCENTRATION

A Dissertation

by

SHISHAN HU

Submitted to the Office of Graduate Studies of
Texas A&M University
in partial fulfillment of the requirements for the degree of

DOCTOR OF PHILOSOPHY

May 2007

Major Subject: Mechanical Engineering

APPLICATION OF COMPUTATIONAL FLUID DYNAMICS TO AEROSOL

SAMPLING AND CONCENTRATION

A Dissertation

by

SHISHAN HU

Submitted to the Office of Graduate Studies of
Texas A&M University
in partial fulfillment of the requirements for the degree of

DOCTOR OF PHILOSOPHY

Approved by:

Co-Chairs of Committee,	Andrew R. McFarland
	Yassin A. Hassan
Committee Members,	Hamn-Ching Chen
	John S. Haglund
Head of Department,	Dennis O'Neal

May 2007

Major Subject: Mechanical Engineering

ABSTRACT

Application of Computational Fluid Dynamics to Aerosol Sampling and Concentration.

(May 2007)

Shishan Hu, B.S., Tsinghua University; M.S., Tsinghua/Shantou University

Co-Chairs of Advisory Committee: Dr. Andrew R. McFarland
Dr. Yassin A. Hassan

An understanding of gas-liquid two-phase interactions, aerosol particle deposition, and heat transfer is needed. Computational Fluid Dynamics (CFD) is becoming a powerful tool to predict aerosol behavior for related design work. In this study, FLUENT 6 is used to analyze the performance of aerosol sampling and concentration devices including inlet components (impactors), cyclones, and virtual impactors.

The $k - \omega$ model was used to predict particle behavior in Inline Cone Impactor (ICI) and Jet-in-Well impactor (JIW). Simulation provided excellent agreement with experimental test results for a compact ICI. In the JIW, compound impaction is shown to cause the device to have a smaller cutpoint Stokes number than the single impaction unit. The size ratio of the well-to-jet was analyzed to find its influence on the total and side collections.

Simulation is used to analyze liquid film, flow structure, particle collection, pressure drop, and heating requirements for a bioaerosol sampling cyclone. A volume of fluid model is used to predict water film in an earlier cyclone. A shell-volume is

developed to simulate thin liquid film in large device. For the upgraded version cyclone, simulation is verified to successfully predict cutpoint and pressure drop. A narrowing-jet is shown to describe the flow evolution inside the axial flow cyclone. Turbulent heat transfer coefficients and surface temperatures are analyzed and heaters are designed for this cyclone. A double-outlet cyclone was designed and its pressure drop decreased about 25%, compared with a single-outlet cyclone. A scaled-down 100 L/min cyclone was also designed and tested based on the 1250 L/min unit.

CFD is used to design a Circumferential Slot Virtual Impactor (CSVI) which is used for concentration of bioaerosol particles. Simulations showed a 3-D unstable flow inside an earlier version CSVI, which could explain acoustic noise and particle loss observed in the experiment. A smaller CSVI unit was designed using simulation and its flow was shown to be stable. CFD was then used to analyze the wake flow downstream of the posts to reduce particle losses and eliminate flow instabilities caused by wakes. A successful solution, moving the posts outside was developed by the use of CFD.

DEDICATION

I would like to dedicate this work to all the members of my family. My parents and my older brothers and sister worked hard for many years to support my education and imprinted on me a fundamental rule of life: to act like a gentlemen who is as pure water and to be knowledgeable like a grand tree. My wife married me when I had just graduated from college. Her love and encouragement has accompanied and supported me with happiness and conformance, which allowed us to pursue our dreams together and to make an attempt to pursue a higher education in this country.

ACKNOWLEDGEMENTS

TABLE OF CONTENTS

LIST OF TABLES

LIST OF FIGURES

FIGURE   Page

FIGURE   Page

NOMENCLATURE AND ABBREVIATIONS

NOMENCLATURE

A	Surface area of particle
ALR	Ratio of mass of air to water
B_i	Biot number
$C_{1\varepsilon}$, $C_{2\varepsilon}$, C_μ, σ_k, σ_ε	Constants in $k-\varepsilon$ turbulent model
C_c	Cunningham's correction
C_D	Drag force coefficient for particles
D_h	Hydraulic diameter
C_L	Constant used in Discrete Random Walk (DRW) model
C_p	Specific heat
$D_{0.5}$	Cutpoint which is defined as aerodynamic diameter of particle for which the minor flow transmission efficiency is 50%
D_C	Cone diameter used in Inline Impactor
D_i	Inlet tube diameter
D_j	Nozzle diameter at the jet exit
D_{mp}	Mean particle size
d_p	Particle diameter
D_W	Well diameter used in Jet-in-Well Impactor
Do	Outlet tube diameter

E Total internal energy

f Minor flow ratio in CSVI, which is defined as minor flow rate, $\dot{Q}_i$, divided by the total flow rate $\dot{Q}_t$, $f = \dot{Q}_i / \dot{Q}_t$. Also, the symbol is used to represent the friction factor in heat transfer calculation

g Gravity

h Heat transfer coefficient

i Heat flux. Also, symbol is used to represent turbulent intensity

k Turbulent kinetic energy

K Thermal conductivity. Symbol is also used to represent the pressure coefficient

K_a Thermal conductivity of air, 0.022W/(m·K)

k_t Turbulent thermal conductivity

K_w Thermal conductivity of water, 0.58 W/(m·K)

L Width of an air pathway

L_C Characteristic length

L_e Eddy length scale

$\dot{m}_a$ Mass flow rate of air from an air needle

$\dot{m}_w$ Mass flow rate of water from a water needle

N_u Nusselt number

p Static pressure

Pr   Prandtl number of air, 0.69

$\dot{Q}_i$ Minor flow ratio in CSVI

$\dot{Q}_t$ Total flow ratio of CSVI

R Radius towards the axis of CSVI

R_C Critical zone radius of CSVI. Also symbol is used to represent the radius of cyclone body

Re Reynolds number defined as $\mathrm{Re} = \dfrac{\rho_a U L_C}{\mu}$

Re_P Particle Reynolds number

Re_r Relative Reynolds number of a particle

Re_t Turbulent Reynolds number

R_i Fillet radius in the receiver section of CSVI

R_O Radius of exhaust tube from minor flow region in CSVI

R_v Radius of vortex finder

S Stopping distance of a particle. Symbol also used to represent the clearance distance between the jet and the collection plate of a classical impactor.

S_{ij} Mean strain tensor

Stk Particle Stokes number defined as $Stk = \dfrac{C_c \rho_P U_i D_p^2}{9 \mu W}$

$Stk_{0.5}$	Cutpoint Stokes number
t	Time
T	Temperature
T_a	Air temperature
T_o	Initial temperature
T_L	Fluid Lagrangian integral time
u	Local liquid velocity
u_i, u_j, u_k	Averaged component of the instantaneous velocity of fluid
u_i', u_j', u_k'	Fluctuation component of the instantaneous velocity of fluid
$\overline{u_i' u_j'}$	Reynolds stress
U	Averaged liquid velocity
U_a	Air velocity
v_P	Particle velocity
V	Volume of a particle
V_{aX}	X direction velocity component of air out of an air needle
V_{XO}	Initial velocity in the X direction of the water droplets after atomization
V_{WX}	X direction velocity component of water fluxing from a water needle
W	Width of a jet
W_1	Slot width of acceleration nozzle of a CSVI
W_2	Receiver slot width of a CSVI

y	Distance from the wall
y^+	Dimensionless distance from the wall
α_q	Volume fraction for each phase (q)
χ	The ratio of well diameter to jet diameter in the jet-in-well impactor
ε	Dissipation rate of turbulent kinetic energy
η	Efficiency
ϕ_D	Particle drag force parameter
λ	Molecular mean free path
μ	Dynamic viscosity of the fluid
μ_a	Dynamic viscosity of air, 0.00018 Pa·s
μ_t	Turbulent viscosity of the fluid
μ_w	Dynamic viscosity of water, 0.001 Pa·s
ν	Kinematic viscosity of a fluid
θ	Angle
ρ	Liquid density
ρ_P	Particle density
ρ_a	Air density, 1.2 kg/m^3
ρ_w	Water density, 1000 kg/m^3
σ	Water surface tension, 0.073 kg/s^2
τ_e	Eddy lifetime

$\overset{=}{\tau}$	Stress tensor
τ	Particle relaxation time
τ_{cross}	Particle crossing time in turbulent eddies
ω	Specific dissipation rate of turbulent kinetic energy
ψ	Shape factor of a particle
ζ	A normally distributed random number

ABBREVIATIONS

AD	Aerodynamic diameter of particle
CFD	Computational fluid dynamics
CSVI	Circumferential slot virtual impactor
CYC	Cyclone
DNS	Direct numerical simulation
DPM	Discrete phase model
ICI	Inline cone impactor
JIW	Jet-in-well impactor
LES	Large eddy simulation
LSVI	Linear slot virtual impactor
PSN	Particle saturated number
RANS	Reynolds-Averaged Navier Stokes equation
RWM	Random walk model

CHAPTER I

INTRODUCTION

A bioaerosol system generally includes three major components: an inlet, a concentrator or collector, and a detector or identifier. Typically the particle size range of interest in bioaerosol sampling is 1 to 10 μm AD, which may consist of single spores, clusters of organisms, or amorphous particles. The function of an inlet is to aspirate sampled air at a desired flow rate and to remove undesirable large particles such as large dust particles or other debris that could degrade the performance of the collector/concentrator or detector/identifier systems. The concentrator increases the aerosol concentration in the size range of interest, so that either a lower detection level can be achieved, or a given level could be detected with greater reliability. The collector serves the function of depositing the aerosol in a manner that provides compatibility with the detector/identifier. Sometimes the collection and concentration roles are combined into a single function, as with a wetted-wall cyclone, where the cyclone will take in aerosol at a particular flow rate and deliver the particles as a hydrosol, but with the liquid flow rate being on the order of 10^{-5} to 10^{-6} of the air. The detector or identifier processes the sample and provides a signal that either indicates the presence of a bioaerosol (detector) or indicates the specific biological material that has been sampled (identifier). In this study, the focus is on the sampling, concentrating, and collecting of bioaerosol to

_____

This thesis follows the style of *Aerosol Science and Technology.*

the exclusion of detection and identification, with the emphasis of sampling being related to scalping large, unwanted particles from the aerosol size distribution.

Bioaerosol inlet fractionators and concentrators/collectors generally belong to the mechanical applications related to fluid mechanics and use the principle of inertial separation of the aerosols. Essentially the processes are two-phase flow applications that study the discrete phase particles in a continuous phase fluid. Some special aspects of this two-phase flow include small particles with sizes on the order of micrometers and dilute particle concentration, which imply a one-way coupling effect, i.e. the discrete phase particles have no influence on the continuous phase fluid.

To meet the requirements for the design of the inlet fractionators and concentration devices, Computational Fluid Dynamic (CFD) can be a powerful tool to analyze the performance of the device, filter out possible problems, and optimize the design. Accompanying the fast development of computer science and technology, the models in CFD are improved for different applications such as flow field calculations and particle trajectory calculations, etc., providing detailed descriptions of flow velocity, pressure distribution, particle behavior, total collection, and flow evolution in an unsteady state. From laminar to turbulent, from single-phase to multiphase flow, from steady to unsteady, from conduction to convection, CFD can be used to analyze a wide range of applications in aerosol research.

CFD applications include two major calculations for different objectives. The first calculation is common to all studies, which is to calculate the continuous phase flow based on an Eulerian reference frame. Fluid characteristics are calculated in this step,

including velocity, pressure, and turbulence features if the flow is turbulent. The second calculation is to apply the results of the first calculation in conjunction with the appropriate model for the application being studied. For example, the Discrete Phase Model (DPM) may be used to calculate the particle behavior in a Lagrangian reference frame to track their locations in the simulated domain, and thus determine whether or not the particles are collected. The Volume of Fluid (VOF) model can be used to calculate the liquid film evolution in a wetted-wall cyclone, and conduction and convection models may be used to calculate the temperature response when the cyclone is used to sample cold air.

In this study, a commercially available software package, FLUENT 6, together with Gambit (FLUENT's mesh generation software) is used to model bioaerosol sampling system designs which include three different types of devices: inlet fractionators, cyclones, and circumferential slot virtual impactors (CSVI's). Papers have been published that verify FLUENT models can provide reasonable results for simulations related to those reported herein, including turbulent flow, particle trajectories, heat transfer, and liquid films (Yang *et al* 2006, Burwash *et al* 2006, Ataki and Bart 2004) etc.

This dissertation includes six (6) chapters and some auxiliary sections to complete an integrated study. Chapter I introduces the background, objectives, and developments of the bioaerosol sampling system. Chapter II gives a brief introduction to FLUENT and Gambit. Some basic models of CFD, which were used in the applications of this study, are discussed. The Gambit mesh generation strategy, technical skills, and

considerations are introduced for different application domains and flow conditions, especially for turbulent flow in a complex geometry. The FLUENT flow models include different turbulent models and the laminar model, VOF, DPM, and heat transfer. Boundary setting for FLUENT simulation cases is also introduced and its influence is discussed. Finally, methodology discrepancies, between numerical simulations and experimental tests, are discussed and possible solutions are suggested to improve the accuracy of numerical predictions for some applications.

Chapter III introduces the CFD design for air sampling fractionators, which include an Inline Cone Impactor (ICI) and a Jet-in-Well Impactor (JIW). A compact size ICI is designed using a $k - \omega$ turbulent model, and its performance is experimentally verified. For the JIW design, secondary impaction is taken into account, which can result in a much smaller cutpoint Stokes number compared to a traditional impactor.

Chapter IV describes the approaches for the design of some bioaerosol sampling cyclones using CFD techniques. Four (4) bioaerosol sampling cyclones are introduced focusing on different objectives. For an earlier 780 L/min cyclone, the VOF model is used to analyze the liquid evolution near the skimmer and a special cut-shell strategy is introduced. For an upgraded 1250 L/min unit, a Reynolds Stress Model (RSM) together with DPM is used to predict the performance of the cyclone. A narrowing-jet inward-spiral-flow structure is found in the cyclone, which is used to explain why the collection is restricted to a small region of the cyclone near the flow inlet and why the observed cutpoint Stokes number is small. Heaters are designed for this cyclone using turbulent heat transfer models and a fluid-metal separate meshing strategy is introduced for steady

and unsteady studies. A double-head cyclone is also designed to achieve lower pressure loss, where the loss in the double-head device is about 75% of the normal cyclone. Lastly, a small scaled 100 L/min cyclone is designed, which will have a cutpoint of about 1 μm AD and a pressure loss of less than about 1250 Pa (5 inches of water).

Chapter V presents simulations on circumferential slot virtual impactors (CSVI) with flow rates of 10 L/min and 100 L/min. Prediction of the performance for CSVI is conducted and verified for the 10 L/min CSVI unit which has a dynamic range of about 100X. For an earlier 100 L/min CSVI unit, steady and unsteady CFD studies are conducted to analyze a pulsing noise and low minor flow fraction efficiency observed in the experiment of the unit. CFD is also used to simulate the wake flow caused by the posts which degrades the minor flow fraction efficiency. Possible reasons are analyzed and solutions are suggested to improve the flow stability and unit efficiency, and those objectives are met through the use of the CFD design. Axisymmetric CSVI and planer-symmetric linear slot virtual impactor (LSVI) are compared in CFD and the former is found to be essentially more stable. Chapter VI gives a summary of the presented works and some possible future study topics that make use of CFD.

CHAPTER II

CFD TECHNIQUE: THEORETICAL MODEL AND APPLICATION

2.1 FLUENT: Basic Function and Application

There are several major commercial CFD software packages available now including FLUENT, CFX, and Star CD, etc. Generally these packages can provide basic functions about flow calculation, particle trajectory, and other applications based on different mathematical models and mesh generation strategies.

FLUENT (FLUENT Inc., Lebanon, New Hampshire, USA) can provide a wide range of mathematical models for different physical transport problems like heat transfer, combustion, particle mixing, etc., in certain geometries, and it can be applied in various categories like mechanical, nuclear, civil, and chemical, etc. The flow in FLUENT study can be compressible or incompressible, laminar or turbulent, single phase or multiphase, and the geometry can be a simple tube or a complex domain. Also it can use various types of boundaries such as porous media, solid wall, moving or periodic, etc. in steady or unsteady flow fields. FLUENT also provides a power set of geometry and data post-processing tools to analyze interested physical parameters on certain locations in the simulated geometry which can enhance the comprehensive process of people to understand the physical phenomenon.

GAMBIT is the part in the package for mesh generation and it provides robust functions for 2D and 3D applications to treat line, surface, and volume. Structured and unstructured meshes are supported by GAMBIT with different kinds of cells, which can

be a mixed type if needed. Multi-blocks can be used in the mesh to control the number of cells in complex geometries and to match the physics of the various flow properties in different regions and zones. Both axisymmetric and planner-symmetric schemes are available in 2D meshing. GAMBIT can also exchange drawings with the third-part software like AutoCAD which makes it possible to simulate extremely complex geometries that can be prepared by other software and be imported into GAMBIT.

The general process of numerical simulations includes two major steps, i.e., mesh generation in GAMBIT and model application and calculation in FLUENT. Mesh generation is the first step of the simulation using GAMBIT. Grid independence can be verified by adjusting the cell numbers of the mesh for the laminar flow by increasing the cells step by step. When the flow is turbulent, there are some special requirements for the near wall cells in the mesh generation depending on the models to be used for flow calculation such as RANS or LES. The Reynolds numbers are important to preliminarily understand flow conditions and to create the computational mesh. For RANS, turbulent models used together with a wall function, it is important that the first cell size (FL) for wall-adjacent cells, which is defined as the distance between the cell centroid and the wall, is chosen to appropriately satisfy the y^+ requirement within a range of about 30 to 60 in which the log-law function is valid (Fox et al., 2005) for the Standard or Non-equilibrium wall functions. RANS model with the Enhanced wall function and $k - \omega$ require the y^+ to be about 1 for the near wall cells. The dimensionless distance, y^+, is defined as:

$$y^+ = \frac{yu^*}{\upsilon} \tag{1}$$

The parameter y is the distance from the wall, υ is the kinematic viscosity of air, and u^* is the friction velocity (Fox et al., 2005). In the log-law region, the first cell should not be too small to prevent it being placed in the viscous sub-layer or the encompassing buffer region. Also, there should be a few cells inside the boundary layer so the first cell cannot be too coarse.

In the second step, an essential task is to resolve the conservation equations of flow mass and momentum to obtain the velocity and pressure fields in the domain. After that, other models can be started using this basis of velocity and pressure distribution for different applications.

The general form of the conservation of mass equation used in FLUENT is:

$$\frac{\partial \rho}{\partial t} + \nabla \cdot (\rho \vec{u}) = S_m \tag{2}$$

Here, S_m is the source term of the mass in case it can be transferred from other phases or resources like condensation.

The conservation of momentum equation in an inertial reference frame used in FLUENT is:

$$\frac{\partial}{\partial t}(\rho \vec{u}) + \nabla \cdot (\rho \vec{u} \vec{u}) = -\nabla p + \nabla \cdot (\overline{\overline{\tau}}) + \rho \vec{g} + \vec{F} \tag{3}$$

Here, p is static pressure of the fluid; $\overline{\overline{\tau}}$ is stress tensor, $\vec{g}$ corresponds to the gravitational body force and $\vec{F}$ is external force acting on the fluid.

The stress tensor $\overline{\overline{\tau}}$ describes the stretching and twisting effect of the fluid and it is given by:

$$\overline{\overline{\tau}} = \mu[(\nabla \vec{u} + \nabla \vec{u}^T) - \frac{2}{3} \nabla \cdot \vec{u}I] \qquad (4)$$

Here, μ is fluid viscosity and I is the unit tensor.

When the flow is turbulent in the study, the item of fluid velocity $\vec{u}$ will consist of a fluctuation character and the conservation equations need special models to simplify the application which is discussed in the next section.

2.2 Turbulent Models

Flow fluctuations are a special feature of turbulent flow and they can cause mixing and coupling of the physical transported properties of the fluid like momentum, energy, and concentration. Fluctuations of the fluid have different length and time scales that depend on the strength of the turbulence and generally its length scale is very small, about $O(10^{-3})$ of the characteristic geometric length scale. This makes it nearly impossible to calculate the exact flow field by solving the instantaneous governing equations with the current computational apparatus. That approach, Direct Numerical Simulation (DNS), can only resolve some cases with simple geometries and low Reynolds flows. However, the instantaneous governing equations are simplified based on some special assumptions or empirical models to obtain solutions for a large range of engineering applications.

One of the simplifications is the Reynolds-Averaged Navier-Stokes (RANS) equations in which the instantaneous fluid variables are decomposed into two

components, an average part and a fluctuation part using a time-averaged or ensemble-averaged concept, i.e.:

$$\tilde{\phi} = \phi + \phi'$$ (5)

Here, $\tilde{\phi}$ represents any instantaneous fluid variable such as velocity, pressure, energy, species concentration, temperature, or other scalar, ϕ and ϕ' represent the time-averaged and fluctuation components of $\tilde{\phi}$. An important assumption for the Reynolds-averaged approach is that the averaged fluctuation component is zero, i.e.:

$$\overline{\phi'} = 0$$ (6)

Substituting the instantaneous items with the averaged and fluctuation component and applying Equation (5), the mass and momentum conservation equations for incompressible flow become the following RANS equations:

$$\frac{\partial \rho}{\partial t} + \frac{\partial}{\partial x_i}(\rho u_i) = 0$$ (7)

$$\frac{\partial}{\partial t}(\rho u_i) + \frac{\partial}{\partial x_j}(\rho u_i u_j) =$$

$$-\frac{\partial p}{\partial x_i} + \frac{\partial}{\partial x_j}\left[\mu(\frac{\partial u_i}{\partial x_j} + \frac{\partial u_j}{\partial x_i} - \frac{2}{3}\delta_{ij}\frac{\partial u_l}{\partial x_l})\right] + \frac{\partial}{\partial x_j}(-\rho\overline{u_i'u_j'})$$ (8)

Here, the new term $-\rho\overline{u_i'u_j'}$, is called Reynolds stress which is generated by the coupling of the fluctuation components themselves with the mean flow. Different turbulent models such as $k-\varepsilon$, $k-\omega$, and the Reynolds Stress Model (RSM) are used

to simplify the Reynolds stress terms and to obtain closure of the RANS equations. The $k-\varepsilon$ or $k-\omega$ models each use some turbulent variables to characterize the turbulent features such as turbulent kinetic energy, k, dissipation rate of turbulent kinetic energy, ε, and specific dissipation rate, ω. The RSM model uses four (2D) or nine (3D) transport equations to calculate the Reynolds stresses using some other models.

The $k-\varepsilon$ model uses an assumption that the flow is fully turbulent which implies a high Reynolds number turbulent flow. Transportation equations for the standard $k-\varepsilon$ model are:

$$\frac{\partial}{\partial t}(\rho k)+\frac{\partial}{\partial x_i}(\rho k u_i)=\frac{\partial}{\partial x_j}\left[(\mu+\frac{\mu_t}{\sigma_k})\frac{\partial k}{\partial x_j}\right]+G_k-\rho\varepsilon \tag{9}$$

$$\frac{\partial}{\partial t}(\rho\varepsilon)+\frac{\partial}{\partial x_i}(\rho\varepsilon u_i)=\frac{\partial}{\partial x_j}\left[(\mu+\frac{\mu_t}{\sigma_\varepsilon})\frac{\partial\varepsilon}{\partial x_j}\right]+C_{1\varepsilon}\frac{\varepsilon}{k}G_k-C_{2\varepsilon}\rho\frac{\varepsilon^2}{k} \tag{10}$$

Here, G_k is the generation of turbulent kinetic energy which is transferred from the mean velocity gradient and defined as:

$$G_k=-\rho\overline{u_i'u_j'}\frac{\partial u_j}{\partial x_i} \tag{11}$$

Using the Bossinesq hypothesis, G_k can be evaluated as

$$G_k=2\mu_t S_{ij}S_{ij} \tag{12}$$

Here, S_{ij} is the mean strain tensor and μ_t is the turbulent viscosity which is calculated from:

$$\mu_t=\rho C_\mu\frac{k^2}{\varepsilon} \tag{13}$$

Here, C_μ is a constant, σ_k and σ_ε are turbulent Prandtl numbers for k and ε; $C_{1\varepsilon}$, $C_{2\varepsilon}$, and $C_{3\varepsilon}$ are constants. The constants are determined from experiments, and in FLUENT, their default values are:

$$C_{1\varepsilon} = 1.44, \ C_{2\varepsilon} = 1.92, \ C_\mu = 0.09, \ \sigma_k = 1.0, \ \sigma_\varepsilon = 1.3$$

A special application feature for using the standard $k-\varepsilon$ model and two modified versions provided in FLUENT, are that the $k-\varepsilon$ model only calculates the internal region of the flow domain and it uses a wall function for the near-wall cells, which means that the near-wall cells use other empirical models for the calculations. This is different than the two-equation $k-\omega$ models, which calculates the whole flow throughout the domain and does not use a wall function. This results in a different requirement for the meshing, where $k-\omega$ needs very fine cells near the wall but $k-\varepsilon$ can use much coarser ones because of the wall function.

The $k-\omega$ model uses k and ω as the turbulent variables in the calculation. The standard transport equations are:

$$\frac{\partial}{\partial t}(\rho k) + \frac{\partial}{\partial x_i}(\rho k u_i) = \frac{\partial}{\partial x_j}\left[(\mu + \frac{\mu_t}{\sigma_k})\frac{\partial k}{\partial x_j}\right] + G_k - Y_k \tag{14}$$

$$\frac{\partial}{\partial t}(\rho \omega) + \frac{\partial}{\partial x_i}(\rho \omega u_i) = \frac{\partial}{\partial x_j}\left[(\mu + \frac{\mu_t}{\sigma_\omega})\frac{\partial \omega}{\partial x_j}\right] + G_\omega - Y_\omega \tag{15}$$

Here, G_k and G_ω, Y_k and Y_ω represent the generation and dissipation of k and ω, respectively and they can be calculated from related models.

$$G_\omega = \alpha \frac{\omega}{k} G_k \tag{16}$$

Here, α is a coefficient calculated from the turbulent Reynolds number Re_t:

$$\text{Re}_t = \frac{\rho k}{\mu \omega} \tag{17}$$

The RSM models the individual Reynolds stresses and it can provide detailed calculations and information for each $-\rho \overline{u_i' u_j'}$ term in the case of anisotropic turbulent flows. Similar to the $k - \varepsilon$ model, the RSM uses wall functions for the near-wall cells. The transport equations are shown below and each item in the equation needs some assumptions and modeling.

$$
\begin{aligned}
&\frac{\partial}{\partial t}(\rho \overline{u_i' u_j'}) + \frac{\partial}{\partial x_k}(\rho u_k \overline{u_i' u_j'}) = -\frac{\partial}{\partial x_k}\left[\rho \overline{u_i' u_j' u_k'} + \overline{p(\delta_{kj} u_i' + \delta_{ik} u_j')}\right] \\
&+ \frac{\partial}{\partial x_k}\left[\mu \frac{\partial}{\partial x_k}(\overline{u_i' u_j'})\right] - \rho(\overline{u_i' u_k'}\frac{\partial u_j}{\partial x_k} + \overline{u_j' u_k'}\frac{\partial u_i}{\partial x_k}) + \overline{p(\frac{\partial u_i'}{\partial x_j} + \frac{\partial u_j'}{\partial x_i})} - 2\mu \overline{\frac{\partial u_i'}{\partial x_k}\frac{\partial u_j'}{\partial x_k}}
\end{aligned}
\tag{18}
$$

2.3 Particle Trajectory Calculations

Particle trajectories are calculated from the use of the Discrete Phase Model (DPM) in the Lagrangian frame after the flow field is calculated. In the simulation, it is assumed that particle concentration is dilute and particles have no influence on continuous-phase air flow, i.e., it is a one-way coupling simulation. Air flow will act on particles and determine their motion but air flow will not be affected by particles.

The mean trajectory or Discrete Random Walk model (DRW) will be selected depending on particle size and flow conditions. In the mean trajectory calculation, only the mean velocity of the air is used in the DPM model. When DRW is used, a Gaussian distributed random velocity fluctuation is artificially created to act on the particles together with the other forces. When the turbulent dispersion effects are important compared to the other forces (e.g., centrifugal) and the particle size (or Stokes number)

is large, the DRW model should be used. When particle sizes are small and the effects of turbulent dispersion are not dominant, mean trajectories can be used to determine the aerosol particle paths.

2.3.1 Mean Trajectory Calculation

In the mean trajectory calculation, the temporal mean velocities are used in the equation of motion for calculating the particle paths, viz:

$$\frac{d\bar{v}_P}{dt} = \phi_D(\bar{u} - \bar{v}_p) + \bar{g} + \vec{F} \tag{19}$$

$$\frac{d\bar{x}}{dt} = \bar{v}_P \tag{20}$$

Here, $\bar{v}_P$ is the particle velocity; $\bar{u}$ is the fluid velocity; $\bar{g}$ is the gravitational acceleration $\vec{F}$ is other external forces per unit mass, $\bar{x}$ is the position of the particle, $\phi_D(\bar{u} - \bar{v}_p)$ is the drag force per unit mass. The latter term is:

$$\phi_D = \frac{18\mu}{C_c \rho_P d_p^2} \frac{C_D \, \text{Re}_r}{24} \tag{21}$$

$$\text{Re}_r = \frac{\rho \, d_p \left| \bar{v}_p - \bar{u} \right|}{\mu} \tag{22}$$

C_D is the drag force coefficient, which is determined by the relative Reynolds number of the particle. FLUENT provides two models for the calculation of C_D. One is the Morsi and Alexander model,

$$C_D = \alpha_1 + \frac{\alpha_2}{\text{Re}_r} + \frac{\alpha_3}{\text{Re}_r^2} \tag{23}$$

Here, α_1, α_2, and α_3 are constants.

A second model that can be used to calculate C_D is that of Haider and Levenspiel,

$$C_D = \frac{24}{\text{Re}_{SPH}}(1 + b_1 \text{Re}_{SPH}{}^{b_2}) + \frac{b_3 \text{Re}_{SPH}}{b_4 + \text{Re}_{SPH}} \tag{24}$$

Here,

$$b_1 = \exp(2.3288 - 6.4581\psi + 2.4486\psi^2)$$

$$b_2 = 0.0964 + 0.5565\psi$$

$$b_3 = \exp(4.905 - 13.8944\psi + 18.4222\psi^2 - 10.2599\psi^3)$$

$$b_4 = \exp(1.4681 + 12.2584\psi - 20.7322\psi^2 + 15.8855\psi^3)$$

where, ψ is a shape factor, which is defined as the ratio of the surface area s_{SPH} of a sphere having the same volume as the particle, over the exact surface area of the particle S_{PAR}.

$$\psi = \frac{S_{SPH}}{S_{PAR}} \tag{25}$$

For low Reynolds numbers (e.g., $Re < 1$), the Stokes-law can be used to calculate the drag force,

$$\phi_D = \frac{18\mu}{d_p^2 \rho_p C_c} \tag{26}$$

Here, C_c is the Cunningham correction for small particles which can be calculated from

$$C_c = 1 + \frac{2\lambda}{d_p}\left[1.257 + 0.4\exp(-\frac{1.1d_p}{2\lambda})\right] \tag{27}$$

and λ is the molecular mean free path.

The additional item $\vec{F}$ in Equation (19) could be forces in a rotating reference frame or electrostatic forces. A Saffman lift force could also be considered; however, in this study, the gravitational and drag force are the only external forces taken into account.

2.3.2 Turbulent Dispersion Calculation

When the flow is turbulent and the particle size is relatively large, the turbulent dispersion effect can affect the particle motion and may even dominate the particle trajectory determination. Turbulent flow is characterized by fluctuating velocities and eddies that have various length and time scales. The fluctuations and eddies are relatively strong near the wall where turbulent bursts are generated.

Friedlander and Johnstone (1957) originated a free-flight theory for particle motion in turbulent flow near a smooth wall. The general process is that the particles follow the larger eddies in the internal region and can obtain certain energy due to the turbulent velocity fluctuations. When the particles are thrown out from the larger eddies, they can move toward the wall with initial velocity and if the initial velocity is high enough, particles can reach the wall and become deposited. However, the principle of particle motion in turbulent flow is still to be understood and there is no exact accurate solution. For engineering applications, the Discrete Random Walk (DRW) model is used by FLUENT in a stochastic tracking approach to predict the particle motion. As shown by Equation (19), the instantaneous fluid velocity is required for the particle motion calculation, which consists of the mean velocity that can be obtained from the flow field calculation and the fluctuation component that needs to be modeled.

In the DRW model, the turbulent dispersion effect is calculated in the term of interaction between the particles and a succession of turbulent fluid eddies. The eddy is described by a Gaussian distributed random velocity fluctuation and a time scale. Generally, the random velocity fluctuation can be calculated using the local RMS value

of the velocity fluctuations or turbulent kinetic energy, which is determined after the

flow is calculated.

$$u^{'} = \zeta\sqrt{\overline{u'^2}} \ , \ v^{'} = \zeta\sqrt{\overline{v'^2}} \ , \ w^{'} = \zeta\sqrt{\overline{w'^2}} \tag{28}$$

Here, ζ is a normally distributed random number used to generate the fluctuation

velocity. When the turbulent flow is isotropic, then turbulent kinetic energy can be used

in the calculation.

$$\sqrt{\overline{u'^2}} = \sqrt{\overline{v'^2}} = \sqrt{\overline{w'^2}} = \sqrt{2k/3} \tag{29}$$

The eddy lifetime can be calculated from (Shirolkar *et al.* 1996, FLUENT

Documentation 2005):

$$\tau_e = 2T_L \text{ or } \tau_e = -T_L \log(r) \tag{30}$$

In this equation, the eddy lifetime either uses the constant 2 for isotropic flow or uses a

Random Eddy Lifetime by involving a uniform random number r, $r \in [0,1]$. T_L is the

fluid Lagrangian integral time scale, which is determined by the particle inertia and

describes a time during which the particle could maintain its original velocity before it

changes velocity and migrates to another eddy. For small particles which are assumed to

have shorter relaxation times than the time scales of all eddies in the turbulent flow, T_L

can be calculated from:

$$T_L = C_L \frac{k}{\varepsilon} \tag{31}$$

Where C_L is about 0.15 for $k - \varepsilon$ and $k - \omega$ models and 0.30 for the RSM model.

The interaction time $\tau_{\text{int} eraction}$ for a particle crossing through an eddy is

determined by the eddy lifetime τ_e and the particle crossing time, τ_{cross} .

$$\tau_{cross} = -\tau \ln\left[1 - \frac{L_e}{\tau|u - v_p|}\right] \tag{32}$$

$$\tau_{int\,eraction} = \min(\tau_e, \tau_{cross}) \tag{33}$$

Here, L_e is the eddy length scale and τ is the particle relaxation time. The smaller value

of τ_e and τ_{cross} are used for the interaction time. After the interaction time is reached,

the instantaneous velocity is calculated using a new ζ.

2.3.3 Considerations for DPM Applications

When the DPM is used to calculate the particle trajectories, some conditions need

to be set including the number of particles, release locations, initial particle velocities,

particle density, etc.

The particle density can be assigned based on the exact density of the particles

used in the experiment. However, the density is usually chosen to be that of liquid water

so the size of the spherical particles will be the aerodynamic diameter. The density of the

particles generally is close to the liquid water for most applications and the effect of

density is not significant to the calculation.

The initial velocity of the particles can be set to zero or the same as the air

velocity at the release location. The particle stopping distance in this study is short at the

release location and the particles will follow the air so the historical velocity behavior of

the particles disappears quickly, i.e., the initial velocity of the released particles has little

effect on the final results.

Generally, a uniform distribution of the particles is used at the inflow boundary.

If more particles are to be used in particle trajectory calculations to provide better spatial

resolution, they are also distributed uniformly at the release location. However, a larger number of particles will increase the calculation time especially for RWM when the dispersion effect is considered. Similar to the process of demonstrating grid independence by increasing the number of cells, an increasing number of particles can be used in the particle trajectory calculation to demonstrate achievement of asymptotic behavior. The number of particles where this is achieved is called the Particle Saturated Number (PSN), above which the calculated results remain constant.

Hari (2003) discussed the PSN in a 2D laminar flow for an impactor and his results showed that there was almost no difference between releasing 100 and 500 particles. This suggests that a particle resolution of 100 on a line should be sufficient for particle trajectory calculation. For a plane release, a total number of 10,000 particles, which implies a distribution of 100 particles in both linear directions, will be sufficient in laminar flow calculations.

For the RWM that models the dispersion effect of turbulence, there are two aspects to consider regarding particle release and trajectory calculations. The problem regarding the number of particles is similar to that in laminar flow. Besides this number consideration, another aspect is that the calculation of RWM provides a random result in each time due to the Gaussian fluctuation velocity generation. The results can vary in a range of 25% for each calculation, which suggests that release at a point should be replicated and an average value could be used. Generally, sufficient accuracy is obtained if about 20 replicate releases are made at each location.

In most applications, the release location is the inlet surface, which is normally set to be a Velocity Boundary. The bounded inlet area could be a flat surface, a cylindrical surface, or a sphere. The wall surface downstream of the bounded inlet also varies and it could be a straight tube, a converging nozzle as in a virtual impactor, or a complex varying curved surface as in a cyclone. The inlet effect of the particle trajectory calculation could be a potential error in numerical simulation and result in up to about a 10% difference in the calculation especially for the inlet with a converging section as in a CSVI. This is due to several reasons, one is that near-wall cells are much larger than the particle size and the mesh may not capture the velocity gradient with sufficient resolution. The size ratio could be O (100) or even higher. Another reason is that the near-wall cells may not be fine enough to capture the air velocity gradient, which is rapidly changing in the boundary layer and the high gradient has an important effect on the particle motion in this region. In the model, to decide the particle trajectory the velocity of the air inside a cell is usually assigned to be the center value of the cell. It is well known that the velocity changes rapidly inside the boundary layer, which is very thin near the wall and the velocity gradient is very high in this region. The physics of the velocity property near the wall in the boundary layer may be lost if the center value of the near-wall cell is used and the calculation accuracy for particle motion would be low. One solution for this problem is to improve the resolution of the near-wall cells; however, it may increase the total number of cells and would make the mesh generation difficult. Another simplified approach is to artificially set a short section of the inlet wall to be REFLECT, i.e., not trapping particles and allow a longer distance for the particles

to follow the air and avoid non-physical impaction of the initial setting of the particle velocity. The final solution needs to use an interpolated velocity instead of the center value of the cell at the local position inside the near-wall cells to match the spatial velocity in the DPM model of FLUENT.

With reference to Figures 1 and 2, the effect of the size of the near-wall cell is simulated to compare the particle behavior in the inlet region. Here a CSVI unit is used that has an acceleration nozzle at the inlet section. Air is introduced into the CSVI through the inlet and accelerates in the nozzle. Two cases are simulated using different 2D meshes, a coarse mesh and a fine mesh with 20,000 and 50,000 structured cells, respectively. The averaged air velocity at the inlet is low, about 0.475 m/s, and 15 μm particles are released from the inlet to check the trajectories. Figures 1 and 2 show a different behavior of the 15 μm particles at the start section of the acceleration nozzle in the two meshes. In the 20K coarse mesh, some particles, about 10%, strike the curved nozzle as shown in Figure 1. In contrast, no particles reach the curved nozzle in the 50K fine mesh as shown in Figure 2. The result of the 50K mesh more readily shows that the particles could follow the mainstream air. The deposition in the 20K coarse mesh is caused by the large size of the near-wall cells where the velocity of the air is the center value of the near-wall cells and numerical artificial impaction is created. In the fine 50K mesh, the near-wall cells are of a very small size and can capture the rapidly changing velocity of the air in the boundary layer. In other words, the center velocity of the near-wall cell in the 50K fine mesh is much smaller than that in the coarse 20K mesh.

In some applications, it is difficult to use a sufficiently fine mesh to avoid accuracy problems. A better way is to use interpolation values of the air velocity inside the near-wall cells that need to be considered in the DPM model.
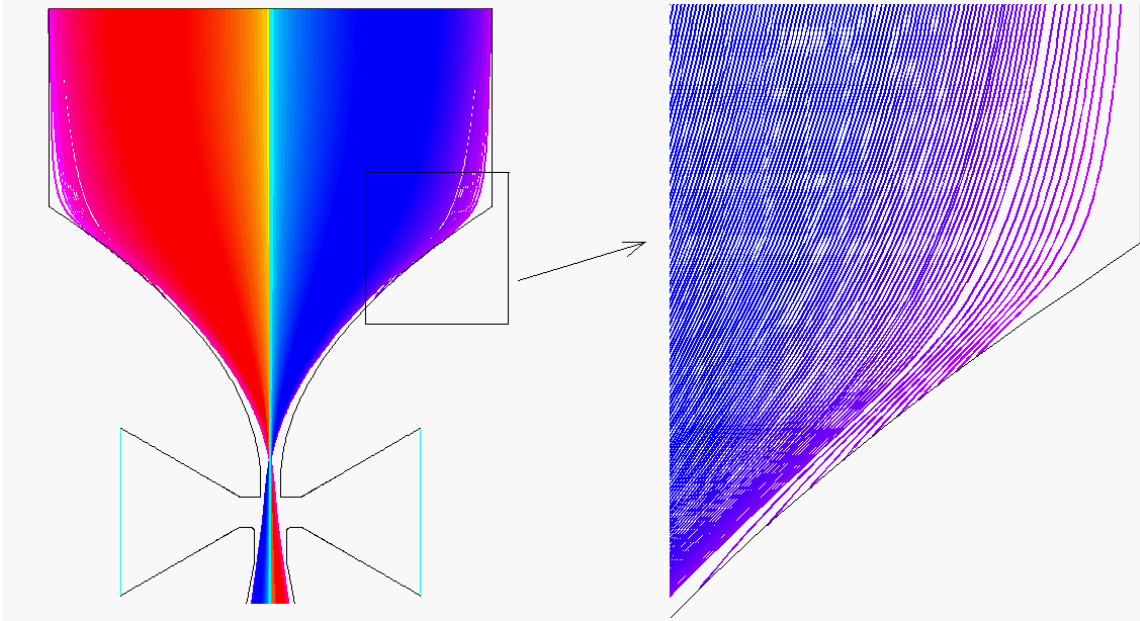
Figure 1 Pathline for 15 μm particles in a CSVI unit in 20K coarse mesh
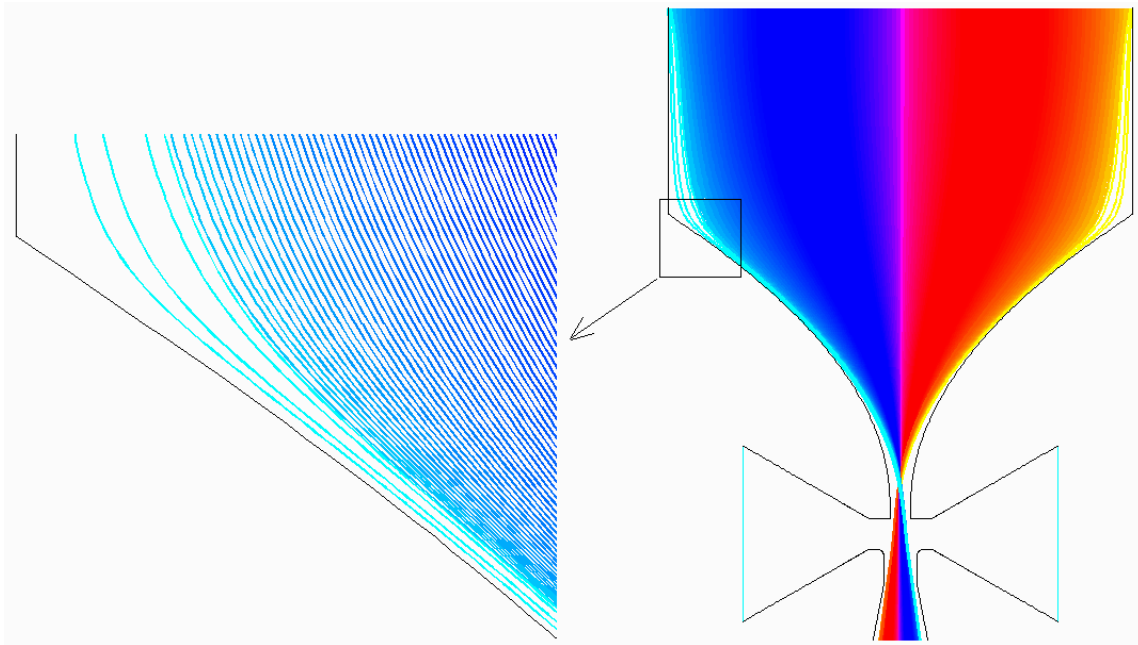
Figure 2 Pathline for 15 μm particles in a CSVI unit in 50K fine mesh

- ***On a 2D and 3D Simulation Discrepancy***

In some applications such as simulation of a round-jet impactor, a uniform velocity or a fully developed profile is used to set the boundary for its inlet. Actually, there is a connection tube upstream of the computational domain of the simulated impactor and the length of the tube can be short or long. When the flow in the tube and impactor is laminar, the flow conditions in the inlet of the computational domain depend on the upstream connection and it could be fully developed or developing because the entrance for laminar flow can be relatively long. It is to be expected that the calculated flow will be different for different flow conditions such as uniform constant or fully developed profile, and that the flow should be the same for the same inlet conditions in either 2D or 3D simulations. However, the results for the particle trajectory calculations

can be different for 2D and 3D simulations even if their calculated flow fields are the same.

In the round jet impactor, each particle has a stopping distance that particles can travel and a resistance distance that particles need to travel. If its stopping distance is longer than the resistance distance, the particle will generally reach the collection plate. For a particular particle having a certain Stokes number, there is a corresponding distance W_O that all the particles inside W_O on the cross-section of the circular inlet will be collected and outside of W_O will not be collected. When 2D and 3D simulations are performed for this round jet to predict collection efficiency, particles are released from a line or a surface area uniformly based on an assumption that concentration of particles is uniform spatially. In 2D simulation, particles are released from a line and the particles are distributed length-uniformly and each Δr on the line contains one particle. In 3D simulation, particles are generally released from a round surface uniformly and the particles are distributed area-uniformly and each ΔA_o contains one particle. Here Δr in 2D is corresponding to ΔA in 3D in location. Usually Δr is constant in the radial direction in 2D. But, obviously the corresponding outer ΔA values are larger than the inner ones based on the same length, Δr, and the outer ΔA contains more particles corresponding to the same Δr. In the round jet impactor, particles in the outer ΔA have longer resistance distance than those in the center area, i.e., the particles in the center region can move more easily to the collection plate. Comparing the number of particles in 2D and 3D simulations, the efficiency of the 3D simulation will be lower than the 2D simulation for a round jet impactor.

In this study, two types of round jet impactors will be considered – the classical impactor where the collection plate is assumed to be infinite in size, and a compound impactor where the jet discharges into a well and impaction can take place on both the bottom (collection plate) and the sides of the well. For the round-jet impactor with single impaction, 2D axisymmetric and 3D should have the same results for laminar flow calculations inside the impactor because they are using the same geometry and laminar flow conditions. Figures 4 and 5 show velocity distributions to compare the calculated flows for 2D and 3D at two lines (Line A and Line B) shown in Figure 3. One line is located in the exit of the jet and the other is located vertical to the bottom plate. The velocity values in Figures 4 and 5 are normalized by the average velocity V_o of the jet inside the inlet tube. The curve of the velocity in Figure 4 has a flat section which suggests that the flow for this case is still developing at the jet exit plane. It can be seen that the velocity curves in both Figures 4 and 5 for 2D and 3D are nearly identical, which means that the calculated flows are the same for 2D and 3D.
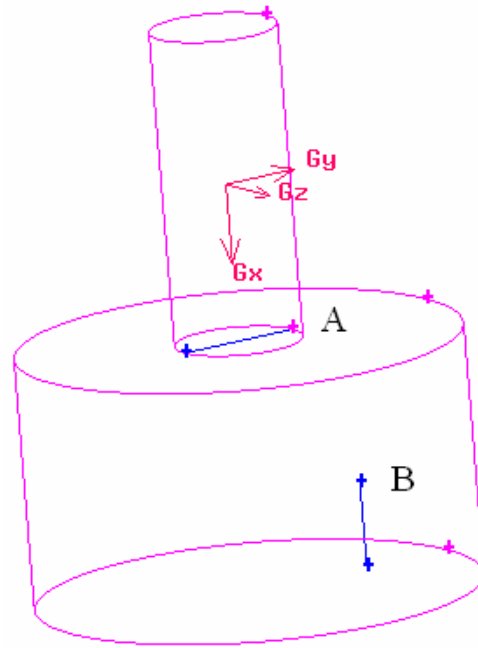
Figure 3 Locations of lines to compare in the impactor
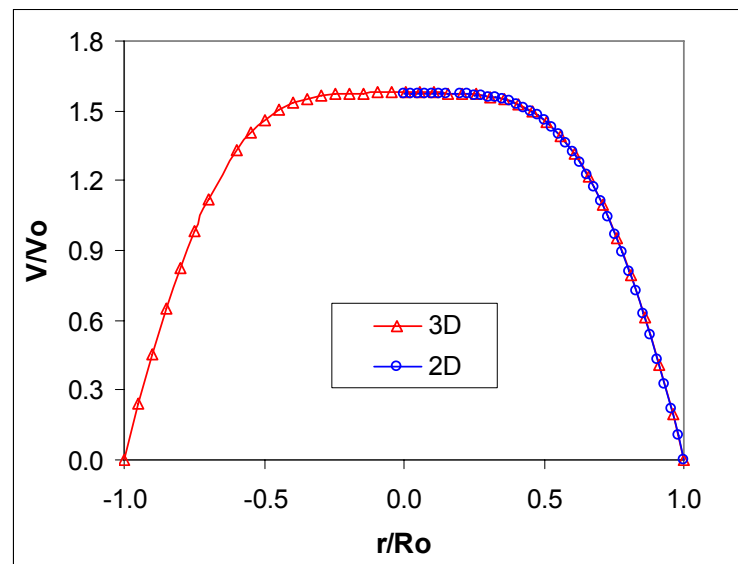
Figure 4 Velocity profiles for Line A in 2D and 3D simulations
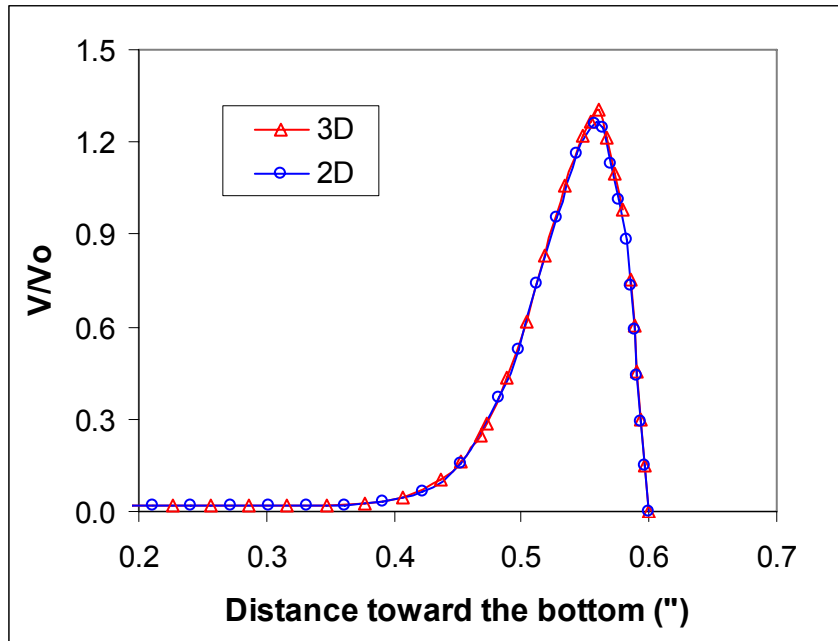
Figure 5 Velocity profiles for Line B in 2D and 3D simulations

Calculations for particle collection efficiency are different for 2D and 3D as shown in Figure 6, where it can be seen that 3D has a lower prediction of particle collection efficiency than 2D because of the particle releasing stratagem for DPM model which results it being more difficult to collect particles in 3D. The two curves are close but for those particles in the Stokes number range of 0.2-0.3, the 2D predictions for collection efficiency are about 10-15% higher than the 3D result for each particle size. If the ratio of collection efficiencies for 2D and 3D are plotted with particle Stokes numbers, it can be seen that the ratio is above 1.1 in the Stokes range of 0.2-0.3, Figure 7. Based on these considerations, 2D particle trajectory calculations could be converted based on a surface-area-weighted concept to improve the simulation. For a fixed particle size, its W_O can be found by particle trajectory checking. Then, the particle number is

calculated based on the surface area A_O with the radius W_O. The collected fraction is calculated with A_O divided by the entire area of the round inlet. After this conversion, 2D predictions will provide almost identical results to 3D.
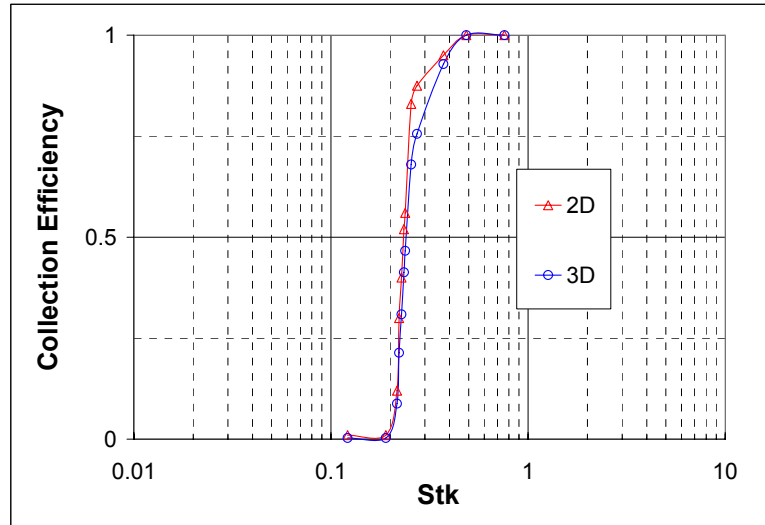
Figure 6 Collection efficiency for 2D and 3D based on the same jet impactor
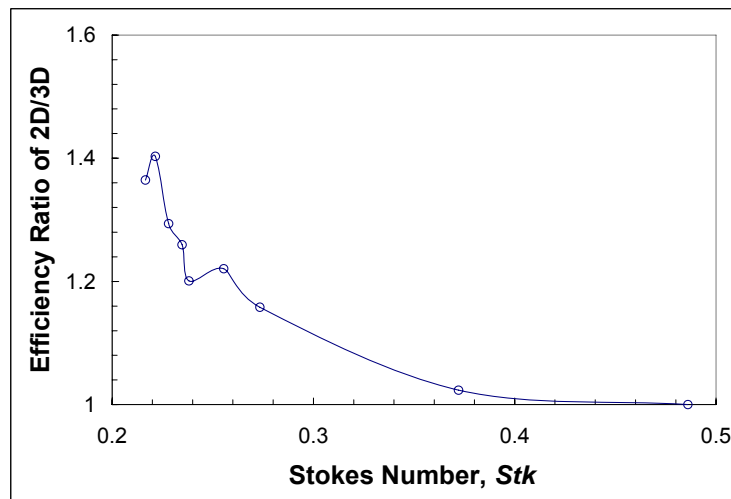
Figure 7 The ratio efficiency of 2D/3D as a function of Stokes number

- *On a 3D Simulation and Experiment Discrepancy*

Another factor to be considered is that the results of physical experiments are based on a time-period-collection to calculate collection, for example, an experiment may require sampling of aerosol for 10 minutes. Collection is typically calculated from the ratio of the mass of particles collected at the outlet and a reference sample. The simulation in FLUENT calculates the collection in similar processes but it is based on a one-time-release method in which a certain number of particles are released from a surface at a fixed amount of time and the number of collected particles is counted. However, the air velocity at the release surface may not be uniform due to the boundary layer effects and the center velocity is higher than the near-wall region especially for laminar flow where the boundary layer is relatively thicker than the turbulent one. It is reasonable to assume that the volume concentration is uniform throughout the space which implies that there will be more particles passing through the center area in the fixed experimental time-period, i.e., more easily collected particles. Consequently, the experimental results will provide higher collection efficiency for the round jet impactor than in the simulations.

Three-dimensional (3D) simulation can be improved by using a velocity-weighted method to make it compatible with the experimental method. One direct method is to control the number of particles at each point in the release surface based on a rounding of the local air velocity. Assume for example, that points A and B on the release surface have air velocities of 7.2m/s and 1.9 m/s, respectively. The number of particles released in the simulation from points A and B would be 7 and 2. The total

collection efficiency can be obtained by acquiring a summary of all the collected and released particles. The best way to realize this method is to modify the DPM in the software to consider the local velocity effect relating to the particle release.

Another method to improve the 3D prediction is to convert the simulated results through considering the velocity effects. The releasing surface can be divided into N sections, about 8-10 in the conversion, and each section i, numbered from the center to the edge, could use the same air velocity V_i. The total number N_{Total} of released particles is calculated from all the N sections and the number of collected particles $N_{collected}$ is calculated from the $0 \sim N_W$ sections where N_W corresponds to the value of W_O for each particle size. The collection efficiency can be calculated using N_{Total} and $N_{collected}$, Equation (13).

$$N_{Total} = \sum_{i=1}^{N} V_i \cdot C_0 \cdot 2\pi r_i \cdot \Delta r \tag{34}$$

$$N_{collected} = \sum_{i=1}^{N_W} V_i \cdot C_0 \cdot 2\pi r_i \cdot \Delta r \tag{35}$$

$$Efficiency = \frac{N_{collected}}{N_{Total}} \tag{36}$$

2.4 VOF Model for Two-Phase Flow

The VOF model is a multiphase model embedded in FLUENT, which is used for flow with a free-surface or a clear interface, i.e., where the fluid phases do not intermingle. VOF determines the volume fraction α_q for each phase (*q*) in every computational cell as a specified variable to indicate how much the cell is filled with the phase *q*. If α_q = 1, the cell is filled with phase q and if it is zero, there is no phase q in that cell. In the cyclone study presented herein, a value of α_q = 0.5 indicates the location of the interface between air and water, as the cells are filled with half air and half water. The continuity equations for the volume fraction of the phases are:

$$\frac{\partial \alpha_q}{\partial t} + \vec{\mathbf{U}} \cdot \nabla \alpha_q = \frac{S_{\alpha_q}}{\rho_q} \qquad (37)$$

$$\sum \alpha_q = 1 \qquad (38)$$

Where, $S_{\alpha q}$ is the source term of phase *q* and ρ_q is the density of phase *q*. A single momentum equation is solved for all cells and its velocity results are for all phases, namely,

$$\frac{\partial}{\partial t}(\rho \vec{U}) + \nabla \cdot (\rho \vec{U} \vec{U}) = -\nabla p + \nabla \cdot [\mu(\nabla \vec{U} + \nabla \vec{U}^T)] + \rho \vec{g} \qquad (39)$$

where p is pressure and $\bar{g}$ is gravity.

2.4.1 Special Meshing Method for VOF

For the VOF model, the water side should contain several cells in the direction normal to the wall. This implies that the cell size must be very small (on the order of micrometers in thickness) because the liquid phase thickness is generally very thin (a few tens of micrometers). This requirement would usually make a study of the film

formation with a 3D VOF model very difficult in some applications with a complex and large geometry such as a cyclone.

The approach adopted to analyze this problem was to setup a thin shell-volume in the near-wall region, which is sufficiently thick to include the water film on the wall. Boundary conditions for the air side surface of the shell were obtained from the results of a single-phase flow simulation on the whole geometry that generated a velocity profile to be used in the shell method. Because the water film is very thin, it is reasonable to assume that the presence of the water film will not significantly affect the air flow, so the results from the single-phase air flow simulation can be used as the boundary condition for the two-phase shell simulation.

2.5 Heat Transfer

Two steps with the appropriate models are conducted when FLUENT is used to simulate the heat transfer features for some applications. First, the air flow field and energy equation are resolved to find the convective turbulent heat transfer coefficient on the internal surface of the device. In this step, the turbulent heat transfer coefficient for the internal surface was calculated and stored in a data profile which will be used in the second step. Second, only the solid wall of the device is simulated, and that is accomplished by considering conduction and convection based on wall thermal properties and the turbulent heat transfer coefficients transferred from the first step. The energy equation used in FLUENT is:

$$\frac{\partial}{\partial t}(\rho E) + \nabla \cdot (\bar{u}(\rho E + p)) = \nabla \cdot (k_{eff} \nabla T) \tag{40}$$

$$k_{eff} = k + k_t \tag{41}$$

Here, k is the thermal conductivity and k_t is the turbulent thermal conductivity

calculated in the turbulent models.

CHAPTER III

IMPACTOR

3.1 Introduction

The geometry of a classical impactor is simple and the device is easy to fabricate and operate. They have been studied extensively for different configurations and operational conditions. Marple and Liu (1974) investigated the characteristics of laminar jet rectangular and round impactors using numerical simulations. Their studies analyzed the effects of some factors on impactor efficiency including Reynolds number, the ratio of jet characteristic dimension to the distance between jet exit plane and plate, and the Stokes number. Hari et al. (2005) conducted numerical studies on the performance sensitivities of the affecting factors for a rectangular slot impactor including gravity and ultra-Stokesian drag. Their predictions agreed well with experimental results. Burwash *et al.* (2006) studied turbulent dispersion effects on 5 μm particles for an axisymmetric impinging jet with Reynolds number 10^4 on a flat surface and suggested that the turbulent dispersion for particle deposition is many times that of particle inertial impaction. They used Shear Stress Transport (SST) turbulent model in CFX (CFX5.7.1, Ansys, Inc.) to simulate the jet and got reasonable results qualitatively and quantitatively compared with experimental results. For the 5 μm particles in their study, the Stokes number is about 0.11 and the collection efficiency is about 16% which suggested that $Stk_{0.5}$ is much larger than 0.11 for the turbulent flow in their study. John (1999) gave a simple derivation for impactors and showed $Stk_{0.5}$ values of about 0.49 and 0.25 for

rectangular and circular jets, respectively. Huang and Tsai (2002) numerically investigated the influence of the ratio of the jet diameter W to the impaction plate diameter D_C, W/D_C in a round-nozzle impactor. They found that the collection efficiency increases when the ratio decreases (same jet, larger plate) in a Reynolds number range of 100~500 at a fixed Stokes number and attributed the effect to a slower jet and gravitational effect.

Some applications for real impactors with confined jets have been reported. McFarland and Ortiz (1982) developed a 10 μm cutpoint ambient aerosol sampling inlet that used 9 turbulent jets with a diameter of 0.98 cm each in a plenum with a diameter of about 30 cm for a design sampling air flow rate of 113 L/min. Peters et al. (2001) reported on an EPA WINS impactor which used a single jet-in-well device operated at a flow rate of 16.7 L/min to remove particles larger than 2.5 μm. Different nozzles and well geometries together with oil and filter collection surfaces were compared. The effect of the size of the collection well on the performance of the WINS was discussed, but no details were provided. The Reynolds number of the WINS was about 6,000 and $Stk_{0.5}$ was about 0.22.

In this study, numerical techniques were used to characterize the performance of two kinds of impactors. One is an Inline Cone Impactor (ICI) where the air is accelerated in the space between a cone and a tube wall. Another is a jet-in-well impactor (JIW) that

uses a jet nozzle to impinge flow into a well. The impactors were used as components of bioaerosol sampling inlets and served as the role of large-particle fractionators. The $k - \omega$ turbulent model was used to calculate the flow field and the Random Walk Model (RWM) was used in the Discrete Phased Model (DPM) to calculate the particle trajectory.

3.2 System Description

The Inverse Cone Impactor (ICI) uses a cone inside a tube to form a round slot to accelerate the air flow inside the tube and it has an axisymmetric geometry, Figure 8. The air impacts onto the bottom plate during which particles with sufficient inertia can reach the plate and be collected. The air is then exhausted through a smaller tube downstream of the plate. Important parameters for the ICI include the average air velocity in the gap between the cone base and the tube wall, *U*, flow Reynolds number *Re,* and Stokes number *Stk* based on gap width *W* and velocity *U*.
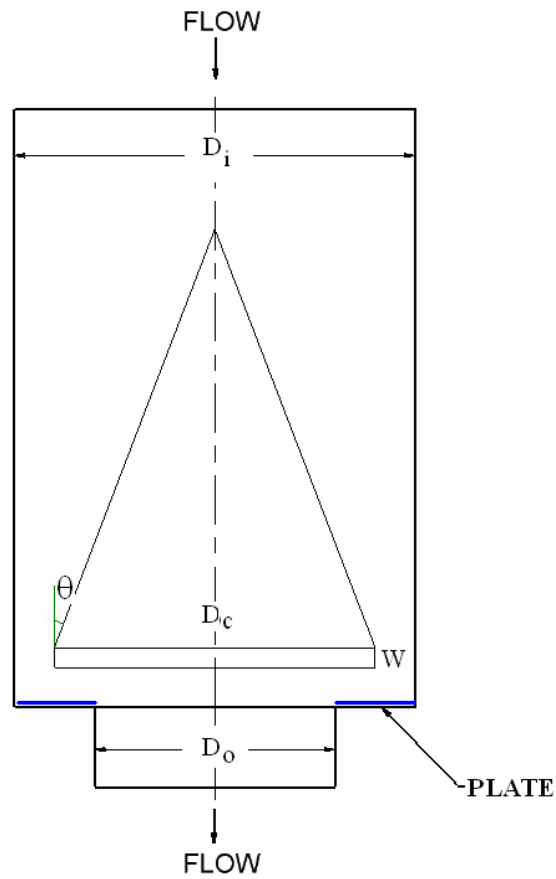
Figure 8 Schematic layout of the Inverse Cone Impactor

Symbolic expressions for these parameters are:

$$U = \frac{\dot{Q}}{\frac{\pi}{4}*(D_i^2 - D_c^2)*W} \tag{42}$$

$$Re = \frac{\rho U W}{\mu} \tag{43}$$

$$Stk = \frac{C_c \rho_P U D_P^2}{18\mu W} \tag{44}$$

Here, $\dot{Q}$ is the flow rate, D_i is the diameter of the inlet tube and D_c is the diameter of the

cone.

With reference to Figure 9, the jet-in-well impactor considered herein is comprised of an acceleration nozzle that discharges air into a cup or well, where the flow impacts the bottom plate, and then is directed horizontally toward the side wall of the well. The flow then makes another turn and is directed upwards where it is vented from the well. Primary and secondary inertial impactions of aerosol particles take place on the bottom plate and the side wall, so the process is referred to herein as compound impaction. Important parameters for the jet-in-well impactors include the volumetric flow rate ($\dot{Q}$), jet velocity (U), the flow Reynolds number (Re), the Stokes number (Stk) at the outlet of the jet, and the ratio of well-to-jet diameters (χ).
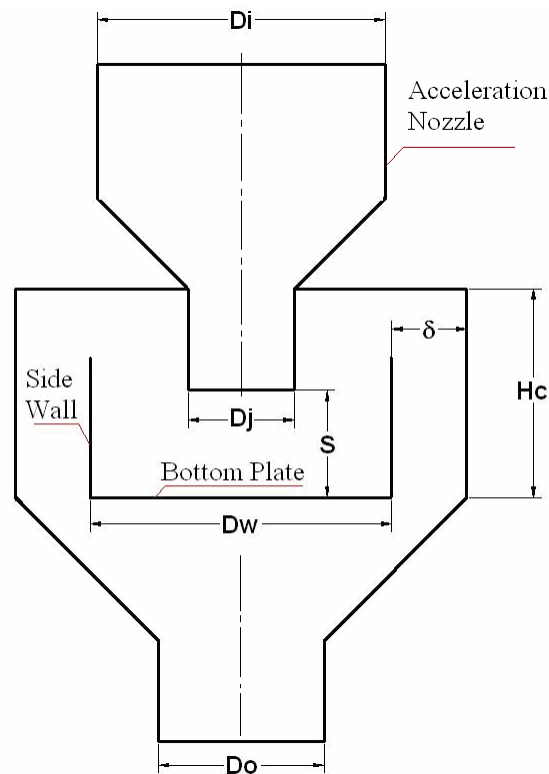
Figure 9 Schematic layout of the Jet-in-Well Impactor

$$U = \frac{\dot{Q}}{\frac{\pi}{4}D_j^2} \tag{45}$$

$$Re = \frac{\rho U D_j}{\mu} \tag{46}$$

$$Stk = \frac{C_c \rho_P U \infty D_P^2}{9\mu D_j} \tag{47}$$

$$\chi = \frac{D_W}{D_j} \tag{48}$$

Here, D_j is the diameter of the jet and D_W is the diameter of the well. Jet diameter is used to calculate the particle Stokes number.

For both impactors, another important dimension is the jet-to-plate distance S, which has a measurable influence on the collection efficiency of the impactors. In addition to these parameters, reference will also be made to the cutpoint, $D_{0.5}$, which is the aerodynamic diameter for which the collection efficiency is 50%. Correspondingly, use will also be made of the cutpoint Stokes number, $Stk_{0.5}$.

3.3 Results and Discussion

3.3.1 Inverse Cone Impactor

The flow rate of the Inverse Cone Impactor in this study is 1250 L/min. Earlier inlets with such high flow rates generally are of relatively large sizes and housing diameters of about 600 mm (approximately 2-ft) for the case of multiple jets. In this study, a compact Inverse Cone Impactor is designed with a tube diameter of only 127 mm (5"). Two different cones are used in the simulation and experiment to study the performance of this type of impactor. Table 1 gives the dimensions and parameters of the two Inverse Cone Impactors, which have different sizes of cones inside the same 127

mm tubes. The two different cones are used to obtain different jet velocities, slot widths, and correspondingly, varying Stokes numbers for particles. It can be seen from this table that the flow has high Reynolds numbers at the inlet, gap width, and outlet, namely, 13,900, 3,700, and 27,800, which means that the flow inside the Inverse Cone Impactor is probably turbulent. The Reynolds number at the gap area is about 3,700 which is a low Reynolds turbulent flow. This requires the use of the $k - \omega$ turbulent model because this model is suitable for low Reynolds turbulent flows. Two-dimensional (2D) simulation is used because the geometry is axisymmetric and the gap width is small in comparison with the radius of the tube at that location.

Table 1. Dimension and parameter for Inverse Cone Impactors

Item	Case 1	Case 2
Flow rate (L/min)	1250	1250
Inlet diameter (mm)	127	127
Cone diameter (mm)	105.4	110.4
Gap width W (mm)	10.80	8.32
Jet-to-plate distance S (mm)	21.59	16.64
Ratio of S/W	2	2
Outlet diameter (mm)	63.5	63.5
Averaged velocity at inlet (m/s)	1.64	1.64
Reynolds number at inlet	13,900	13,900
Average velocity at gap width (m/s)	5.29	6.72
Reynolds number at gap width	3,800	3,720
Averaged velocity at outlet (m/s)	6.72	6.72
Reynolds number at outlet	27,800	27,800

Figure 10 shows the velocity contours inside the Inverse Cone Impactor for the cone diameter of 105.4 mm (Case 1). There is reverse flow at the outlet exhaust tube but that does not affect the stability of the entire flow. Typical velocities at different locations are shown in Figure 11 using the format of velocity vectors. The flow approaching the impaction zone is relatively uniform as is the case with the jet flow of a classical impactor.
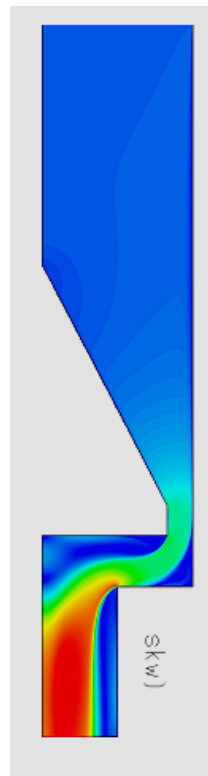
Figure 10 Velocity contour for 105.41 mm cone, 2D simulation. Only one half of the axisymmetric flow field is shown
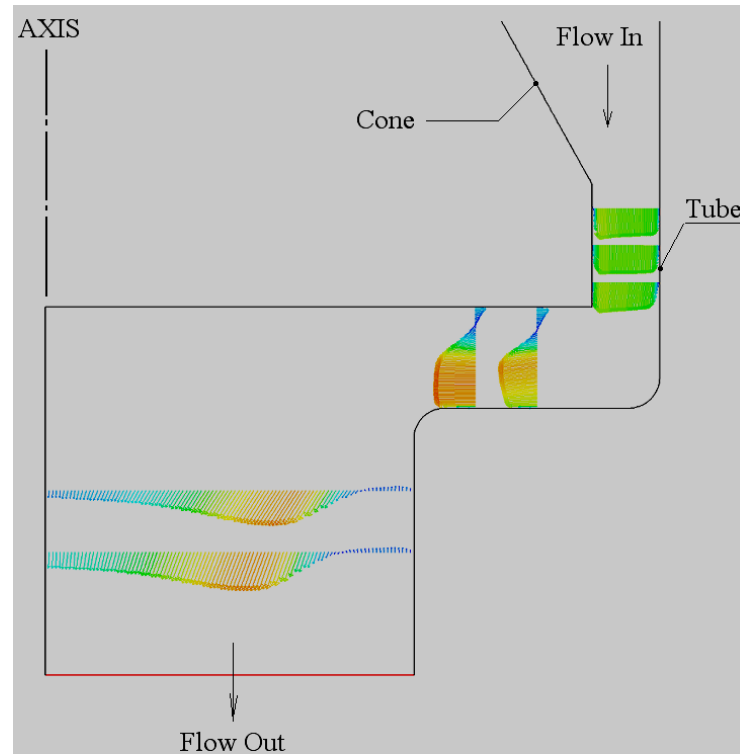
Figure 11 Velocity vectors at different locations inside Inverse Cone Impactor

Figure 12 shows the numerical predictions and experimental results for the particle collection efficiencies of the two Inline Cone Impactors (ICI) listed in Table 1 (different gap widths). The numerical predictions agree well with the experimental results in the Stokes range of 0.04~1.3. The collection curves for the two different gap width impactors almost overlap which means that the particle behavior in this type of ICI is primarily a function of the particle Stokes number. The cutpoint Stokes number, $Stk_{0.5}$, is abut 0.28 for the impactors with the gap width Reynolds number of about 3,800.
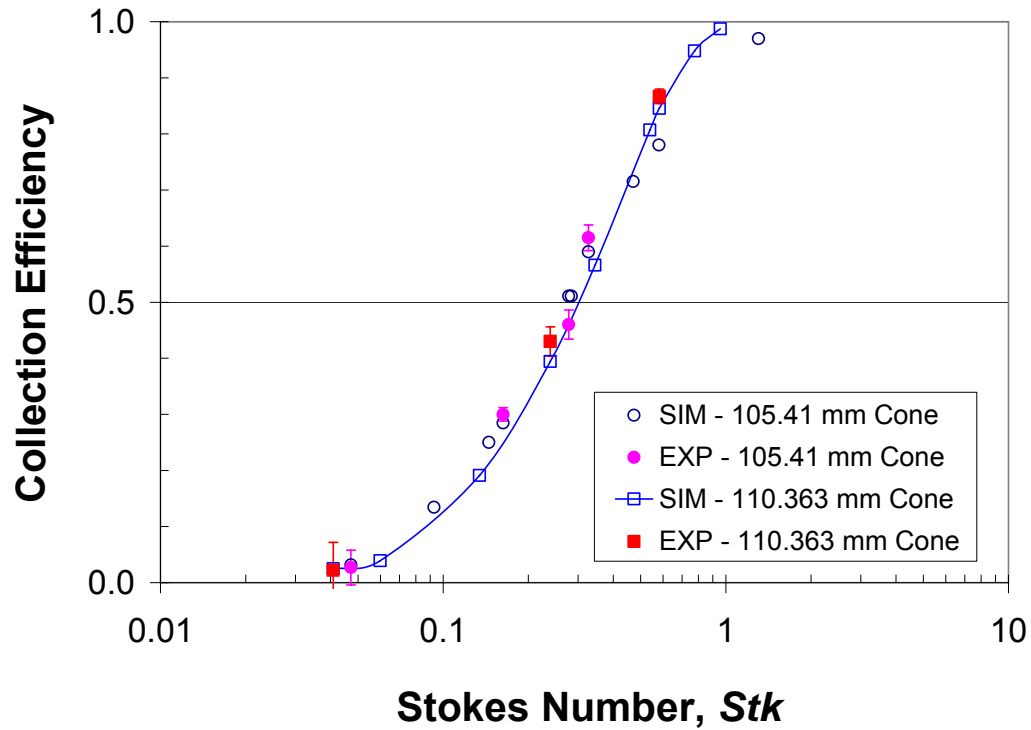
Figure 12 Collection efficiency as a function of Stokes number for the Inline-Impactor. Here, EXP refers to experimental results and SIM represents simulation predictions

The value of $Stk_{0.5}$ is smaller than the typical rectangular jet impactors, which have $Stk_{0.5}$ of about 0.59, but larger than the typical circular jet impactor, which has a $Stk_{0.5}$ of about 0.24 (Hinds, 1999). Compared to a pure rectangular jet impactor, where particles are uniformly distributed across the jet width, in the ICI the linear-fraction, of the particles at the inner region near the cone, is smaller because the area is proportional to the radius. In the ICI, the particles passing near the cone have a longer distance to travel to reach the bottom plate so they are more difficult to collect. This results in a higher fraction of particles that are less difficult to collect and thereby a higher collection in ICI than the typical rectangular jet impactor.

3.3.2 The Compound Impactor

Three physical prototypes of jet-in-well impactors were tested in this study, which employed different jet nozzles and wells. The ratios of well diameter-to-jet diameter are 3, 4, and 7.2. The Reynolds numbers based on jet exit plane conditions range from 2230 to 4230, which is in the realm of transitional to low Reynolds number turbulent flow.

Table 2. Parameters used in physical experiments

Parameter	Case 1	Case 2	Case 3
Flow rate, $\dot{Q}$, (L/min)	90	20	20
Jet Diameter, Dj (mm)	30.48	12.7	12.7
Well diameter D_W (mm)	91.4	91.4	50.8
Well-to-Jet ratio, χ	3	7.2	4
Flow Reynolds number at jet exit	4,230	2,230	2,230

3.3.2.1. The Compound Impaction Phenomenon

Figure 13 shows four photos taken after exposing the impactors for about 1 hour to particles with different Stokes numbers. Here, filter paper was placed on the bottom of the well (primary impaction) and around the wall of the well (secondary impaction). Blue food coloring was added to the liquid used for particle generation to provide additional contrast of the deposited particles on the filter papers to the contrast that would be provided by the usual analytical tracer, sodium fluorescent, of the aerosol generation liquid. The jet-in-well impactor had the same dimensions as the cases listed in Table 2. Different particle sizes were selected and generated to obtain different

particle Stokes number. The dark-green color results from the mixture of the yellow fluorescent tracer and the blue dye in the deposited liquid particles. In each photo, the upper part (circular) shows the deposition on the bottom plate and the lower part shows a small section of the side wall deposition. It can be seen that the particle deposition patterns are totally different in the impactors with different well-to-jet ratios and particle Stokes numbers.

In Figure 13(a), the particles deposit both on the bottom plate and on the side-wall. This photo represents the Case 3 impactor in which the well-to-jet ratio is 4.0 and the particle Stokes number is 0.12. On the bottom plate, the deposition from the primary impaction appears as a uniformly distributed spot, which is caused by the first turn of the air flow. However, on the side-wall, there is a clearly defined strip on the cylinder surface, which indicates significant secondary impaction. The narrow strip of deposition [Figure 13(a)] suggests that the deposition on the side-wall is primarily a result of the secondary impaction because if it was caused by turbulent dispersion, it would be more diffused. Figure 13(b) shows the results for the same Case 3 impactor as in Figure 13(a), but with particles having a larger Stokes number (0.27). On the bottom plate, deposition forms a uniformly distributed spot which is caused by the primary impaction. However, the deposition on the side-wall is very faint, which suggests that most particles are collected on the bottom plate with few particles reaching the side-wall. Figure 13(c) shows the deposition for the Case 1 impactor with a well-to-jet ratio of 3.0 using particles with a Stokes number of 0.06. For these small Stokes number particles, the deposition on the bottom plate is faint. However, there is a clear strip on the side wall,

which indicates that the secondary side wall impaction is much more significant than the primary bottom plate impaction. Figure 13(d) gives the deposition results for the Case 2 impactor where the well-to-jet ratio is as large as 7.2, but with the same particles as in Figure 13(a) that have a Stokes number of 0.12. The deposition on the bottom plate is a clear spot which is similar to Figure 13(a). The spot in 13(d) looks smaller than 13(a) because 13(d) has a well size of 90.4 mm (3.6-inches), whereas in 13(a) the well is 50.8 mm (2-inches). The deposition is faint on the side wall of Figure 13(d), where the impactor has a large well-to-jet ratio, which indicates that the secondary impaction is slight. Comparing the patterns in Figure 13(d) where the ratio is 7.2 with Figure 13(a) where the ratio is 4.0, the side wall deposition in 13(a) is much heavier even though the two cases have the same Stokes number.

With reference to Figure 14 , when the velocity contour is checked in simulation using the same geometry and flow conditions as Figure 13(c), i.e., $\chi = 3$, it shows the location of the secondary turn of the air flow hitting the side wall starting at a distance of about 4 mm above the bottom plate. This supports the occurrence of the deposition strip shown in Figure 13(c).
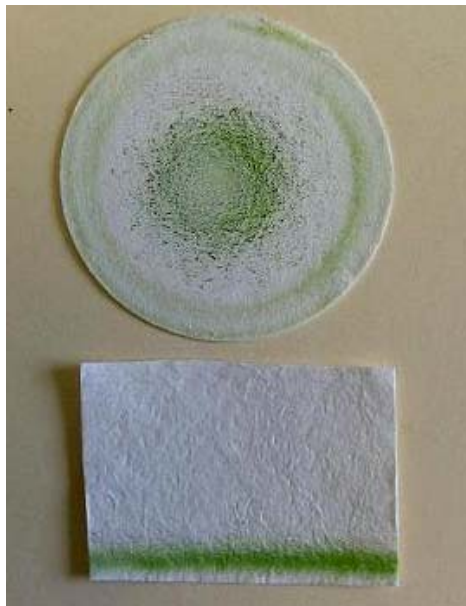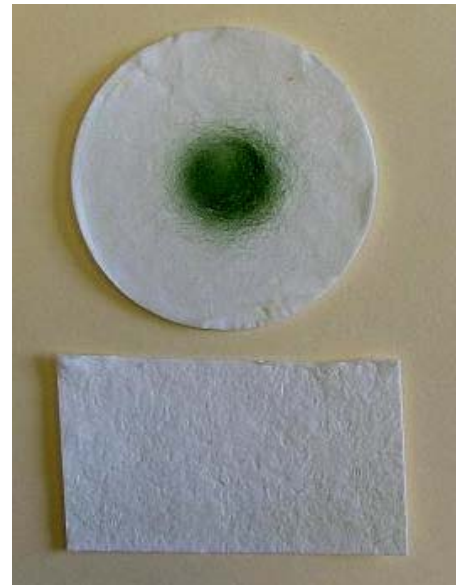
(a) $\chi=4$, Stk=0.12   (b) $\chi=4$, Stk=0.27
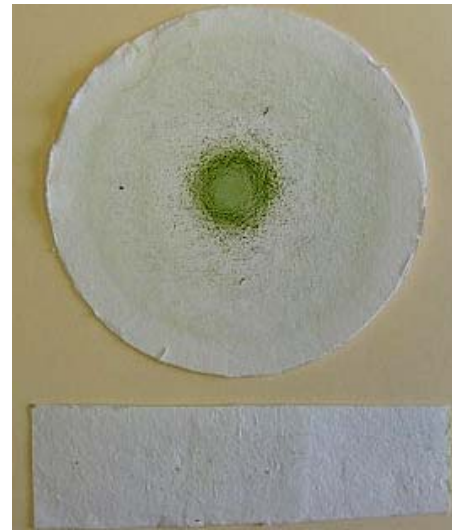
(c) $\chi=3$, Stk=0.06   (d) $\chi=7.2$, Stk=0.12

Figure 13 Photos of particle deposition patterns on filter papers that show primary (circular) and secondary impaction (rectangular). Different well-to-jet ratio and particle Stokes numbers were used
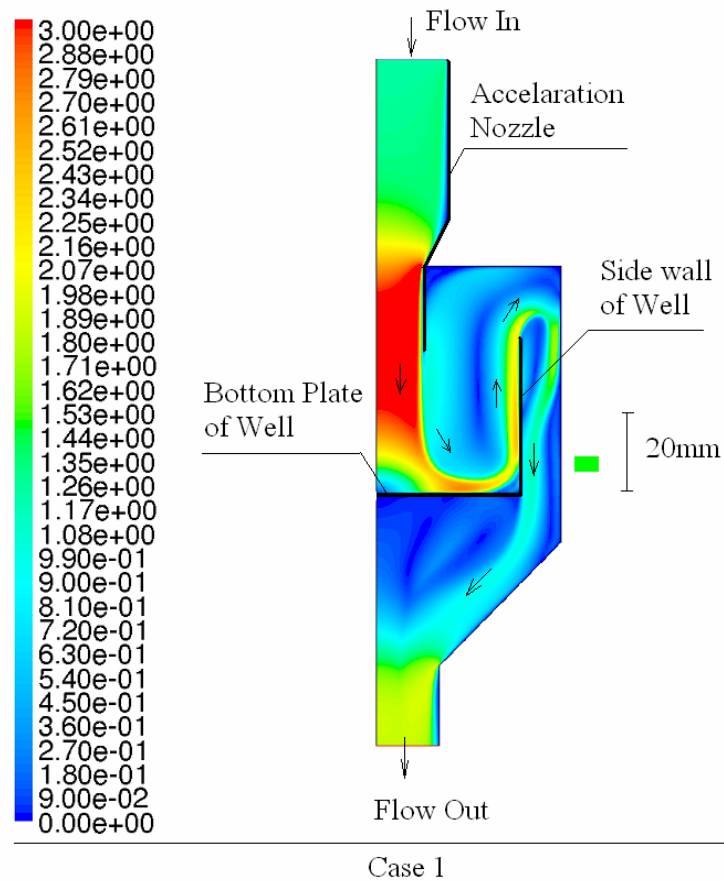
Figure 14 Velocity contour for jet-in-well impactor, Case 1 with well-to-jet diameter ratio 3

Figures 13(c) and 14 may be used to describe how the compound impaction takes place. During the first turn of the air impacting on the bottom plate, particles could reach the plate if the inertia is sufficient or they could follow the air to flow toward the side wall. However, during this primary impaction, a particle that does not reach the bottom plate may move a short distance toward the bottom plate, i.e., it will shift its trajectory to a path closer to the bottom plate. As the air flow approaches the side wall in a small-sized well, its velocity does not decrease significantly so the particle stopping distance is maintained. However, particles having benefited from the displacement in the primary

process may be able to reach the side wall during the second turn of the air. In a sense, the effect of the primary process upon the secondary process is equivalent to increasing the Stokes number of the secondary process, as the Stokes number can be considered to be the ratio of the particles stopping distance to a characteristic dimension, and the characteristic dimension for impaction is reduced by the primary effect.

When the well size is increased and the jet diameter is maintained constant, the velocity of the flow towards the well wall will decrease, so the secondary side wall impaction is attenuated as the jet approaches the side wall. It can be expected that the total collection of the jet-in-well impactor could increase when the well size decreases due to the stronger secondary impaction when other conditions are the same.

3.3.2.2 Compound Impaction Collection Efficiency

Figure 15 shows the numerical prediction for the collection efficiency of the jet-in-well impactors with different well-to-jet ratios from 3 to 15. When the well-to-jet ratio is increased from 3 to 15, the total collection decreases and the collection curve shifts towards the right. When the ratio is in the range of 3 to 8, the total efficiency increases rapidly with decreasing well-to-jet ratio and the $Stk_{0.5}$ decreases significantly, which implies that the secondary side wall impaction may even be dominant, which is similar to the situation shown in Figure 13c. As χ decreases from 8 to 3, $Stk_{0.5}$ decreases from 0.23 to about 0.07 and the collection curves separate from each other. However, when the ratio is $\chi \geq 8$, the ratio has little effect on the total collection, i.e., the secondary side wall impaction is too weak to affect the total impaction, which occurs because the radial air velocity is too small to cause the secondary impaction.

Figure 15 also shows the experimental results for the three cases of jet-in-well impactors with well-to-jet ratios of 3, 4, and 7.2. Numerical predictions agree well with the experimental tests for the particles having larger Stokes numbers and suggests that $k - \omega$ could be a suitable model for particle trajectory calculation in such jet-in-well impactors. However, the numerical results over-predict the efficiency of collection for the particles with Stokes numbers smaller than 0.04. In the jet-in-well impactor, particle deposition could be caused by the combination of inertial impaction and the turbulent dispersion process. Matida *et al.* (2004) suggests that the turbulent dispersion model can cause over-prediction of the particle deposition. For small Stokes number particles, turbulent dispersion deposition may be several times higher than the inertial impaction (Burwash *et al.* 2006). However, for particles having larger Stokes numbers, inertia will be dominant and thus the overall deposition would be relatively unaffected by any inaccuracies in the turbulent dispersion model, i.e., the deposition caused by the turbulent dispersion is small so even if it is over predicted, it does not affect the overall accuracy of the total prediction and thus the numerical results for the particles with large Stokes numbers could agree well with the experimental tests.
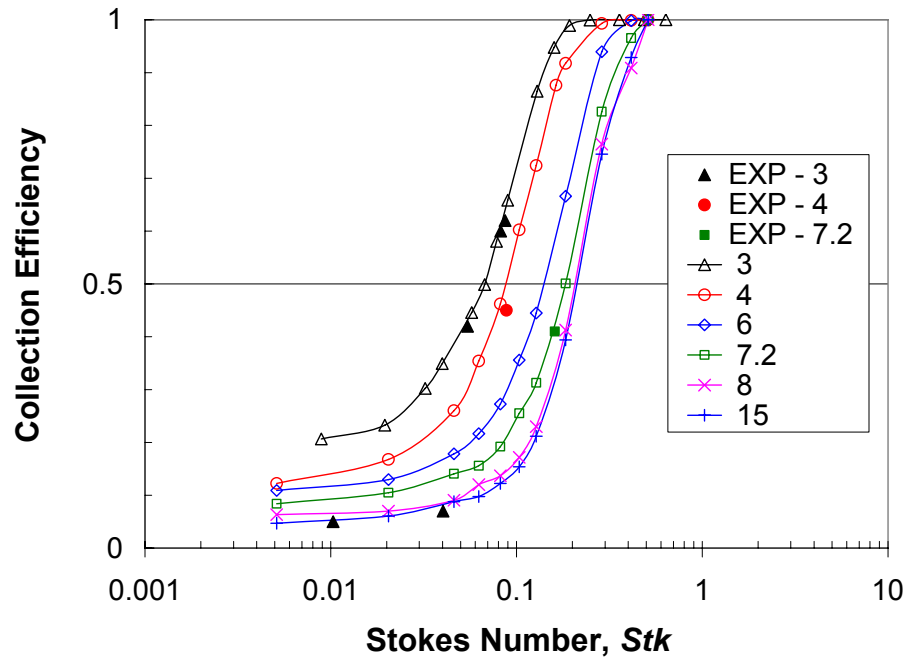
Figure 15 Simulated and experimentally determined total collection as a function of Stokes number for various well-to-jet ratios. Here EXP refers to experimental results

3.3.2.3 Effect of Well-to-Jet Diameter Ratio on Cutpoint

The effect of the ratio of well-to-jet in different ranges on the $Stk_{0.5}$ can be expressed through a correlation as shown in Equation (49) and Figure 16. When the ratio is less than 8, $Stk_{0.5}$ will increase with the increasing ratio. When the ratio is larger than 8, $Stk_{0.5}$ remains stable at about 0.23.

$$Stk_{0.5} = 0.0314e^{0.2486\chi} \qquad 3 \le \chi \le 8 \qquad (49)$$
$$Stk_{0.5} = 0.23 \qquad\qquad \chi \ge 8$$

A special feature of the compound impactor is that when the ratio of well-to-jet is less than about 6, the reflected flow from the side wall may sometimes influence the initial jet from the acceleration nozzle and cause the total flow to fluctuate, as shown in Figure 17 for the Case 3 impactor. The onset of the interaction depends on the flow

conditions and dimensions of the impactor. This suggests that the well-to-jet ratio should be in a range of 6-8 to avoid both a too large well and to achieve a suitable flow field. However, in some special applications, a smaller ratio could be considered as it can provide the same cutpoint with a lower velocity jet, thereby consuming lower power. The US EPA WINS impactor (Peters et al. 2001) has a well-to-jet ratio of 9.45 which falls in the large ratio category, so the secondary impaction in WINS can be ignored. The $Stk_{0.5}$ of WINS is about 0.238 which is close to the result of 0.23 determined in this study.
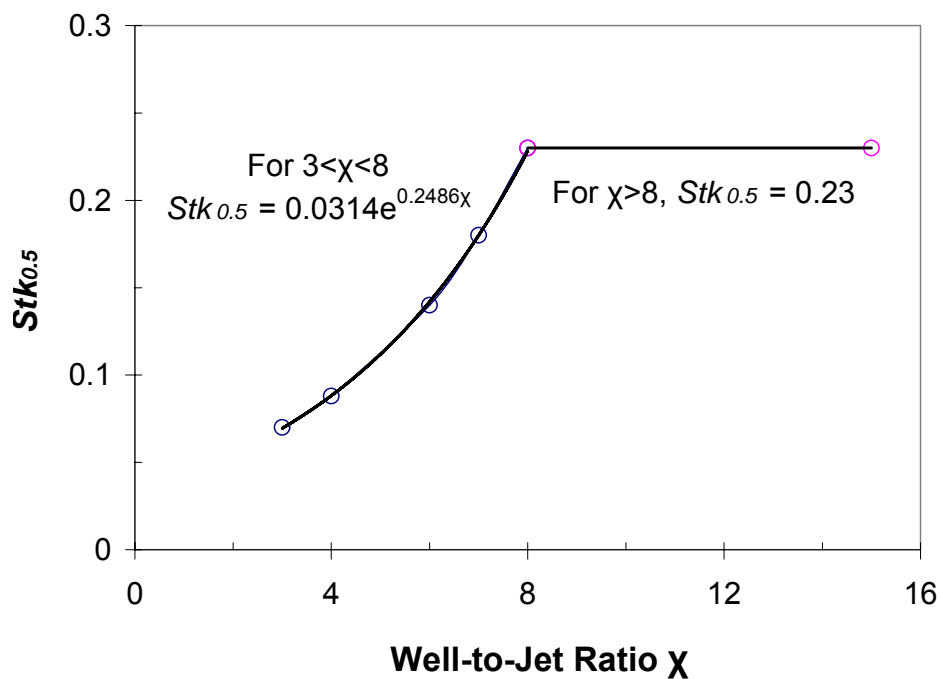
Figure 16 The cutpoint Stokes number, $Stk_{0.5}$, as a function of well-to-jet ratio χ
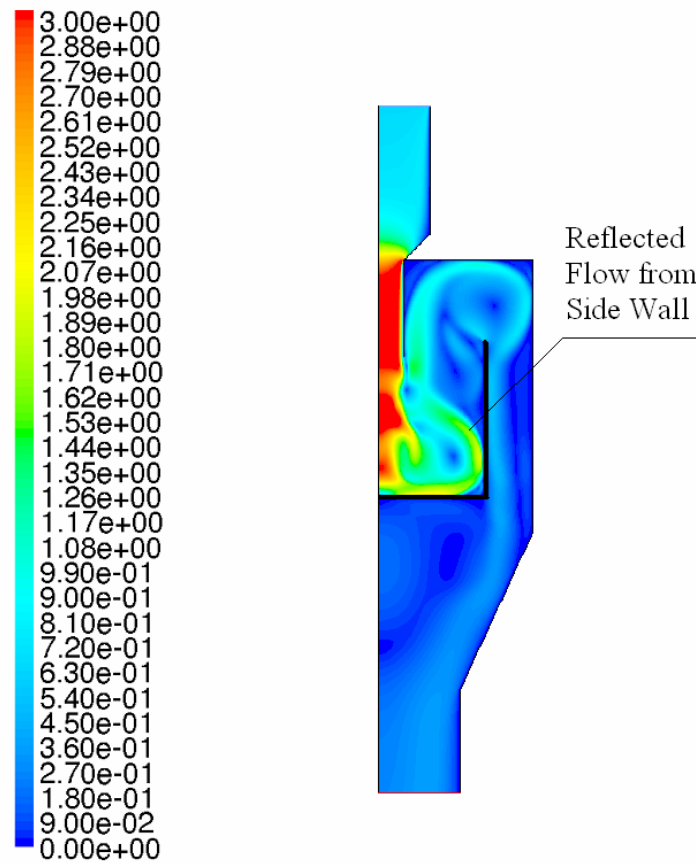
Figure 17 Velocity contour for jet-in-well impactor, Case 3 with well-to-jet diameter ratio 4

3.3.2.4. Comparison of Primary and Secondary Impaction

Figures 18 and 19 show the numerically predicted collections for the bottom plate and side wall with well-to-jet ratio of 4 and 7.2. The collection curves for the bottom plate are almost the same for the two ratios since their initial jets are operated at the same conditions and the primary impaction is, therefore, similar. However, the collection on the side walls is quite different due to different well-to-jet ratio. When the ratio is 4 and the secondary impaction is strong, the side wall collection is about twice that on the bottom plate for the smaller particles and drops quickly for the larger

particles, Figure 18. The maximum collection on the side wall could be as high as 40% for the particles having a Stokes number of 0.2. This significant secondary side wall impaction may be caused by two phenomena. First, the particles which are not collected on the bottom plate can shift their trajectories as discussed earlier. Second, gravity could enhance this movement of the particles towards the bottom plate because the first impaction process and gravity generally have the same direction. These two effects would concentrate the particles in the region closer to the bottom plate and make the particles easier to impact onto the side wall. In Figure 18, the reduced side wall collection for larger particles (Stokes numbers greater than about 0.1) is caused by the fact that the primary impaction process has already removed the high inertial particles.

When the well-to-jet ratio is high the secondary side wall impaction will be weak. Figure 19 shows that for a well-to-jet ratio of 7.2, the side wall collection peaks at about 12%; and the fractional efficiency curve for the primary impaction process is quite similar to that for the total efficiency.
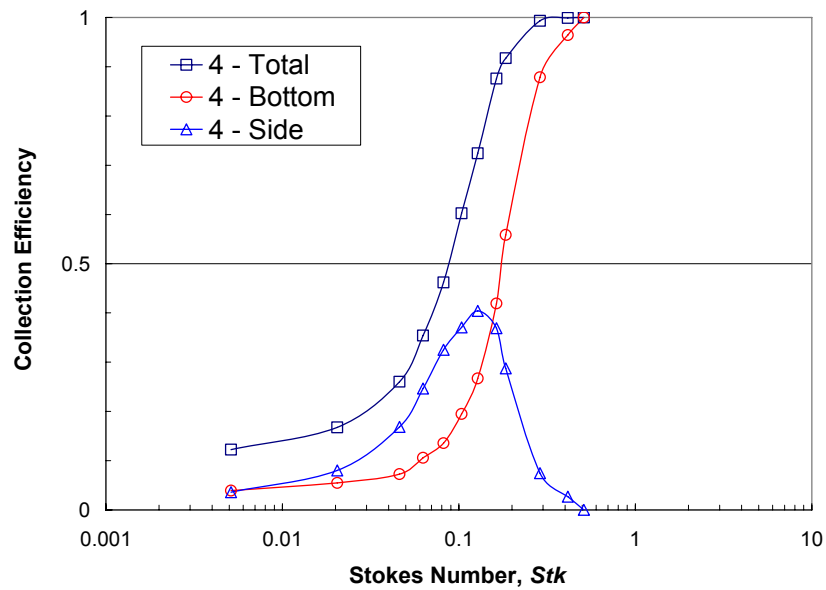
Figure 18 Total, bottom plate and side wall collection of the jet-in-well impactor with a well-to-jet ratio of 4
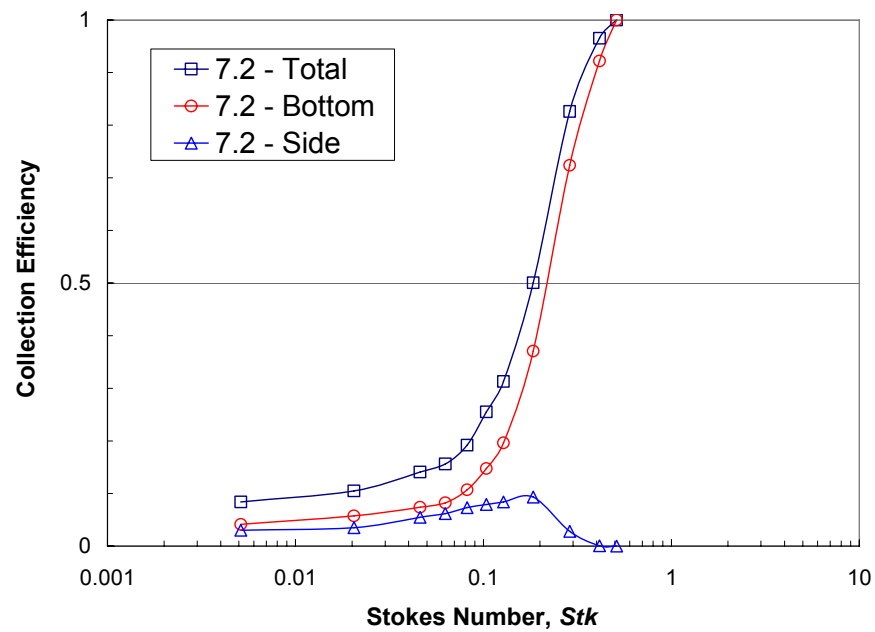
Figure 19 Total, bottom plate and side wall collection of the jet-in-well impactor with well-to-jet ratio of 7

The influence of the well-to-jet size ratio on the secondary side wall collection is shown in Figure 20 for ratios from 3 to 15. Generally, as the ratio increases, the side wall collection decreases. The peak value of the side wall collection decreases from 40% to be only about 5% when the ratio increases from 3 to 8. When the ratio is larger than 8, the side wall collection remains small for all particle sizes, i.e., the secondary side wall impaction can be ignored. This is also demonstrated in Figure 15, where the total collection does not change when the ratio is increased beyond about 8. Figure 20 also shows an unexpected result for very small size ratios, where the peak secondary impaction is greater for a ratio of 4 than the ratio of 3. This could be due to fluctuating flow associated with the small ratios.
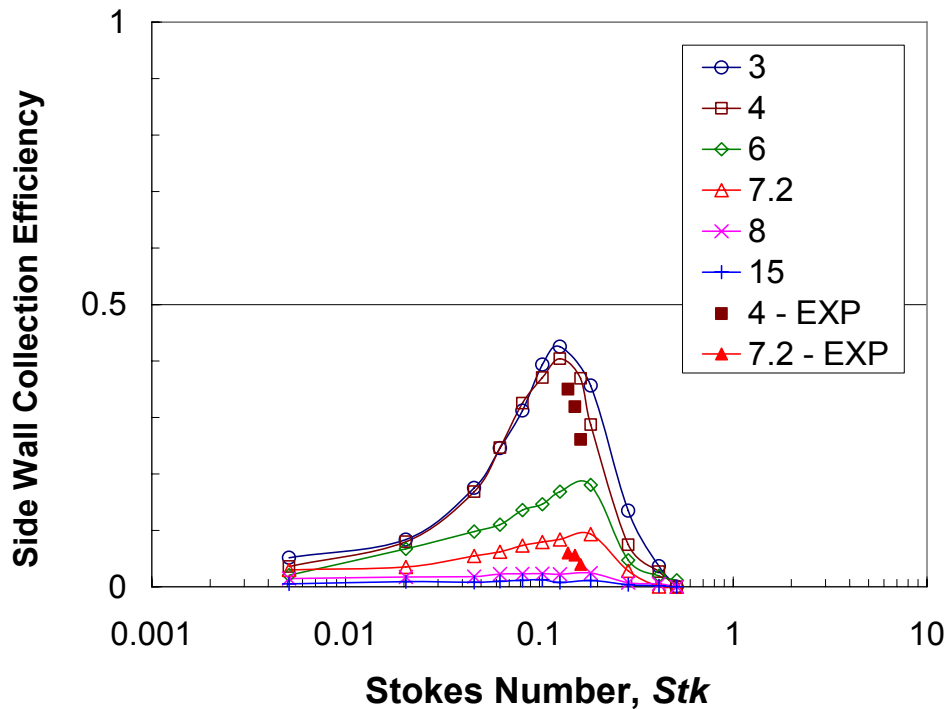
Figure 20 Side wall collection as a function of ratio of well-to-jet

3.4 Summary

The $k - \omega$ turbulent model is successfully used to design a compact size Inline Cone Impactor with a flow rate of 1250 L/min and a diameter of only 127 mm (5-inches). The cutpoint Stokes number $Stk_{0.5}$ for this type of ICI is about 0.28. Numerical predictions for the ICI are in good agreement with two variations of the impactor that were experimentally evaluated.

A compound impaction effect is characterized for circular jet-in-well inertial impactors. The compound impaction includes primary impaction under the acceleration nozzle and secondary impaction at the side wall of the cup, which can significantly enhance particle collection and results in reduced values of $Stk_{0.5}$, e.g., the cutpoint Stokes number is about 0.07 when the well-to-jet ratio is 3. Simulations were conducted for a series of jet-in-well impactors with different size ratios which showed that the side wall and the total collection will increase when the ratio decreases in a range of 3~8, beyond which the secondary side wall impaction can be ignored. The side wall impaction is demonstrated photographically and supported by experimental data.

CHAPTER IV

CYCLONE DESIGN

4.1 Introduction

Generally, flow inside a cyclone is complex and turbulent. Experiments have been conducted with Laser Doppler Velocimetry (LDV) techniques to measure the mean and fluctuating velocity components inside a cyclone. Wang et al. (2005) measured the turbulent structure of flow field and analyzed a flow wake region downstream of a stick inserted into a cyclone. Erdal and Shirazi (2004) conducted measurements at 24 axial locations in a cylindrical cyclone to understand the swirling flow behavior. Hoekstra et al. (1999) performed measurements to study the effect of geometry and swirl numbers on the flow field. These studies used the LDV technique to investigate the static flow structure in the cyclone based on local point measurement. However, there is still a lack of information about the evolution of flow structure and associated details.

Empirical models have been developed to predict particle behavior based on the understanding of flow in the cyclone or correlation of experimental data. Generally, the models can calculate particle collection efficiency, cutpoint, and pressure drop of cyclones with different geometries. Lapple (1951) included an effective number of turns in his model to calculate the cutpoint particle size. Kim and Lee (2001) considered the boundary layer effect in small cyclones in their model based on an equivalent volumetric circular cylinder. Particle motion was analyzed in the core and boundary regions. Their predictions were in good agreement with experimental efficiency but limited to small cyclones. Moore and McFarland (1993) correlated their experimental data using a

modified definition of the flow Reynolds number in developing a new model to predict the cutpoint. These models generally provide good predictions for particular cases with certain limitations. Being empirical in nature, there is a lack of discussion about the special flow structure and its influence on particles in the region where air enters the cyclone body.

Numerical simulation can be a useful tool to study cyclones. Once validated against experimental data, computational fluid dynamics (CFD) techniques can be an optimization tool to predict cyclone performance with changes in geometrical and operational parameters. In addition, results of the simulations also provide information that enhances our understanding of the flow structure and the particle behavior inside the device.

Complicated features of the turbulent, swirling flow inside the cyclone combined with curvature effects, inherent in the geometry, necessitate the use of a suitable turbulent model to capture the physics. Hoekstra et al. (1999) compared the results of flow field predictions for a cyclone obtained using different turbulence models (standard and RNG k-ε models) and Reynolds Stress model (RSM) with experimental data and concluded that reasonable agreement was obtained only with the RSM. Mathur and Murthy (1997) used the RSM and Large Eddy Simulation (LES) models in FLUENT (FLUENT Inc., Lebanon, New Hampshire, USA) to simulate flow in a cyclone and reported consistent agreement between the simulation results and the experimental velocity data obtained from LDA measurements. Results of the above studies suggest that the RSM is a suitable turbulence model to resolve the flow field in the cyclone. In

other studies performed on relatively small sized cyclones with low flow rates, collection characteristics, and pressure drop obtained from CFD predictions are in relatively good agreement with experimental data (Gimbun et al. 2005 and Griffith and Boysan 1996).

Some studies were focused on the cyclone to understand its heat transfer feature by experimental measurements and empirical models developed. Akpinar (2005) evaluated the convective heat transfer coefficient in a cyclone type dryer to investigate the effect of drying air velocity and temperature on the convective heat transfer. Gupta and Nag (2000) developed an empirical model to predict the heat transfer coefficient in the cyclone of a circulating fluidized bed and obtained good agreement with measured data. CFD has also been used in many studies to successfully predict turbulent heat transfer. Yang et al. (2006) simulated heat transfer on a turbine blade using FLUENT and their predictions for heat transfer coefficient on the blade tip and suction side agreed reasonably with their experiment measurements except there was about 25% over-prediction on the pressure side. Lin et al. (2001) studied heat transfer in a U-shaped duct of a square cross section at a Reynolds number 25,000 using numerical techniques based on the finite volume method and showed how the flow nature affected the surface heat transfer. However, at the present time there is a lack of information about the numerical simulation of turbulent heat transfer in air sampling cyclones.

In this study, numerical techniques are used to model the performance and design of four different bioaerosol sampling cyclones, focusing on different problems and objectives. In contrast with traditional cyclones, these bioaerosol sampling cyclones have some special features. Air flow through the cyclone is axial and liquid (water) is

continuously injected into the cyclone at a very small flow rate, which forms a thin film onto which bioaerosol particles are deposited and continuously transported out of the cyclone. The liquid film is developed by the shear force provided by the air flow due to the high velocity gradient existing near the wall. Generally, there is a clear interface between the air and the liquid, i.e., the two-phases do not intermingle.

Experimental and numerical studies have been conducted in the past to understand the mechanism of liquid film formation and the influence of such factors as air and liquid flow velocity, etc. Ataki and Bart (2004) studied laminar rivulet flow on flat and wavy plates using the VOF model in FLUENT. Their predictions were found to be in good agreement with measured liquid film thickness and width. Gu et al. (2004) studied the formation of a liquid film on an inclined plate and analyzed the effect of influencing factors such as plate structure, liquid property, and gas flow rate on the film.

A wetted-wall bioaerosol sampling cyclone, which will be referred to herein as CYC-A, was developed by Black and Shaw (2002) for operation at a sampling flow rate of 780 L/min and a liquid outflow rate of 1.6 mL/min. During operation of this cyclone, Moncla (2005) observed that liquid would periodically be carried over into the exhaust air stream and this could cause the sampling efficiency (aerosol-to-hydrosol) to approach zero. In the present study, liquid carry-over was simulated using a volume of fluid (VOF) model in FLUENT. Development of the liquid film inside the complex cyclone geometry was modeled, which allowed the problem to be analyzed. The cyclone was redesigned to eliminate the liquid carry-over problem.

For an upgraded version of cyclone, which will be referred to herein as CYC-B, the air flow rate was increased to 1250 L/min yet the output liquid flow rate was reduced to 1.0 mL/min. Additional studies on this upgraded cyclone were directed towards characterizing its liquid atomization and droplet cooling in cold air, aerosol-aerosol particle collection, pressure drop, flow structure, and heater design. Evolution of the air flow within the upgraded cyclone is illustrated with appropriate figures and a special inward jet flow structure is demonstrated. Simulations of collection efficiency curves, pressure drops, and temperature response of the cyclone wall, are compared with experimental data.

Based on these simulation results, a double-outlet cyclone, referred to herein as CYC-C, was designed with the objective to reduce the pressure drop. This cyclone was fabricated and tested and the pressure drop was compared with CYC-B.

A scaled 100 L/min cyclone, which will be referred to as CYC-D, was designed to obtain a similar cutpoint to the 1250 L/min cyclone (CYC-B) and pressure drop that would be less than about 1250 Pa (5 inches of water).

4.2 CYC-A: Liquid Film Study

The CYC-A bioaerosol sampling cyclone was developed by Black and Shaw (2002). This cyclone is designed to have a nominal flow rate of 780 L/min with cutpoint around 1.0 μm aerodynamic diameter (AD). The inlet tube is 19.05 mm (0.75-inches) diameter, which provides a Reynolds number of about 32,000. The average flow velocity is 46 m/s at the entrance slot and the cyclone body has a diameter of 28.575 mm (1.125-inches) and a diameter of 38.1 mm (1.5-inches) at the skimmer, Figure 21. A special

feature of CYC-A cyclone is that the liquid skimmer connects to the cyclone in an expansion region, which was intended to reduce the pressure drop of the whole cyclone, Figure 22.
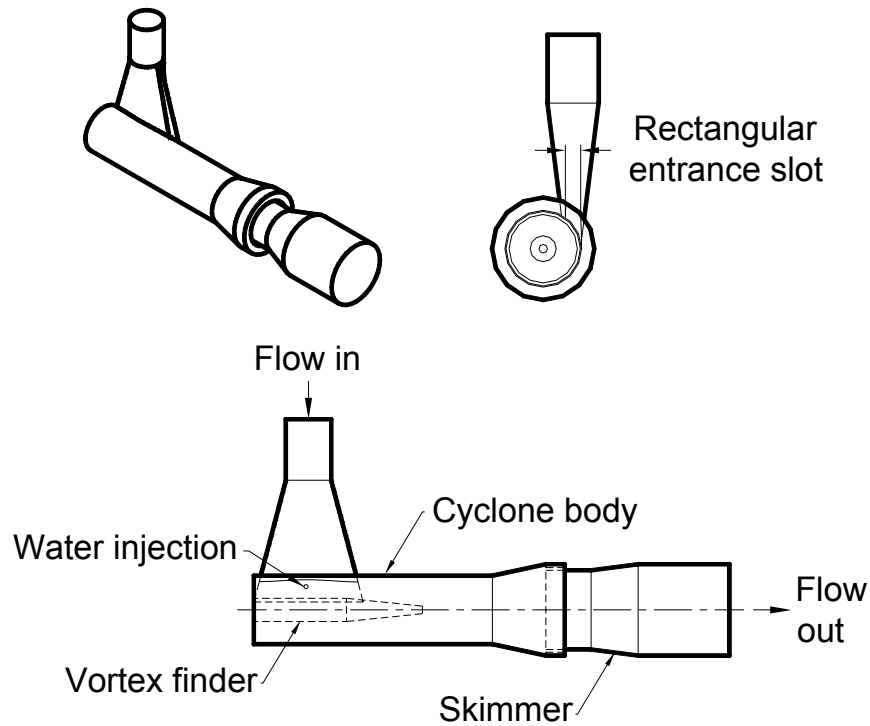
Figure 21 Layout of CYC-A cyclone

Liquid is injected into the cyclone through a small hole with diameter of 0.33 mm (0.013-inches), which is located near the entrance slot. The stream of the liquid is expected to be atomized by the high velocity main air to form small droplets spraying onto the main deposition surface, and forming a film that will act as a collection surface for bioaerosol particles that reach the wall. The process of atomization is determined by

two factors, the liquid jet velocity and the main air velocity. The main air flow should have a high velocity to effect atomization of the liquid. However, the velocity of the liquid jet should also be fast enough so the jet will reach the high velocity region of the main air. If not, the liquid will travel down the wall as a rivulet in the boundary layer.

During experiments with the CYC-A bioaerosol sampling cyclone, it was observed that a ring of water existed in the region just upstream of the intake zone of the skimmer, Figure 22. The water ring, present under normal sampling conditions, could not easily be eliminated by simply changing air or liquid flow rates. Experimental visualization suggested the presence of the ring appeared to be at least partially responsible for causing liquid carryover into the exhaust air stream. Simulations were conducted to analyze this problem and to find possible reasons for the formation of the ring. The cyclone has a complex internal geometry, and the liquid film on the cyclone wall is very thin (on the order of a few tens of micrometers) in the region where particle impaction takes place. For the VOF model, the water side should contain several cells in the direction normal to the wall. This implies that the cell size must be very small (on the order of micrometers in thickness). This requirement would make a study of the film formation, with a 3D VOF model, very difficult if the entire cyclone cross section were to be taken into account.
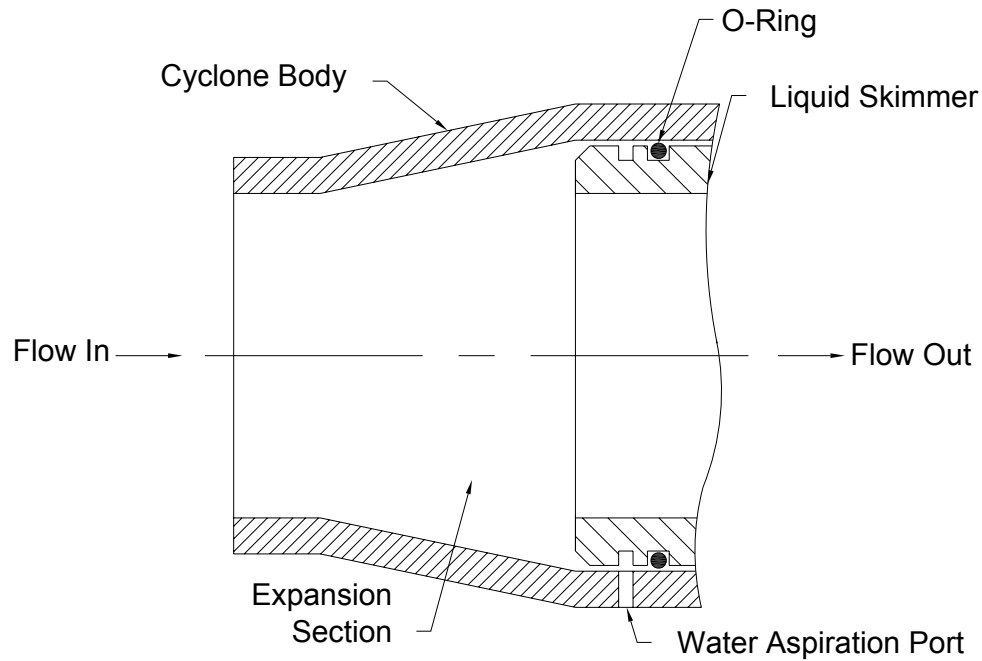
Figure 22 Cross sectional view of liquid skimmer region of the earlier version of cyclone

The shell-volume concept was used to simulate the evolution of the liquid film near the skimmer region of the cyclone. First, a mesh with about 1.1 million unstructured cells was used to simulate the CYC-A cyclone to get the whole flow field, Figure 23. A thin shell, about 300 μm thick, was cut along the wall where water rivulets flow and where the water ring is located. The air velocity distribution on the outer surface of the shell was achieved from the whole flow simulation and stored for use in VOF simulations.
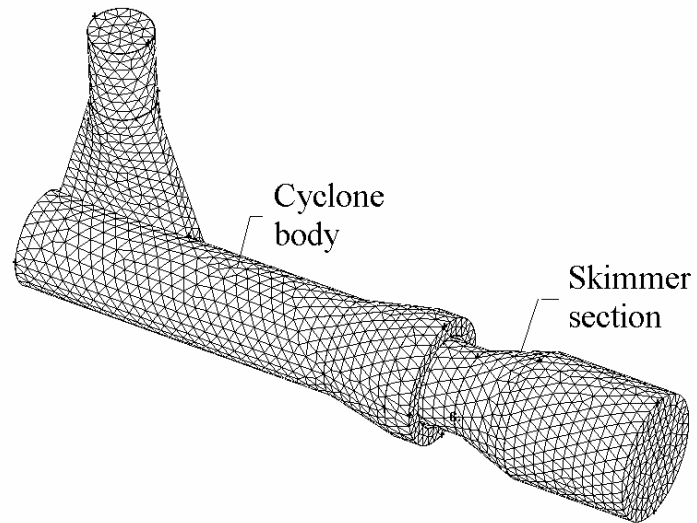
Figure 23 Numerical mesh used for calculating air flow field in the CYC-A sampling cyclone

Second, VOF was used to simulate the cut shell with its outer boundary set by the velocity profile transferred from the first step. With reference to Figure 22, the skimmer of the CYC-A cyclone is preceded by a flow expansion. Visualization of water streak-lines, Figure 24, shows liquid flow anomalies in this region. It may be noted on the left (upstream) side of Figure 24, there are several black lines, which are flowing rivulets of water. At the location where the rivulets terminate, there is a ring of liquid that continuously rotates.
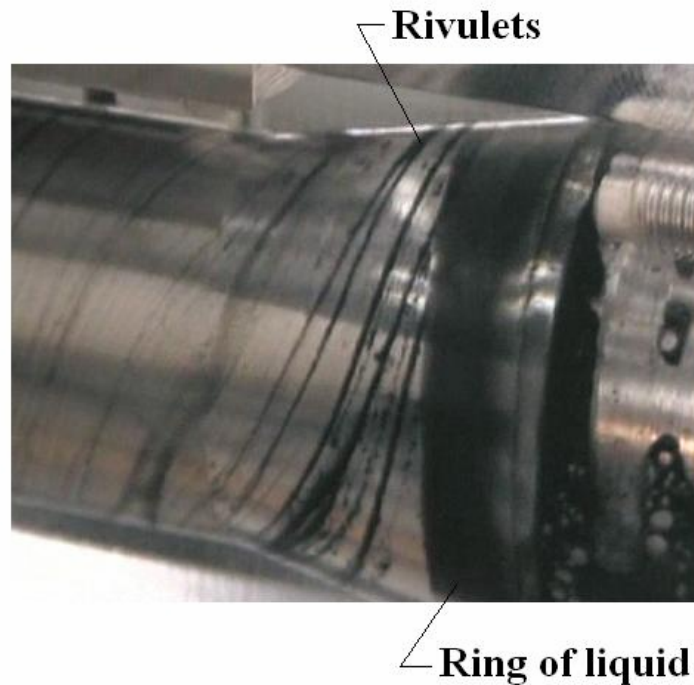
Figure 24 Photograph of the earlier cyclone with India ink added to water for contrast. Airflow is from left to right. The ring of liquid forms just upstream of the skimmer

Figures 25 and 26 show air and water streak-lines in the skimmer region obtained from the results of the VOF simulation for the geometry of CYC-A. Qualitative similarities in the liquid streak-lines between the numerical and experimental results are evident from a comparison of Figures 24 and 26. As the air flow approaches the inlet of the skimmer, the expanding geometry causes the axial velocity to decrease rapidly. In this region, the air stream does not provide a sufficient shear force to drive the film forward through the gap between the cyclone wall and skimmer body, which causes the rotating water ring to be formed. It can be observed in Figure 26 that, when the water rivulets approach the upstream region of the skimmer, there is an abrupt change in the direction of motion, i.e., the axial component is significantly reduced.
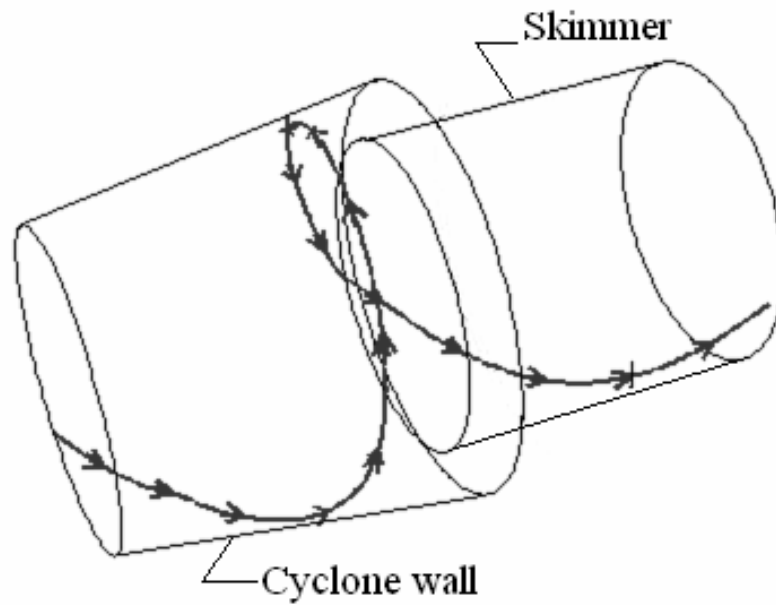
Figure 25 Numerically simulated streak-lines of air in the outlet region of the earlier version of the cyclone
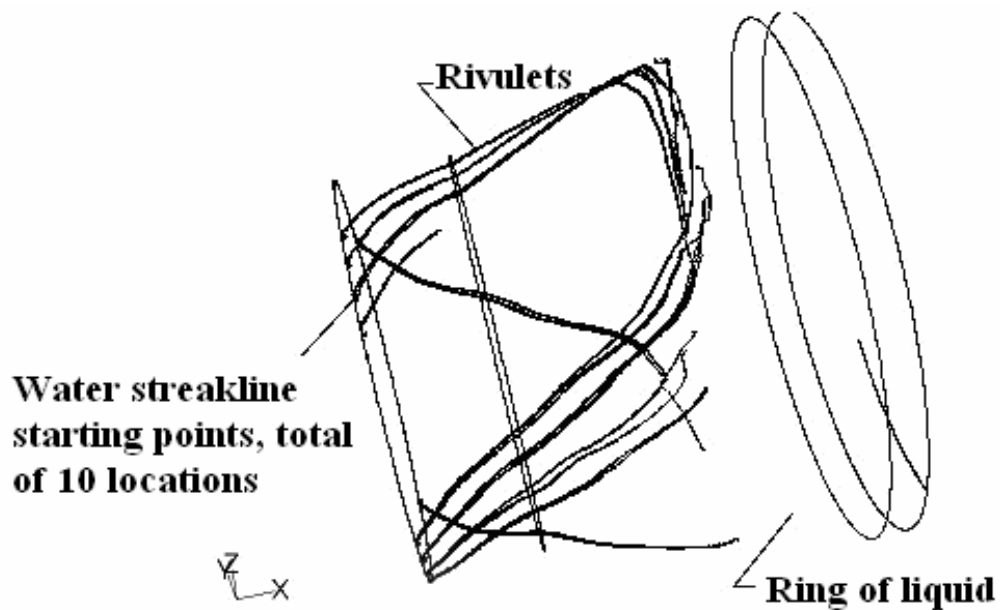
Figure 26 Numerically simulated streak-lines of water in the outlet region of the earlier version of the cyclone

The presence of the water ring suggested that a modification to the skimmer geometry was needed. To this end, the flow expansion just upstream of the skimmer inlet was eliminated and the cyclone body was made larger. The increased size was needed to avoid increased pressure drop across the cyclone that would have resulted from the use of a smaller skimmer diameter with the same cyclone body size. Because of the increased body diameter, the cyclone flow rate could also be increased from a nominal value of 780 L/min to 1250 L/min, without an inordinate increase in pressure loss. Experimental evaluation of this upgraded cyclone indicated that the liquid ring and the liquid carryover problem were eliminated.

4.3 CYC-B: 1250 L/min Cyclone

The CYC-B cyclone is an upgraded unit version of CYC-A, which among other considerations, was designed to eliminate the water bypass problem. In CYC-B, air is introduced into the cyclone and accelerates in the inlet section, then enters the cyclone body through an elongated slot, moves in the axial direction, and exhausts just downstream of the liquid skimmer. Liquid (water) is continuously injected into the cyclone as a mist, which is created by air blast atomization. The flow rate of the liquid is about 1.5 mL/min. The atomized liquid droplets are carried into the cyclone by the air stream, where they are impacted on the cyclone wall, and then form the thin film, onto which the bioaerosol particles are impacted. As the liquid flows through the cyclone, it forms rivulets that are skimmed from the wall, and the collected liquid is then aspirated from the cyclone.

CYC-B is designed to operate at a nominal flow rate of 1250 L/min with a cutpoint of about 1.0 μm AD, corresponding to a flow Reynolds number about 28,000 at the inlet, where the diameter is 63.5 mm (2.5-inches). The average flow velocity is 52 m/s at the entrance slot and the cyclone body diameter is 38.1 mm (1.5-inches), Figure 27. CFD was used to predict the flow conditions and particle behavior in this cyclone and the results are compared with experimental tests. Also, empirical models and CFD are used to calculate the temperature behavior of the atomized water droplets.
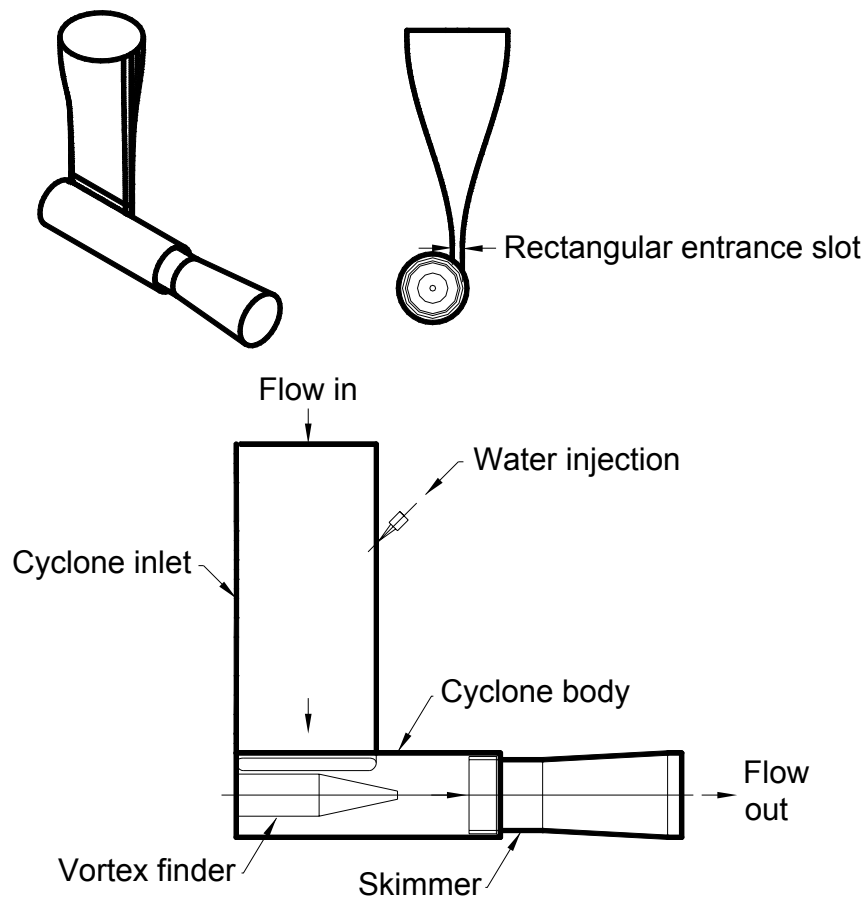
Figure 27 Layout of CYC-B cyclone

The computational mesh used to characterize CYC-B cyclone contains about 1.2 million unstructured cells, Figure 28. Since a RSM model is used for turbulent flow calculation, the standard wall function is used with a y^+ value of between 40 and 60.
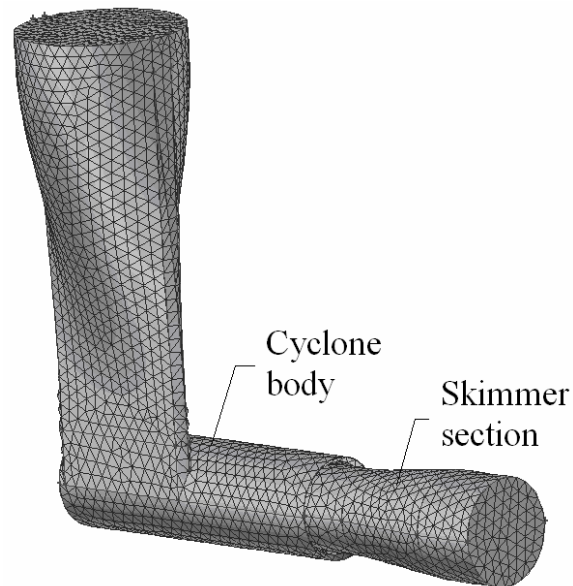
Figure 28 Unstructured mesh for CYC-B cyclone

4.3.1 Water Droplet Cooling

When the cyclone is operated in sub-freezing air, the freshly-formed liquid droplets should not freeze during the period between formation and impaction on the cyclone wall. Here, a theoretical analysis was used to calculate the temperature response of the liquid particle to verify that the droplets would not freeze.

Empirical models were used to find the mean particle size of the droplets after atomization, to calculate the transit time, which is defined as the time period during

which the droplets travel from the point of formation to the point of deposition, and to calculate the cooling time of the particles, which is defined as the time period during which the temperature of the droplets decrease from 20°C to 0°C.

Water is injected into the cyclone inlet section through a capillary tube, where it is atomized by compressed air from a second capillary tube. The velocity of the compressed air is high as the pressure drop across its needle is 34.5 kPa (5 psi). A model of Jasuja (1979) was used to calculate the mean size of water particles during this atomization process.

$$D_{mp} = 10^{-3}(1+\frac{1}{ALR})^{0.5}[\frac{(\sigma\rho_w)^{0.5}}{\rho_a U_a} + 0.06(\frac{\mu_w^2}{\sigma\rho_a})^{0.425}] \tag{50}$$

After atomization, droplets travel from the cyclone inlet toward the cyclone body and are deposited on the cyclone wall. During this period, the water particles are carried by the sampled air flow and they will be cooled down if the sampled air is cold. It is assumed that only drag force and gravity will act on the water droplets and determine their motion during their transit period.

For the cooling process of the water particle, flow over a sphere model suggested by Whitaker (1972) was used to calculate the average Nusselt number and the LUMPED model (Mills, 1999) could be used to calculate temperature response of the droplets because they have a small Biot number of about 0.077 (less than 0.1).

$$N_u = 2 + (0.4\,\mathrm{Re}_p^{0.5} + 0.06\,\mathrm{Re}_p^{2/3})\,\mathrm{Pr}^{0.4} \tag{51}$$

$$h = \frac{N_u K_a}{D_p} \tag{52}$$

$$Bi = \frac{h D_p}{K_w} \tag{53}$$

$$\frac{T - T_a}{T_o - T_a} = e^{-bt} \tag{54}$$

$$b = \frac{hA}{\rho_w V C_p} \tag{55}$$

The sampling cyclone is used to collect the bioaerosols on a wetted-wall and a special requirement for this cyclone is that the region of the wall where collection takes place should be optimally covered by the water during operation. In an earlier application (Black and Shaw 2002), water was injected into a cyclone through a small hole with a diameter of about 0.33 mm (0.013-inches) and the total bioaerosol recovery efficiency was only about 60% for particle sizes where the maximum efficiency could be 100%. The reason is possibly that the wall was not suitably wetted. In the present application, water was injected into the cyclone and atomized by a dedicated stream of high-velocity air from compressed air. After atomization, the small water particles disperse in the inlet section of the cyclone and are then spatially distributed to cover the majority of the wall surface where impaction takes place. For atomization, the pressure of the compressed air was set at 34.5 kPa (5 psi) and the corresponding mass flow rate of the air was maintained at 64.3 mg/s through the 0.585 mm (0.023-inch) I.D. air needle. The water was pumped into the cyclone through a 0.152 mm (0.006-inch) I.D. water needle at a flow rate of 23.3 mg/s (1.5 mL/min), Figure 29. Calculations with Equation (50) show that the mean diameter of the water particles was 42 μm. The water droplets travel a distance of about 116.84 mm (4.6-inches) between the point of atomization and the point of deposition.
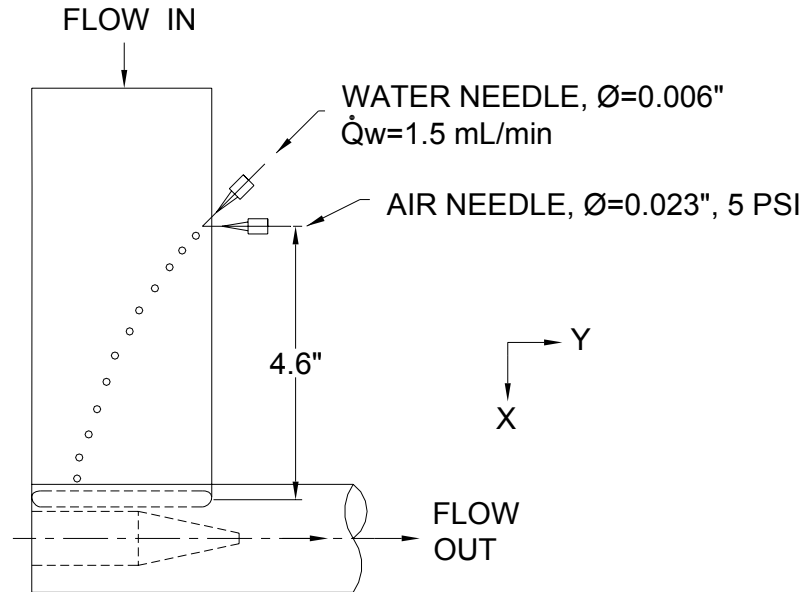
Figure 29 Schematic drawing of air and water needles

During the transit period, water particles can be cooled down by the main air flow. Average velocity of the main air flow in the X-direction is determined by geometry of the cyclone inlet, Figure 30. This average velocity will determine the water droplet motion and the heat transfer coefficient for the droplet surface. The initial velocity of the water particles V_{XO} is calculated from momentum conservation in the X-direction considering the momentum of air and water from the respective needles.

$$(\dot{m}_a + \dot{m}_W)V_{XO} = \dot{m}_a V_{aX} + \dot{m}_W V_{WX} \qquad (56)$$
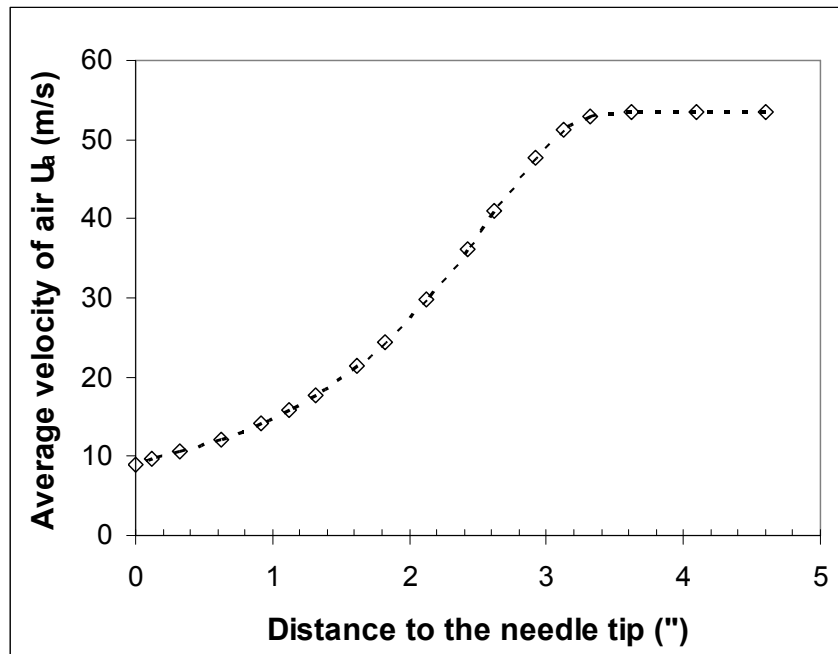
Figure 30 Average velocity of air in the inlet section of the cyclone as a function of distance to the tip of the needles along the X-direction

Transit time and cooling time for different water particle sizes are calculated based on the conditions that water droplets have an initial temperature of 20°C and the main air temperature is -40°C. The results of these calculations for different droplet sizes are shown in Figure 31, where it can be observed that droplets with sizes larger than 33 μm will not freeze during the transit period. The transit time for the 42 μm water particles predicted to be produced by the air blast atomization process is only about 3.0 ms while the cooling time will be 5.1 ms. After the 42 μm particles reach the cyclone wall, the particle temperature is about 6.4°C, which means that the water particles will not freeze during their transit and they will reach the cyclone wall in liquid phase. This conclusion was verified in experiments with similar conditions where the incoming cold air temperature was -40°C, and water at room temperature 20°C was injected into the

cyclone. A boroscope was used to observe inside the cyclone and it verified that only liquid was found to have reached the cyclone wall.
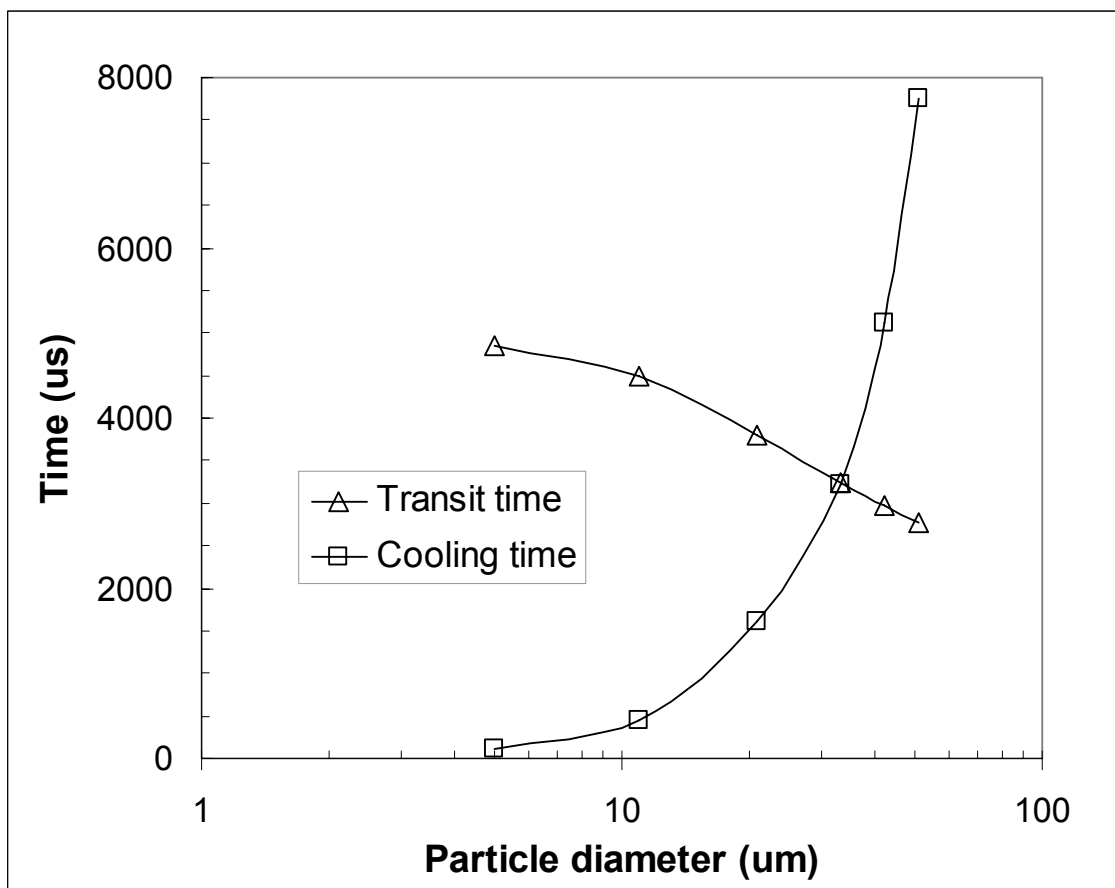
Figure 31 Comparison of transit time and cooling time as a function of particle size in the inlet section of the bioaerosol sampling cyclone

4.3.2 Cyclone Flow Field and Particle Behavior

Aerosol collection and pressure drop were numerically predicted for the upgraded cyclone at seven air flow rates, which provide a range of flow Reynolds numbers of approximately 16,000 to 32,000. For each flow rate, 12-15 different sizes of

particles were used to generate aerosol-to-aerosol collection curves. Each efficiency data point was based on the release of 2200 particles. Results of the simulations showing collection efficiency as a function of Stokes number are presented in Figure 32. For comparison, experimental aerosol-to-aerosol collection efficiencies are shown for both CYC-A (earlier cyclone) and the CYC-B (upgraded cyclone), where it may be observed that the aerosol-to-aerosol collection efficiencies of the two cyclones are similar over the range of Stokes numbers evaluated. The numerical predictions are in good agreement with the experimental data except the numerical simulations give slightly higher efficiency values than the experimentally observed results, which may be caused by additional particle losses in the experiments in such physical components as filter holders. The value of cutpoint Stokes number, $Stk_{0.5}$, is small (~0.05) over the range of Reynolds numbers considered, and the efficiency curves are essentially independent of Reynolds numbers.
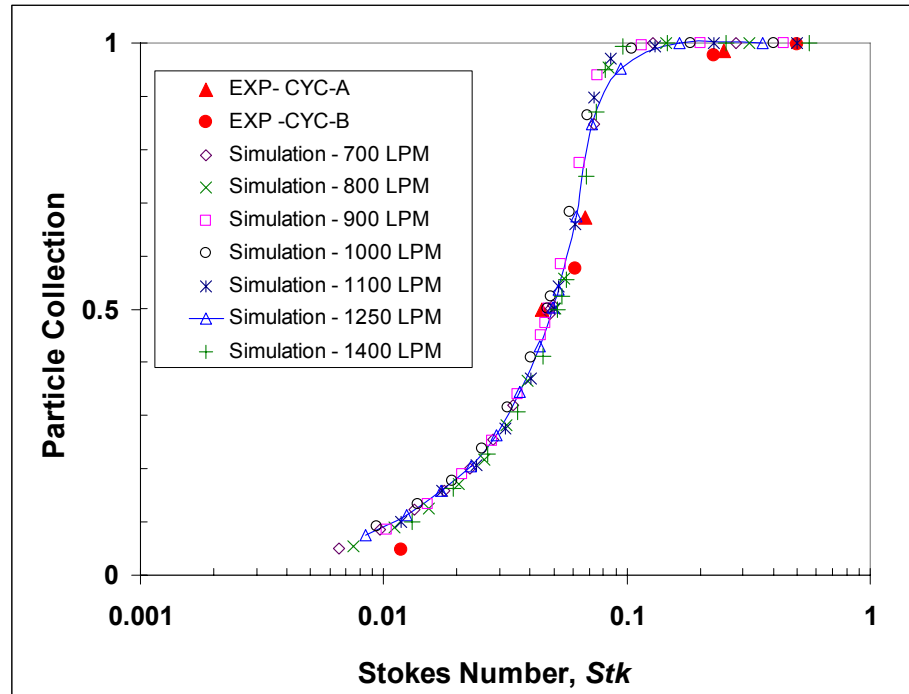
Figure 32 Particle collection efficiency of the wetted-wall bioaerosol sampling cyclones as a function of Stokes number. Simulation data is for the CYC-B cyclone only. The curve is drawn through the predicted points for the flow Reynolds number of 28,000

The data for the predicted collection efficiency forms a relatively sharp curve, which is typical of an air sampling cyclone. The slope of the efficiency curve, which is shown in the log-log plot of Figure 32, is approximately constant for efficiency values less than unity, i.e.:

$$\frac{d\log(\eta_{AA})}{d\log(Stk)} \approx 1.14 \qquad \text{For } Stk \leq 0.092$$

$$\eta_{AA} = 1 \qquad \text{For } Stk > 0.092 \qquad (57)$$

Where η_{AA} is the aerosol-to-aerosol collection efficiency. The slope value of the efficiency curve, which is 1.14, is an indication of the sharpness of the fractional

efficiency curve based on Equation 57, where a larger slope corresponds to a steeper collection curve. If the sharpness of the cyclone is calculated using $(D_{84}/D_{16})^{1/2}$, as suggested by Kenny and Gussman (2000), where D_{84} and D_{16} represent particle aerodynamic sizes having collection efficiency values of 84% and 16%, respectively, the sharpness value is about 1.45.

The pressure drop, ΔP, as a function of flow rate is shown for the earlier CYC-A and the upgraded version CYC-B cyclones in Figure 33. Also shown is a numerically predicted curve for the upgraded CYC-B system. In general terms, at the same flow rate, the pressure drop across the earlier cyclone is about 2.5 times that of the upgraded system. The lower pressure drop across the upgraded system is primarily due to a modification in the design of the entrance region upstream of the cyclone body (Figure 28) and the increase in body diameter. At the nominal operation condition of 780 L/min, the pressure drop across the earlier version of the cyclone is 5.0 kPa, and at the nominal flow rate of 1250 L/min, the pressure drop across the upgraded cyclone is 5.6 kPa. The numerically predicted pressure drop values for the upgraded cyclone are in excellent agreement with experimental data, with the difference being typically less than 10%.
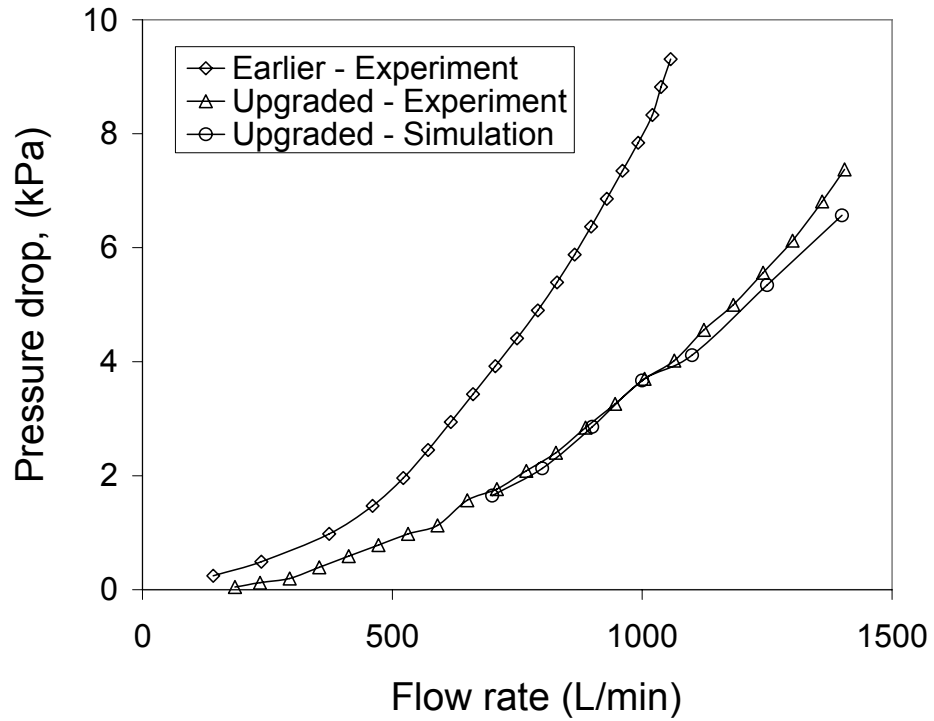
Figure 33 Pressure drop across wetted-wall cyclones

Knowledge of the pressure drop is important for bioaerosol sampling cyclones that are to be used in the field because it is a direct measure of the ratio of ideal power (not taking into account power losses in the motor/blower) to flow rate, i.e.:

$$\Delta P = \frac{\dot{W}_{ideal}}{Q} \tag{58}$$

where $\dot{W}_{ideal}$ is the ideal power. At the flow rate of 1250 L/min, the ideal power for the upgraded cyclone is 117 W, whereas the ideal power for the earlier cyclone at 780 L/min is 65 W. However, if the earlier cyclone were to be operated at a flow rate of 1250 L/min, the ideal power would be 292 W.

As shown in Figure 32, the value of $Stk_{0.5}$ for the sampling cyclone is about 0.05. In modeling reverse flow cyclones, it is generally assumed that the air flow enters the cyclone at a velocity of U_i and then spirals along in the axial direction with the centrifugal force driving particles to the wall (Lapple, 1951; Fuchs, 1964) until the flow reversal takes place, which for a typical Lapple cyclone is assumed to take place after about 6 turns of the air flow. However, that description of the principle of operation may not be appropriate for this cyclone design, where aerosol particle deposition takes place on a small area of the inner wall, which is approximately defined by the slot length and the first half-turn of the air flow. Outside of this region, almost no particles are deposited even if they are still in the aerosol state and are subjected to the centrifugal force for a number of rotations of the air stream in the cyclone body. If the cutpoint Stokes number is calculated from the Lapple model with an assumption that the flow undergoes ½ turn, the result is a value of 0.6.

In some respects, this type of bioaerosol sampling cyclone behaves more like a classical impactor because deposition takes place on a small area of the cyclone body as a result of particle inertia in a curvilinear flow field. If the particle stopping distance is greater than a reference distance, e.g., ½ of the slot width, deposition is likely. Because the ratio of the stopping distance to a reference dimension is the Stokes number, aerosol particle collection is Stokes number dependent. However, the model of Lapple, which is based on centrifugal force effects, is also expressible in terms of the Stokes number. Essentially both models take into account aerosol particle behavior in curvilinear flow,

with the main difference being that the deposition is assumed to occur over a much greater extent of the cyclone body in the Lapple model.

For the wetted-wall bioaerosol sampling cyclone, the cutpoint Stokes number is about 0.05, which is substantially lower than the cutpoints of classical round and rectangular jet impactors, as the latter have $Stk_{0.5}$ values of about 0.24 and 0.59, respectively (Hinds, 1999). We believe the much smaller $Stk_{0.5}$ for the cyclone is caused by special flow features downstream of the rectangular entrance slot in the cyclone, namely a narrowing of the inlet jet and inward directed radial flow along the slot length.

To demonstrate the flow structure in this region, three computationally-generated stream-tubes of air from different locations along the rectangular entrance slot are illustrated in Figure 34. With reference to the axial flow in the cyclone, the left stream-tube is upstream of the right one. First, it may be noted that the stream-tubes narrow substantially as they enter the cyclone body. Second, it can be seen that the left stream-tube is forced inward (toward the vortex finder) by the next stream-tube, and that stream-tube is also forced inwards by the succeeding stream-tube. With respect to the narrowing of the stream-tubes in Figure 34, the effect causes an increase in velocity of about 1.5X that of the velocity based on flow rate and rectangular entrance slot area. Also, the particles have a shorter distance to travel to impact onto the wall than the distance based on the slot width. These two factors tend to make the particle collection more efficient than it would be inferred from use of the Stokes number calculated from the slot area and volumetric flow rate. However, after the first turn, when an air spiral becomes covered by outer air spirals, the particles will have little chance to reach the wall,

because the distance to the wall is greater than in the first turn. Based on this flow structure, the majority of particle deposition occurs on the wall immediately downstream of the rectangular entrance slot, i.e., during the first half-turn. The section of the wall downstream (right side) of the slot, Figure 34, collects few particles. This deposition pattern phenomenon was observed in an experiment with the earlier wetted-wall cyclone where we operated the cyclone with no liquid flow while sampling 2 μm polystyrene spheres (PSL) that were tagged with fluorescent tracer. Analysis of the regional deposition in the cyclone showed the majority of the PSL particles were deposited in a cylindrical sector that is approximately bounded by the rectangular entrance slot length and an angle of about 180 degrees.
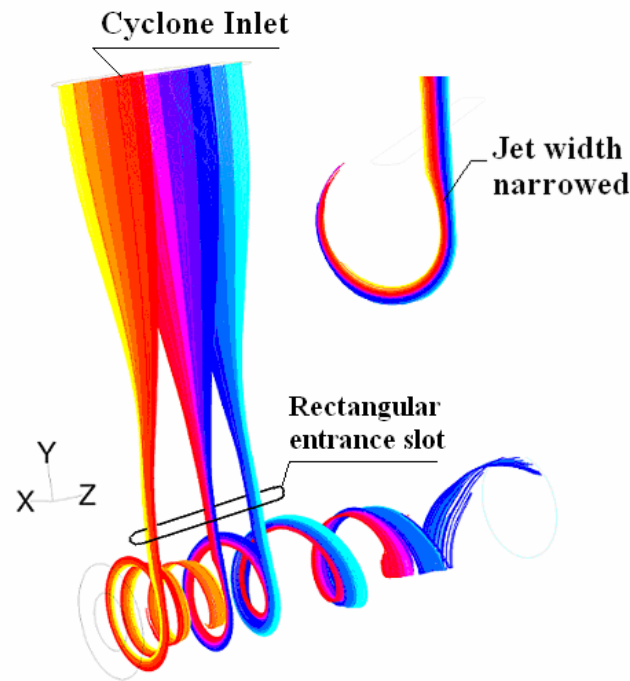

Figure 34 Stream-tubes, which narrow as they enter the cyclone and spiral inward as they pass through the cyclone body

4.3.3 Heater Design

When the water droplets reach the CYC-B cyclone wall, they form a film that, in turn forms rivulets, which flow along the wall and are aspirated at the skimmer port. When the cyclone is operated at sub-freezing temperatures, heaters must be provided to prevent freezing of the liquid on the cyclone wall. The temperature of the whole cyclone wall should be maintained in a suitable range, as too high of a temperature may damage bioaerosol organisms and cause excessive liquid evaporation, and too low of a temperature would cause freezing of the liquid. For this particular cyclone application the total power budget for the heaters was limited to about 320 W.

The strategy chosen for heating was to divide the cyclone into zones, and provide appropriate electrical heating to each zone. The power of each heater should be determined by the local turbulent heat transfer coefficient, $h(x, y, z)$ which determines the local heat flux and the total heat flux in sequence. The $h(x, y, z)$ varies over the area of the internal wall of the cyclone because the velocity of the free stream cold air varies between the cyclone inlet to the outlet.

$$\dot{q}'' = h(x, y, z)(T - T_a) \tag{59}$$

$$\dot{Q} = \int \dot{q}'' dA \tag{60}$$

$$P_{Heater} = \dot{Q} / \eta_{Heater} \tag{61}$$

Here, T is the local temperature of the cyclone wall, T_a is the temperature of the free stream air, $\dot{Q}$ is the total heat flux input into the cyclone, and P_{Heater} is the total power of the heaters. The parameter η_{Heater} is used to represent the efficiency of the heaters, which

is determined by the inner contact resistance and outer insulation layer of the heaters. The heaters should tightly contact the cyclone outer wall to reduce the contact resistance and this is realized by gluing a layer of highly thermal conductive material between the heaters and the cyclone wall. The heaters should also prevent heat from flowing outward into the surrounding area. This is accomplished by embedding the heaters in a rubber-like material which allows the heaters to be tightly attached to the cyclone wall and provides a degree of thermal insulation.

For the period during which the liquid film flows along the wall in CYC-B, the CFD technique was used to determine the turbulent heat transfer coefficients on the cyclone surface, to design heaters, and to predict the temperatures of the cyclone wall and the liquid film. The water film on the cyclone wall is assumed to be very thin (about 20-30 μm) so heat resistance of the water film is ignored. It is reasonable to assume that the presence of this thin water film will not affect the general flow structure and heat transfer features of the cyclone, i.e. the presence of the liquid film can be ignored and calculations involving only cold air and the cyclone wall will represent the physical heat transfer process. The process of simulation includes several steps (see Figure 35):

(1) Flow field calculation: Shown in blue in Figure 35, the geometry of the internal volume of the cyclone was used to simulate the air flow. Based on the fluid field results, the turbulent heat transfer coefficient $h(x, y, z)$ at the wall surface is calculated. The mesh for the flow calculation contains about 1.1 million unstructured cells.

(2) Solid wall calculation: Shown as green in Figure 35, both convection and conduction for the solid wall of the cyclone are considered and the temperatures of the wall are calculated based on the transferred $h(x, y, z)$ values from Step 1. Mesh for the cyclone wall contains about 1.2 million mixed cells.

(3) Wall temperature check: Check the temperature on the cyclone wall and adjust the power of the heaters to verify the temperature of the wall is suitable and satisfy the relative requirement. For the unsteady thermal response, the temperature of the cyclone wall is recorded for comparison against experimental measurements.
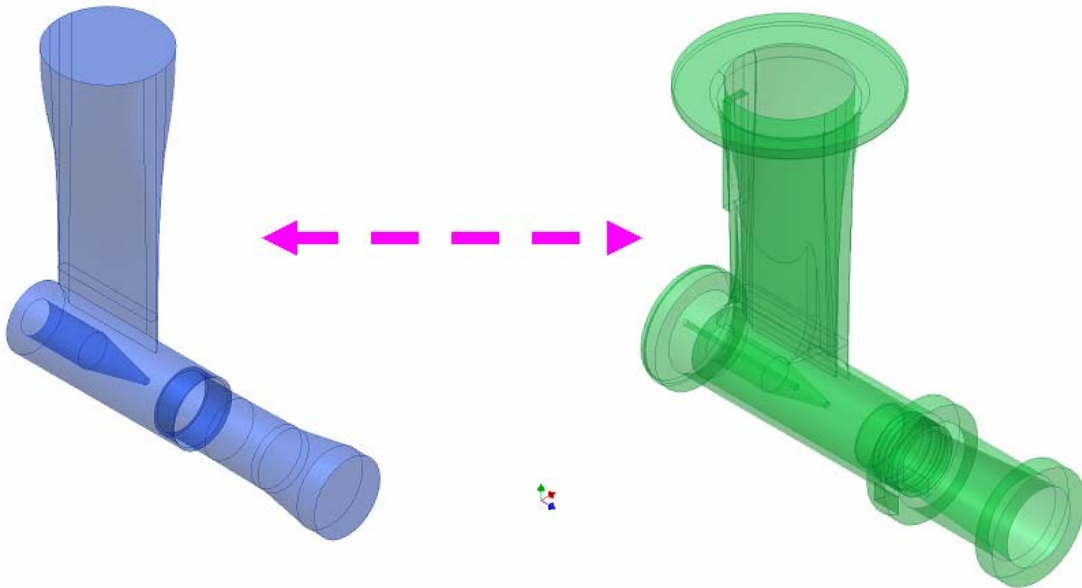
Figure 35 Inside volume (blue) and metal wall (green) of CYC-B cyclone. A mesh of about 1.1 M cells was used to characterize the flow field and determine the convective heat transfer coefficients (blue). The temperature distribution in the solid wall (green) was calculated based on the values of the heat transfer coefficients

Figure 36 shows the distribution of the turbulent heat transfer coefficient $h(x,y,z)$ on the internal wall of the cyclone. It can be seen that $h(x,y,z)$ varies over a wide range of 20 to 300 W/(m²·K). The inlet section has smaller h values because of relatively slower local air velocities (~8 m/s) and the cyclone body has higher values because of higher air velocities (~60 m/s). The difference of the $h(x,y,z)$ values for the two regions suggests that non-uniform heating intensity should be applied for heaters to match the local heat exchange rates. Prediction of $h(x,y,z)$ is most important in this cyclone heating study because it determines the convective heat transfer coefficient in the solid wall simulation. The Gnielinski (1976) formula was used to check the predicted turbulent heat transfer coefficient at the elongated slot.

$$Nu = \frac{\frac{f}{8}(\text{Re} - 1000)\,\text{Pr}}{1 + 12.7 * (\frac{f}{8})^{0.5}(\text{Pr}^{2/3} - 1)} \tag{62}$$

$$\text{Re} = \frac{\rho_a D_h U_a}{\mu_a} \tag{63}$$

Where D_h uses the width of the slot and f is the friction factor calculated from the Petukhov (1970) formula,

$$f = (0.79\ \ln \text{Re} - 1.64)^{-2} \quad \text{For } 10^4 < \text{Re} < 5 * 10^6 \tag{64}$$

Based on these formulas, the h value at the elongated slot is 250 W/(m²·K) and it agrees well with the predicted value from simulation (~246 W/(m²·K)).
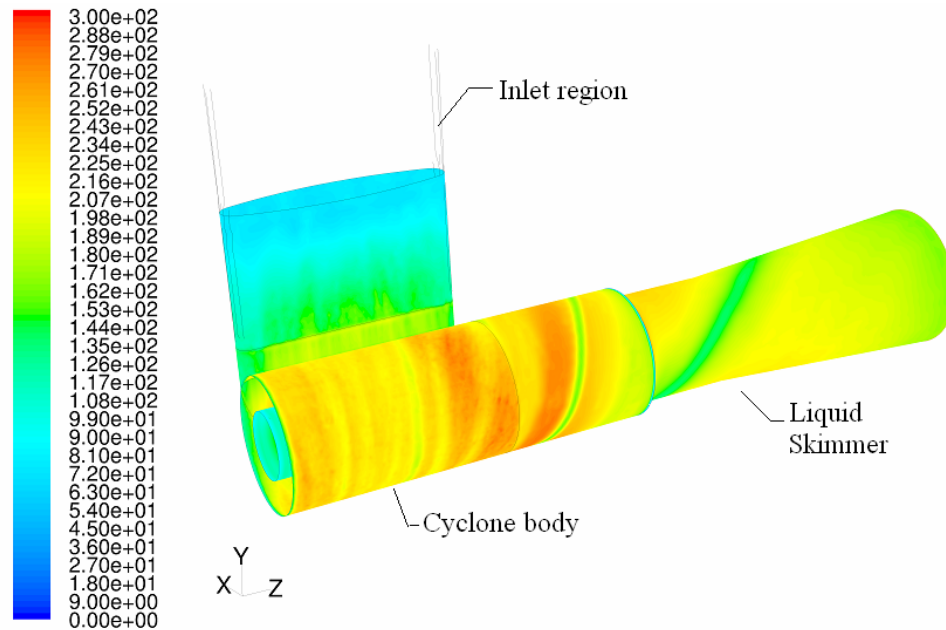
Figure 36 Distribution of turbulent convective heat transfer coefficients on the inner wall of the cyclone

With the consideration of non-uniform distributed heat transfer coefficients on the wall of the cyclone, the heaters should be provided with power inputs that correspond to the $h(x, y, z)$ local values, i.e., the heat flux i, should track the local heat transfer coefficient. If local flux i is much less than indicated by $h(x, y, z)$, then the liquid could freeze. If i is much higher than suggested by the local $h(x, y, z)$, then the wall temperature could be too high and result in bioaerosol damage, excessive liquid evaporation and a waste of electrical energy. However, from the standpoint of fabrication costs, use of a large number of heaters should be avoided. As a consequence, the cyclone wall was divided into four sections which have similar values of $h(x, y, z)$

inside each section. The power provided to each heater was based on CFD predictions. A cartridge heater was inserted into the vortex finder and three flat heaters were wrapped on the cyclone wall. For each flat heater, high thermal conductivity adhesive was used on the inside surface of the heater to bond the heater to the cyclone wall. In this design, the heating flux i of the heaters differed from each other but each heater had a uniform flux.

Thermocouples (TC) and a Resistance Temperature Detector (RTD) were installed in the cyclone wall to monitor the local temperatures and another RTD was installed at the tip of the skimmer to record that temperature, Figure 37. During an experimental test, the cyclone section together with heaters and temperature detectors was covered with polyurethane foam to isolate the cyclone from the environment. A Boroscope was inserted through the cyclone wall to observe the water behavior inside the cyclone.
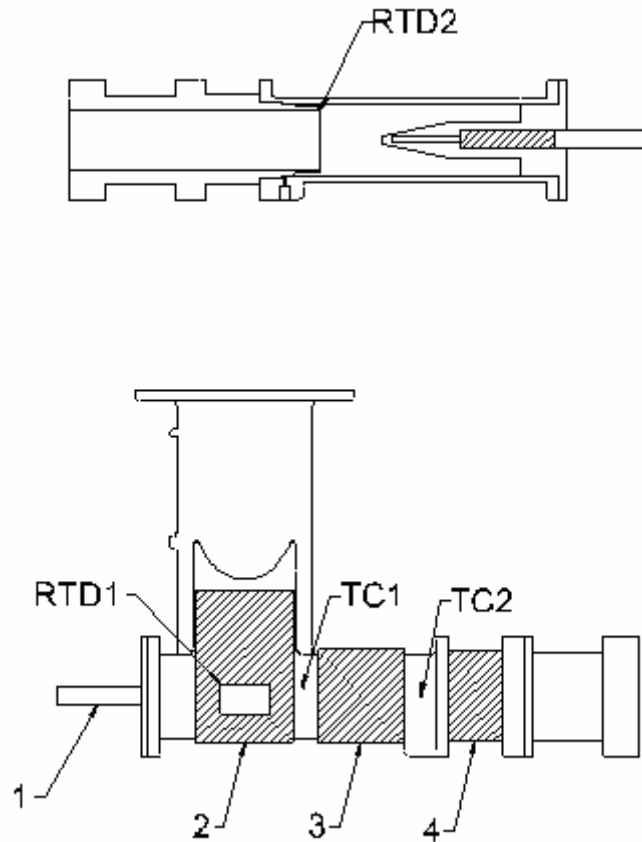
Figure 37 Heaters and temperature detectors on the bioaerosol sampling cyclone, 1~4 are heaters

A design problem was identified through the use of simulation, namely, that liquid could freeze at the leading edge of the skimmer. The skimmer, Figure 38, has a thin short nose with a length of about 12.7 mm (0.5-inches) length and a thickness of 1.143 mm (0.045-inches). A heater cannot be attached directly to the nose section, and heat can only be conducted through the thin wall of the nose to reach its tip. The whole nose section of the skimmer must be maintained above the freezing temperature of water as liquid water will be present in the skimmer region during operation. In the original

design, the whole skimmer was machined from 304 stainless steel (304SS), which has a thermal conductivity of only 15.3 W/(m·K). However, the average heat transfer coefficient for the skimmer nose is high, about 280 W/(m²·K). Simulation showed that a heater with flux of 45000 W/(m²·K) would be needed to keep the tip of the skimmer at 2°C when the air temperature is -20°C. Furthermore, the surface temperature at the tip of the skimmer (Figure 38) would need to be about 110°C, which could damage bioaerosol particles and cause excessive evaporation. These facts revealed that the skimmer needed to be re-designed.

In the new design, an aluminum alloy (AL) was used that has a thermal conductivity of about 167 W/(m·K) and the thickness of the nose was increased to be 1.4 mm (0.055-inches). Simulation predicted that the i value, the total power for the skimmer heater, and the temperature of the tip of the skimmer (Figure 38) are reduced to 24000 W/m², 85W, and 35°C, respectively, to maintain the tip of the skimmer at 2°C when air temperature at the cyclone inlet is -20°C.
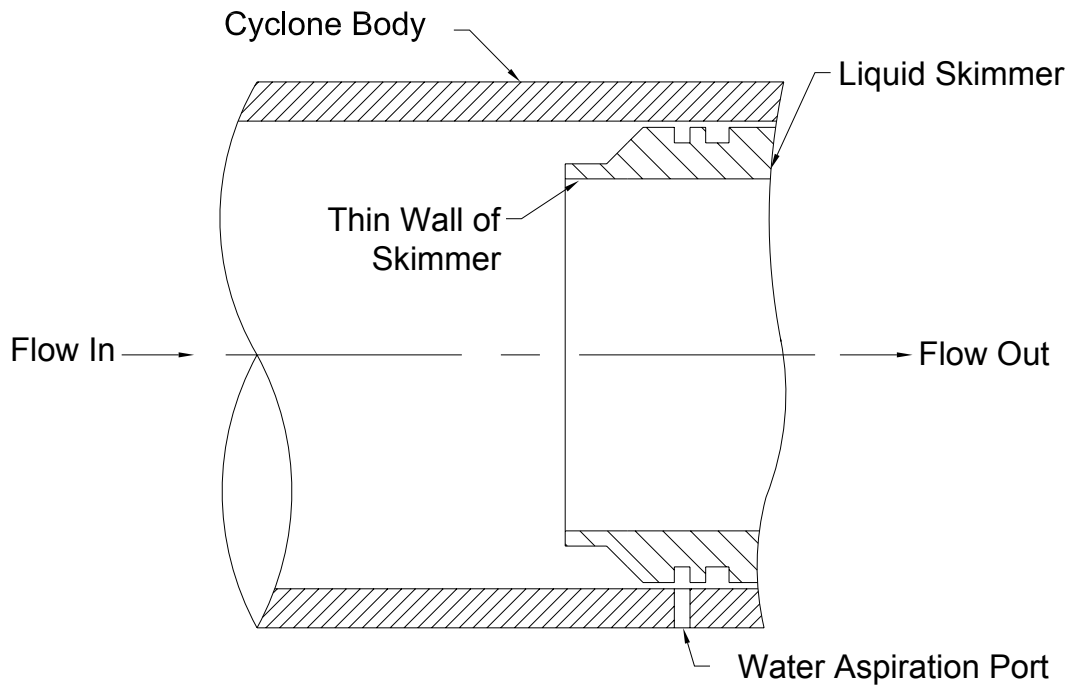
Figure 38 Structure of the skimmer nose with thin wall inserted into the cyclone body

After the heaters are wrapped on the cyclone wall, there can be some bare gaps not covered by the heaters because of the complex geometry of the cyclone and installation of temperature detectors such as thermocouples (TC) or resistance temperature detectors (RTD). The cyclone wall has a wall thickness about 3.175 mm (0.125-inches) which implies that the temperature of the cyclone wall is almost uniform in the normal direction because the normal Biot number is only about 0.052, based on a convective heat transfer coefficient of 250 $W/(m^2 \cdot K)$ and a thermal conductivity of 15.3 $W/(m \cdot K)$. However, temperature in the axial direction in a bare region can vary if the width of the region is large and if the temperature of the midpoint of the bare region, between the heaters, is low because that region could only be heated by conduction in the axial direction. Figure 39 shows the necessary minimum heat flux i of the heaters as

a function of gap width for assurance that the midpoint of a gap is above freezing. The CFD calculations are based on a simplified geometry in which a 3.175 mm (0.125-inch) plate was simulated. In the simplified plate case, 304SS was used (conductivity of 15.3 W/(m·K)) for the 3.175 mm plate. Cold air at a temperature of -20°C exchanges heat with the plate at its top surface where the average convective heat transfer coefficient was 225 W/(m^2·K). Heaters were located at the bottom surface of the plate and there was a bare gap between the heaters. The thermal conditions of the plate are similar to the cyclone wall.

It can be seen in Figure 39 that when the width of the gap increases, the minimum i increases rapidly which implies that the gap between the heaters should be maintained as small as possible. When the gap is too wide, the internal midpoint of the cyclone wall cannot be heated above freezing temperature if the intensity of the heater is not sufficiently high. This phenomenon was observed in an experimental test where an RTD was used that resulted in a bare window with dimensions of about 30.5 mm × 17.8 mm (1.2-inches × 0.7-inches) inside a heater and there was a gap about 8.9 mm (0.35-inches) between the two heaters, Figure 40. Heater flux was 12000 W/(m^2) around the RTD window for the 304SS cyclone wall and cold air was at -41°C. It can be expected that the midpoint temperature of the windows will be below the freezing temperature and water will become ice at this region according to the simulation prediction. This was observed with the Boroscope, where ice was formed near the RTD window center and at the gap between the heaters; however, there was no ice in the nearby heated regions, Figure 41.
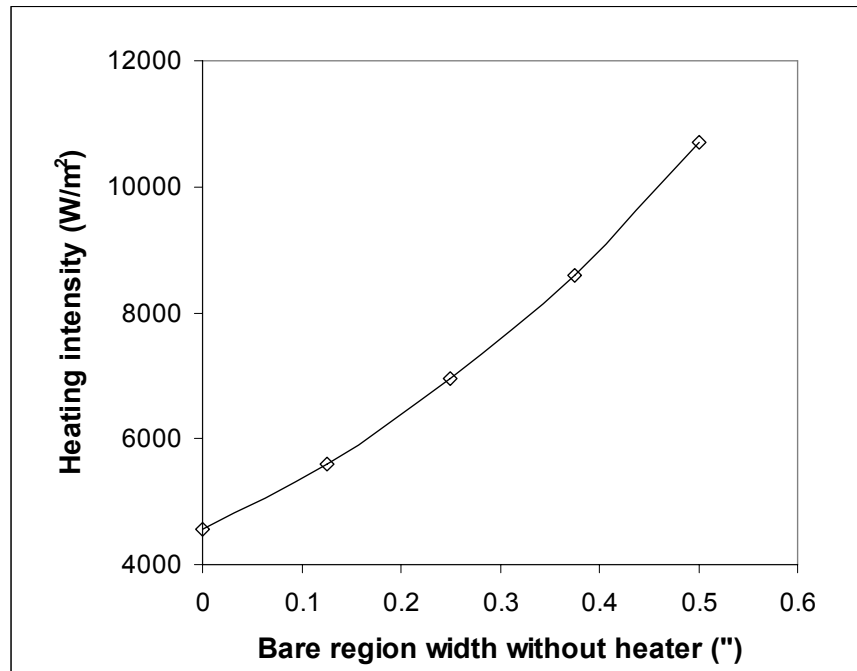
Figure 39 Minimum heating intensity i of the heaters as a function of the bare region width without heater
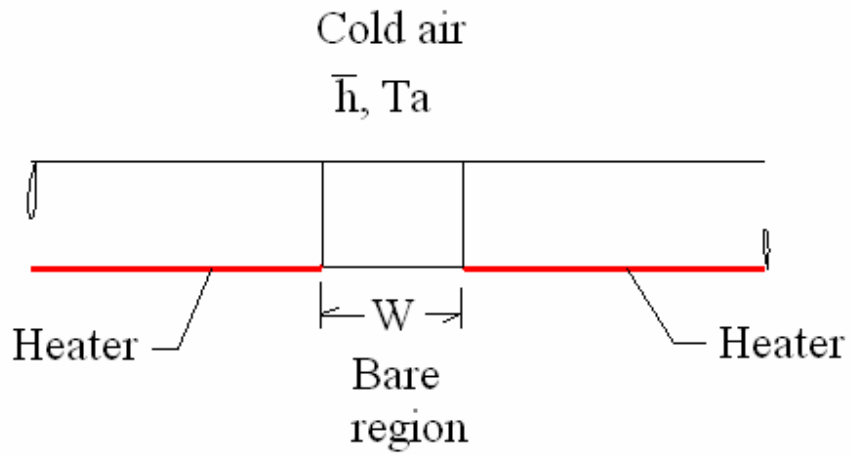
Figure 40 Schematic drawing for plate used in simulation
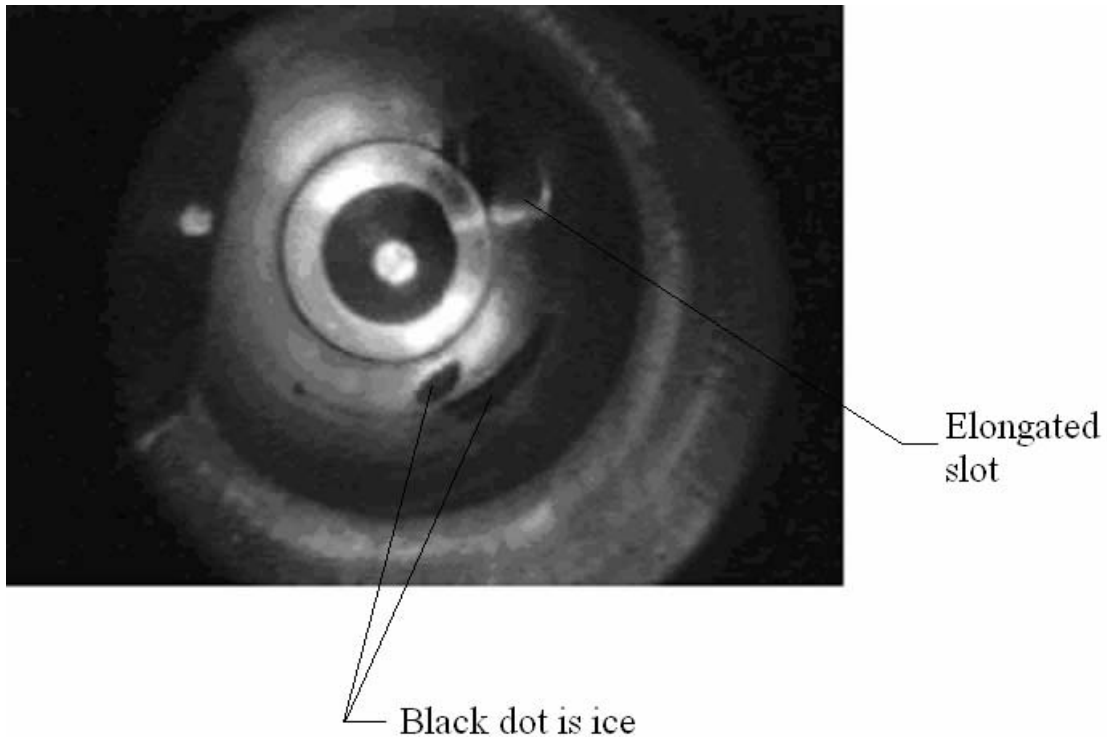
Figure 41 Photo taken in an experiment with -41°C cold air to show ice formation near the bare region without heaters

The heaters were re-designed to reduce the width of the gaps between the heaters and the SS304 skimmer was replaced with an AL skimmer. Experiments were conducted to test the performance of the modified cyclone operated at cold temperatures with a total heater power of about 320W. In one test, the air blower was operated for 9 minutes to allow the cyclone wall to cool to a uniform temperature of -10°C before the heaters were actuated. The temperature of the 304SS skimmer was recorded via the RTD to compare its temperature response with the CFD prediction, Figure 42. Good agreement was obtained between the experimental measurements and simulation, with the maximum difference being about 3°C in the transient period. Simulation predictions are

a little higher than measurement results because the heater was not perfectly isolated in the test so some heat may have been lost to the environment. For the 304SS skimmer, the tip temperature increased from -10°C to 4.2°C, a 14ºC increase, in about 4 minutes. In contrast for a test with the AL skimmer under the same conditions, the tip temperature increase was about 24°C, which indicates that the AL skimmer can achieve much better thermal operation performance in colder temperatures than the 304SS skimmer. Also the AL skimmer will require much less power than the 304SS skimmer to achieve comparable performance.
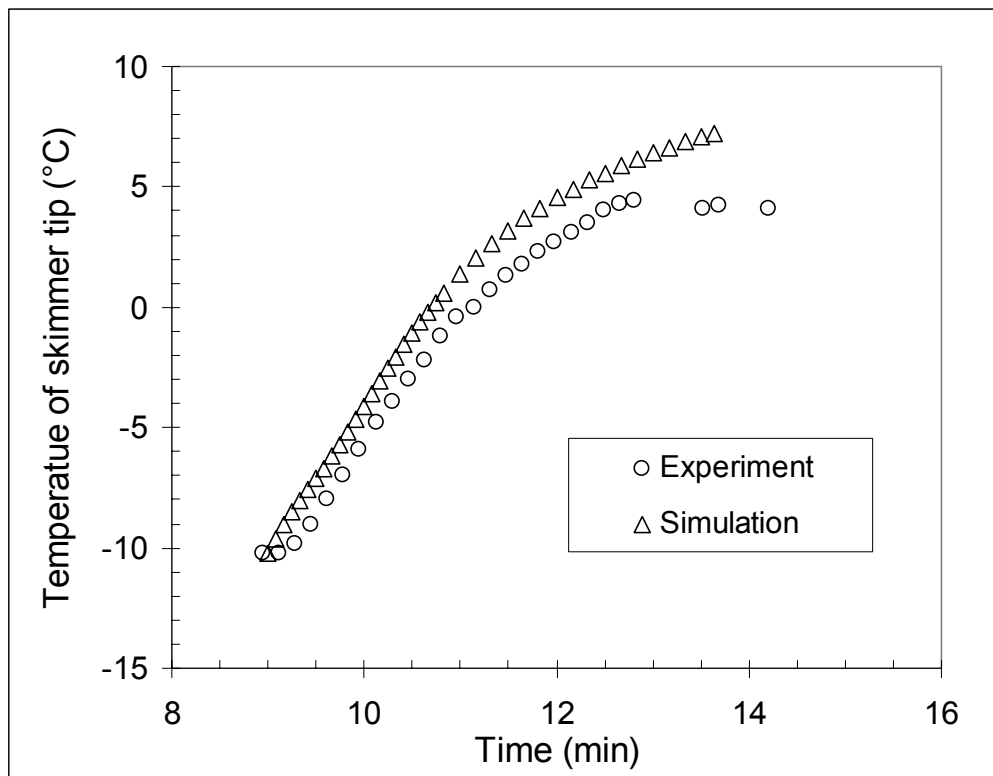
Figure 42 Temperature response of the tip of the 304SS skimmer. Comparison between experiment and simulation

In a second test, with the cyclone at room temperature (20°C), the heaters and blower were turned on at the same time so -41°C cold air and heating energy acted on the cyclone simultaneously. Temperatures at several local points were recorded to study the time response of the cyclone to the cold air and to compare observations with the CFD predictions. Figure 43 shows the measured and predicted temperature for points TC1 and TC2 (Figure 37), where it can be seen that good agreement was obtained between experimental and numerical results. Points TC1 and TC2 are located on the cyclone body but the temperature of point TC1 decreases much faster than point TC2, which means that the turbulent heat transfer coefficient at point TC1 is much higher than TC2. It is also noticeable in Figure 43 that the temperature response of the cyclone wall to the cold air is very fast as the temperature at point TC1 decreases from the initial 20°C to below 0°C in about 40 seconds. This suggests that convective heat transfer is dominant and that the stored energy of the cyclone body may only maintain above-freezing temperatures for a short time. In turn, this also suggests that the heaters must be turned on at the same time as the blower.
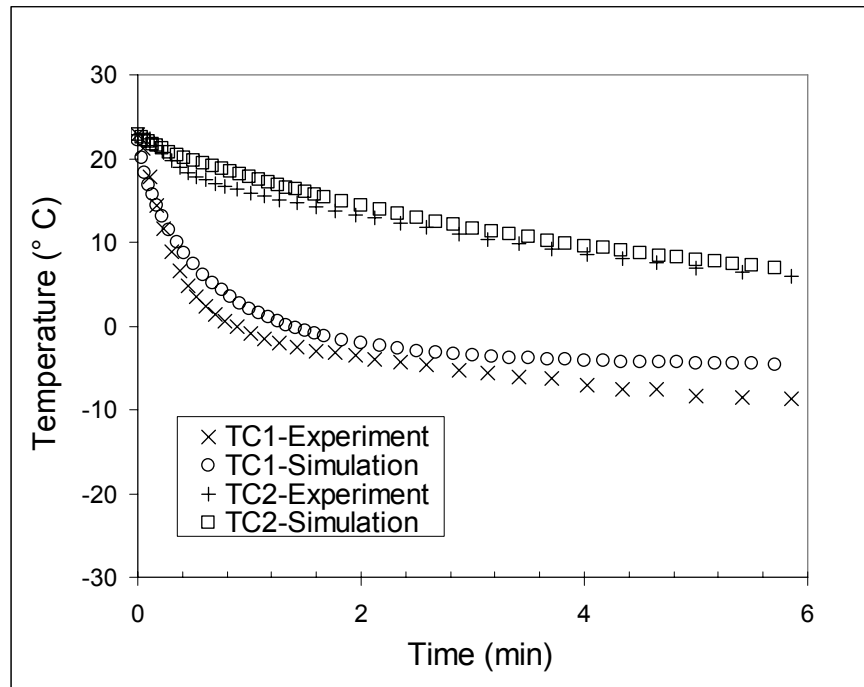
Figure 43 Temperature responses of points using thermocouples TC1 and TC2 on the cyclone body, comparison between experiment and simulation

Cyclone CYC-A, which was designed for a flow rate of 780 L/min, has heaters that only apply heat to the wall of the cyclone, i.e., no heat is provided to either the vortex finder or the skimmer, and the skimmer material is 304SS. Due to ice buildup near the vortex finder, this cyclone could not function when the cold air temperature was -10°C. In the present study, where the cyclone sampling flow rate is 1250 L/min, the improved heater designs allow operation at temperatures as low as -26°C, yet the heaters use less power. Table 3 gives the comparison of the two applications, where it can be seen that the cyclone with the new heater design significantly improves low temperature performance.

Table 3. Comparison of heater design for the CYC-A and CYC-B cyclones

	Q (L/min)	Surface area (m^2)	Total power of heaters (W)	Coldest working temperature (^{o}C)
CYC-A	780	0.030	350	> -10
CYC-B	1250	0.055	320	About -26

4.4 CYC-C: Double Outlet Axial Exhaust Cyclone

Pressure drop across a cyclone is important because it provides an indication of the ideal power consumption of the cyclone. A traditional cyclone has one inlet and one outlet. Pressure coefficient K value can be used to indicate pressure drop behavior through a device, where K is defined as

$$K = \frac{\Delta P}{\frac{1}{2}\rho U^2} \tag{65}$$

Here, ΔP is the pressure drop across the cyclone and U is the averaged air velocity across the entrance slot. The value of K for a single outlet cyclone is generally about 3~4. Equation (65) may also be considered as showing that the pressure drop of a cyclone is proportional to the square of the averaged air flow velocity. When air flow velocity decreases, the pressure drop can be reduced significantly assuming a similar pressure coefficient. If the air flow separates into two streams after it is taken into the cyclone body, the averaged air velocity in the two streams should be reduced because each stream has only half of the total mass flow rate. Each stream of the air flow exhausts through one outlet so the cyclone would have two outlets. At the same time, the

cutpoint of the two outlet cyclone should be similar to the one outlet unit because they have similar averaged air velocity upstream of the entrance slot. As discussed earlier, for the cyclone configurations, such as CYC-B, the majority of the particle deposition happens near the first turn downstream of the projected area of the entrance slot and the deposition is determined by the particle Stokes number, i.e., the averaged air velocity and the slot width. If a double-outlet cyclone has the exact same geometry upstream of the entrance slot as the one-outlet cyclone, the two units should have the same particle deposition performance.

A double-outlet cyclone was designed and simulated to check its pressure drop. The double-outlet cyclone, named CYC-C, uses the same cyclone inlet section as the CYC-B unit upstream of the entrance slot with a flow rate of 1250 L/min to obtain a 1 μm AD cutpoint. The cyclone inlet connects to the cyclone body, which connects to the skimmer in sequence. In CYC-C the air flow separates into two streams and is exhausted from two outlets, as shown in Figure 44.
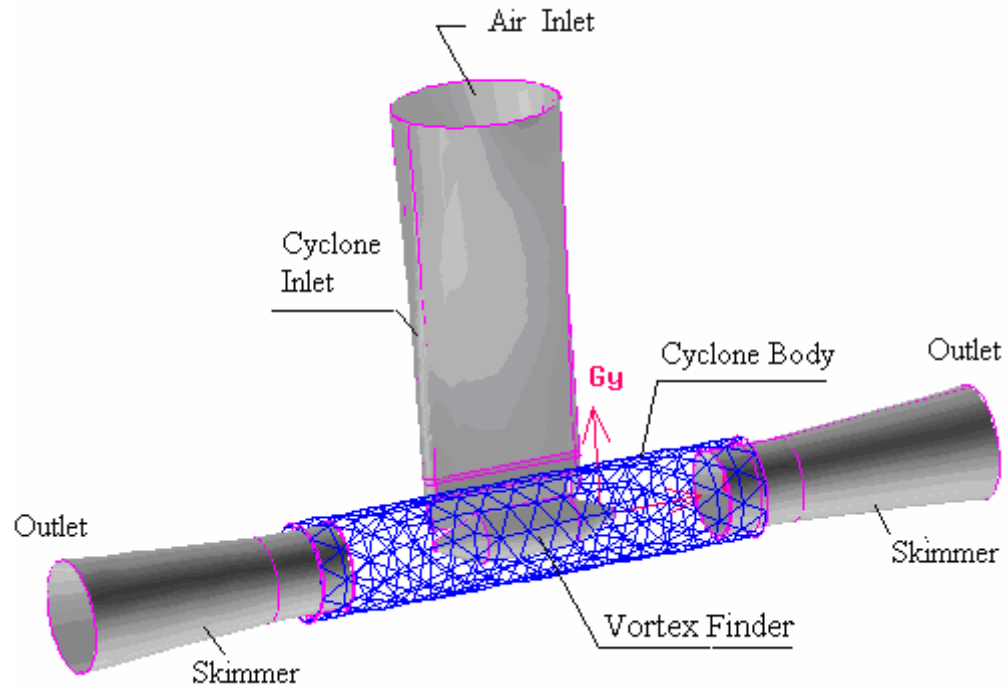
Figure 44 Layout of CYC-C with double-outlets

The vortex finder in CYC-C is fixed with two small bolts through the cyclone body. Dimensions of the CYC-C cyclone at the cyclone inlet, entrance slot, diameter of vortex finder, diameter of cyclone body, and skimmer are all the same as those of the CYC-B unit. The experimental setup used to check the airflow characteristic (pressure drop as a function of flow rate) is shown in Figure 45, where the flows from the two outlets of the CYC-C cyclone are joined together and exhausted through the same blower.
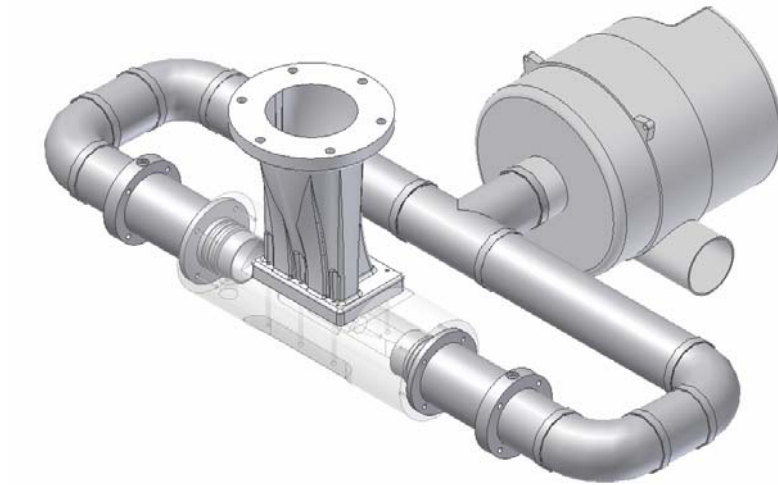
Figure 45 Double-outlet cyclone experimental set-up

The CYC-B and CYC-C cyclones were tested to compare the pressure drop across the cyclones at different flow rates. The results are shown in the Figure 46. During the experiments, one cyclone inlet was used to ensure the same pressure drop caused by the inlet section so the measured pressure drop can indicate the difference of the pressure drop caused by the cyclone body. At a flow rate of 1250 L/min, the pressure drop of the double - outlet cyclone is about 25% less than the single-outlet unit.
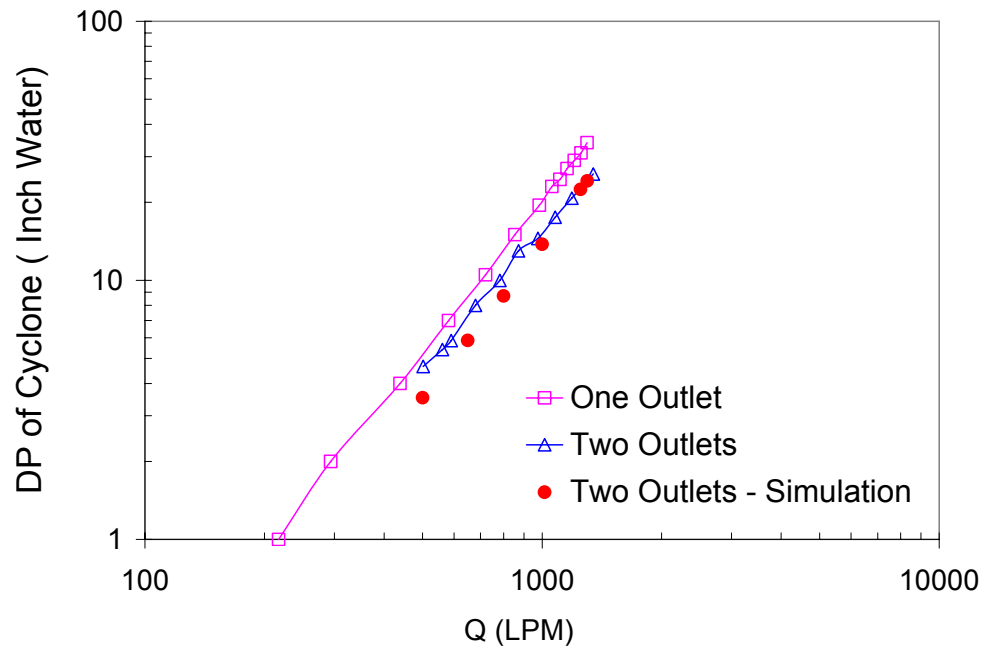
Figure 46 Comparison of pressure drops in single and double outlet cyclones

4.5 CYC-D: Scaled 100 L/min Cyclone

A 100 L/min cyclone, named CYC-D, was designed based on Stokes scaling from the CYC-B cyclone. The two cyclones are intended to have the same cutpoint. As described earlier, $Stk_{0.5}$ is about 0.05 for the CYC-B cyclone and this value is used to calculate the dimensions of the CYC-D, considering the Reynolds number effect. Some studies (Moore and McFarland 1990, Zhu and Lee 1999) reported that the trend of $Stk_{0.5}$ of a cyclone is increasing as the flow Reynolds number decreases especially in the low Reynolds number range, less than 4,000-6,000, the $Stk_{0.5}$ increases significantly. Reynolds numbers of the 1250 L/min CYC-B cyclone and the 100 L/min CYC-D unit are about 28,000 and 5,000, respectively, which means that the $Stk_{0.5}$ of CYC-D could be larger than 0.05 of the CYC-B unit. Referring to their suggested results, a value of 0.07-0.08 for $Stk_{0.5}$ is selected in the design of the CYC-D cyclone with a flow rate of 100 L/min and a flow Reynolds number of about 5,000.

Low pressure drop is an important objective for this design. It is found that the skimmer I.D. is a critical factor in determining the pressure drop of the cyclone. For a fixed cyclone body and inlet section, when the I.D. of the skimmer decreases, the pressure drop increases significantly because of the higher velocity of the swirling air. When the magnitude of the swirling velocity increases, it will also cause the air to turn faster and results in a longer pathline of the air. The skimmer I.D. $D_{Skimmer}$ should be large but it is limited by the cyclone body I.D., $D_{Cyclone}$, the thickness of the skimmer nose, δ_{Nose}, and the gap, δ_{Gap}, which is necessary to allow passage of the liquid. Generally, $D_{Cyclone}$ is fixed based on the flow rate and cutpoint requirement, and δ_{Nose} is determined by the fabrication process. Figure 47 shows the pressure coefficient for the cyclone with different skimmer I.D. It can be seen that the pressure drop is nearly linear to the skimmer I.D in a range of 0.45-0.60" for this cyclone.

$$D_{Cyclone} = D_{Skimmer} + \delta_{Nose} + \delta_{Gap} \qquad (66)$$

$$K \approx 11.2 - 14 D_{Skimmer} \qquad (67)$$

When CYC-D is operated at the flow rate of 100 L/min, the averaged air velocity at the entrance slot is about 25 m/s, which is lower than that in the CYC-A unit, 47 m/s. This implies that the CYC-D has a thicker boundary layer than the CYC-B. The water is injected into the cyclone at a flow rate of about 0.3 mL/min. If water is injected into the cyclone through a similar hole like in the CYC-A, the liquid jet may not reach the high velocity region and just scroll down along the cyclone wall. Air-blaster needles are used for water injection in the CYC-D to atomize the water into small droplets. Based on these considerations, a cyclone was designed with a cyclone body diameter of about 17.45 mm (0.687-inches) as shown in Figure 48.
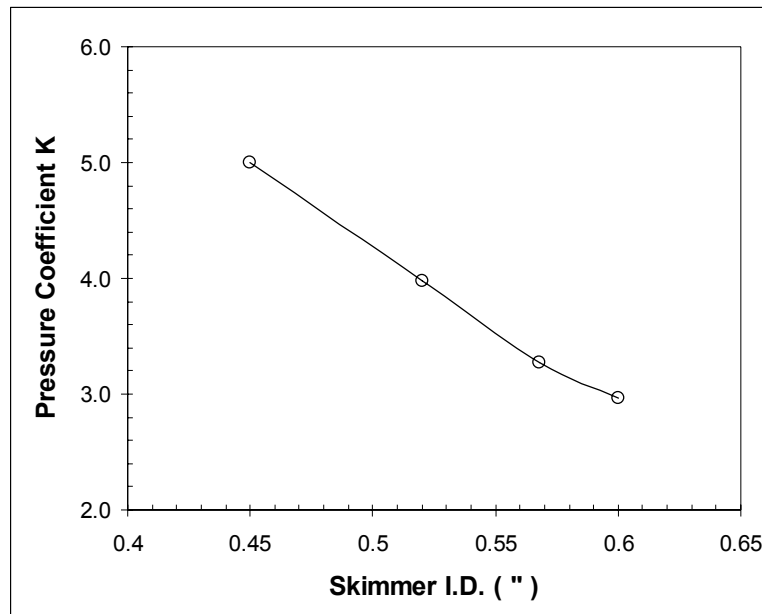

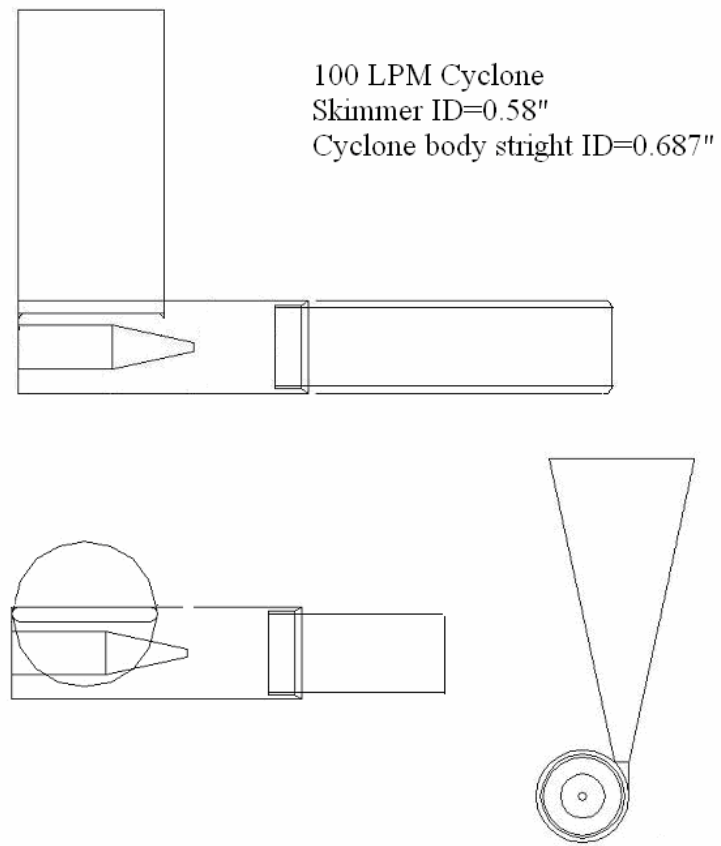Figure 47 Pressure drop coefficient K as a function of the I.D. of the skimmer

100 LPM Cyclone
Skimmer ID=0.58"
Cyclone body stright ID=0.687"

Figure 48 Schematic drawing of CYC-D

4.6 Summary

Numerical simulation is used to predict performance and to analyze flow structure and the liquid film developed in bioaerosol sampling cyclones that have axial flows of the exhaust air. The CFD program FLUENT, using RSM, DPM, and heat transfer models with suitable discretization schemes, was found to properly predict particle collection, pressure drop, and temperature responses for the cyclones that operate in a flow Reynolds range of 16,000~32,000, and a particle Stokes number range of 0.008 to 0.5.

The flow inside the cyclone has a special structure that provides a cutpoint Stokes number of about 0.05. At the design operating conditions of the upgraded cyclone, CYC-B, (1250 L/min intake of air and 1 mL exhaust of liquid), the cutpoint particle size, $D_{0.5}$, is approximately 1 μm AD. The principle of operation for particle deposition could be considered as similar to that of a classical inertial impactor, where deposition occurs in a small area of the internal wall as a consequence of the stopping distance effect; however, here the cutpoint Stokes number is smaller than that of a classical slot impactor. The stopping distance model for the principle of operation contrasts with that of Lapple (1951) for a reverse flow cyclone, where Lapple assumed the flow enters the cyclone at the inlet velocity and undergoes several turns (typically about 6) before reversing direction towards the outlet tube, with the particles being driven to the wall by the centrifugal force during the several turns. In this cyclone, as the flow enters the cyclone body it accelerates and narrows due to the interaction with the internal spiral layers. This causes an increase in the particle velocity and a subsequent

reduction in the distance particles must travel to reach the wall, and the combination of these two factors enhances particle deposition. But, as the flow travels in the axial direction, it is forced inward, which increases the distance particles must travel to reach the wall, resulting in the phenomenon where most of the deposition occurs in the region near the rectangular entrance slot.

A shell-volume method was developed to analyze causes for the formation of a rotating water ring and liquid carryover into the exiting air stream, observed on the earlier version of the sampling cyclone CYC-A. This special method was a 3D simulation, using the VOF model that is practical for analyzing the thin liquid film in a device with complex geometry and of a large size. Understanding obtained from the simulations was used as a guide to develop modification that led to an upgraded cyclone, CYC-B. Experimental evaluation of the upgraded cyclone indicated elimination of a ring of water that was situated just upstream of the liquid skimmer in CYC-A, and the corresponding resolution of a liquid carryover problem.

Numerical simulation was used to predict the turbulent heat transfer coefficients and to design heaters for the CYC-B cyclone that would prevent injected liquid from freezing at air temperatures as low as -26ºC. The FLUENT CFD program was used to successfully design a new skimmer for the cyclone which significantly reduced the necessary power to operate in cold air. The time response and temperature of the cyclone wall were studied at different operational conditions. Numerical predictions were compared with experimental results and good agreement was obtained. These suggest that CFD can be a useful tool for design of bioaerosol sampling cyclones. Theoretical

analysis was used to calculate the mean size of the atomized water particles and their temperature response in the cold turbulent air flow based on empirical models and equations. Transit times and cooling times for different particle sizes were calculated and it was concluded that the atomized 42 µm water droplets will not freeze during the transit time, which was verified in the experiment.

A double-outlet cyclone CYC-C was designed and tested and its pressure drop was about 25% lower than the traditional single-outlet unit. This type of cyclone could be used in the field where lower power is required.

CHAPTER V

CIRCUMFERENTIAL SLOT VIRTUAL IMPACTOR

5.1 Introduction

The circumferential slot virtual impactor (CSVI) is designed to concentrate particles based on the principle of particle inertia. A CSVI can operate with a very low pressure drop which is important for field operation, and it can avoid a side effect that generally occurs in linear slot virtual impactors (LSVI) where particles are lost on the side walls of the receiver section. Many experimental and numerical studies have been reported on virtual impactors (VI) in the past few years regarding their performance and flow stability. However, only a few studies have focused on CSVIs. Haglund and McFarland (2004) reported on a CSVI unit with 150.32 mm (5.918") slot diameter and 0.5 mm (0.0197") slot width. When the unit was operated at 122 L/min, its jet velocity was about 8.63 m/s, the pressure drop was only 63 Pa, and cutpoint was about 2.2 μm. The minor flow fraction efficiency was higher than 72% for particles in the size range of 4.4~10 μm AD.

Loo and Cork (1988) identified the relevant parameters of virtual impactors and analyzed the qualitative sensitivity of a set of detailed parameters on the performance. Validated by comparisons with experimental results, Marple and Chien (1980) used numerical calculation and provided both qualitative and quantitative sensitivity of some factors such as nozzle Reynolds number, nozzle throat width, and collection probe size, etc. on the fractional efficiency and wall loss of the virtual impactor. Hari et al. (2006) used numerical techniques to study the performance sensitivity of a slot virtual impactor

to find an optimization configuration of the geometrical parameters such as throat length and radius of curvature in the receiving nozzle etc.

A special feature of VIs is that the inside flow may be unstable, which can cause the fractional efficiency to be far less than the expected value (Haglund and McFarland, 2004). Han and Moss (1997) visualized the streamlines within a water virtual impactor and found that the flow was stable in a Reynolds number range 2,000~7,000 under certain operational conditions. An interesting feature in their experiment was that the flow tended to be unstable when Re is less than 2,000, especially when it was less than 1,000, which suggested that when the jet is slower, the flow can be more unstable. Gotoh and Masuda (2000, 2001) reported an unstable three-dimensional flow structure in their experiment for rectangular and annual jet virtual impactors and showed some photographs to describe the unstable flow patterns in the minor region. They focused on the reason for instability to be an adverse pressure gradient and added some blocks into the minor region to accelerate the flow and correspondingly to decrease the downstream pressure. The impactor performance was improved by these modifications but detailed reasons for the cause of the unstable flow, were not given. The factors that cause the instability have not been clearly understood or presented at the present time.

In this study, numerical simulation was used to design and predict the performance of CSVI units with flow rates of 10 L/min and 100 L/min over a range of sizes from 1 to 15 μm AD. The CSVI is required to have a wide dynamic range of collection, which means it should have high collection efficiency in the minor region of the unit for the particles in a wide size rage about 1-15 μm.

For the 10 L/min unit, named CSVI-10, CFD was used to modify the unit geometry to improve its dynamic range and predict performance. The predicted fraction efficiency and pressure drop for this unit were compared with the experimental results to validate the CFD results.

In the experimental test for an earlier version of 100 L/min unit, named CSVI-100A, a pulsing noise could be clearly heard and the fraction efficiency in the minor region for large particles was significantly lower than expected. Simulation was used to find possible reasons and solutions for this instability problem. In an upgraded unit, CSVI-100B, in which flow was stable and fraction efficiency was significantly improved, unusual deposition (about 25% loss) was found in the experiment which was caused by the posts which support and align the two halves of the CSVI unit. CFD was used to calculate the flow field and analyze the effects of the posts on the particle deposition. A new unit, CSVI-100C with improved posts was fabricated and tested and the experimental results showed good performance together with excellent agreement with numerical predictions.

5.2 CSVI Description and Performance Features

The typical CSVI geometry studied herein, which is axisymmetric, is shown in a cross-section in Figure 49. From the viewpoint of the fluid, the air flow accelerates in the inlet acceleration nozzle and impinges into the receiver nozzle. About 90% of the mass flow makes a turn and gets into the major flow region and the remaining 10% of the air mass flow rate is exhausted through the minor flow region.
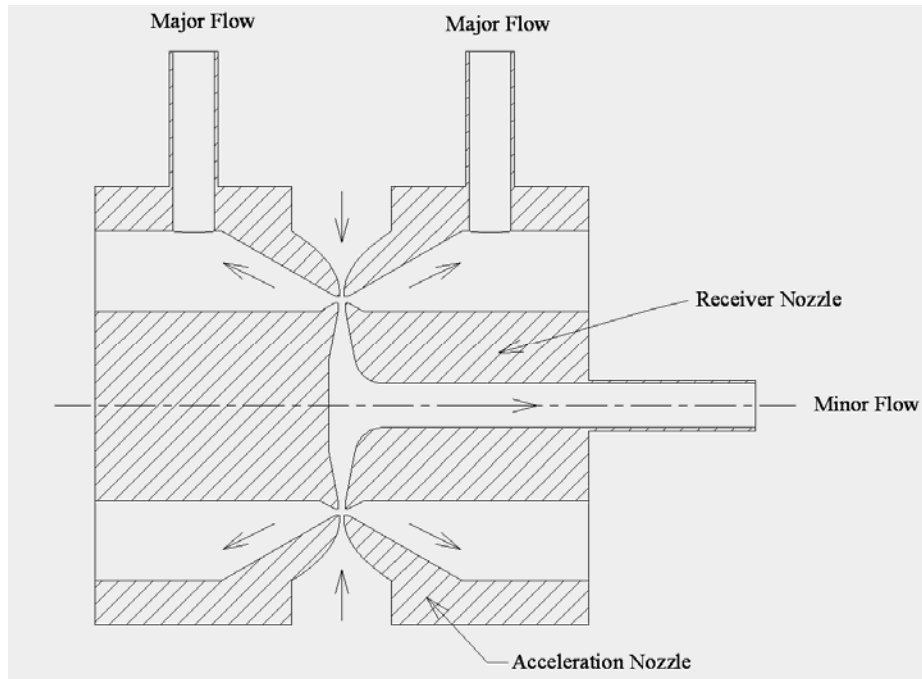
Figure 49 Side cross-section view of CSVI unit

With reference to Figure 50, the geometric parameters of the CSVI that affect its performance are:

- W_1: Slot width between acceleration nozzles which affects the average air velocity, flow Reynolds number and particle Stokes number. Generally the slot width is about 0.508 mm (0.020"), with smaller values resulting in faster jets.

- W_2: Slot width between receiver nozzles which determines the expansion of the minor flow. Larger W_2 value implies larger expansion ratio for the minor flow. This width is generally larger than W_1, and a smaller width between

receiver nozzles could result in more particle loss. Typically for a CSVI, W_2 is about $1.625 W_1$.

- H : Distance between the acceleration nozzles and the receiver nozzles.

- R_C : Critical zone radius, which is defined as the distance from the center of the separation area to the axis of the unit. When the flow rate is fixed, the critical zone radius, together with the W_1, determines the jet velocity. Larger values of R_C corresponds to lower jet velocities.

- R_O : Radius of exhaust tube from minor flow region which determines the air velocity inside the exhaust tube and in sequence, the static pressure. Smaller values of R_O result in a higher air velocity in the exhaust tube and a lower pressure field, but, may cause a problem in the interface with an outside connection. Misalignment could cause inward facing steps in the exhaust tube flow and could result in losses of larger particles.

- R_i : Fillet radius of the receiver nozzle in the receiver section along which the major flow makes a turn. This fillet radius determines the curvature of the pathlines of the major flow and affects the particle wall losses. During the turn of the major flow, the interaction force between the flow and the receiver at this fillet may also affect the stability of the flow. Typically it is about $0.25 W_1$.

- θ_1 : Expansion angle in the major flow region, which determines the volume of the major flow region. The typical value for this angle is about 30°.

- θ_2: Expansion angle in the minor flow region and it determines the expansion rate of the minor flow. A larger angle provides a larger volume for the minor flow to develop and expand, and could possibly reduce wall losses. However, as shown later, it may result in a problem of flow instability.

- *L*: The width of the air pathway in the expansion section of the minor flow region. When the expansion angle θ_2 is large, this width increases rapidly and can result in an adverse pressure gradient.

- *L1*: Distance to the center of the critical zone along with the minor flow direction towards the axis.
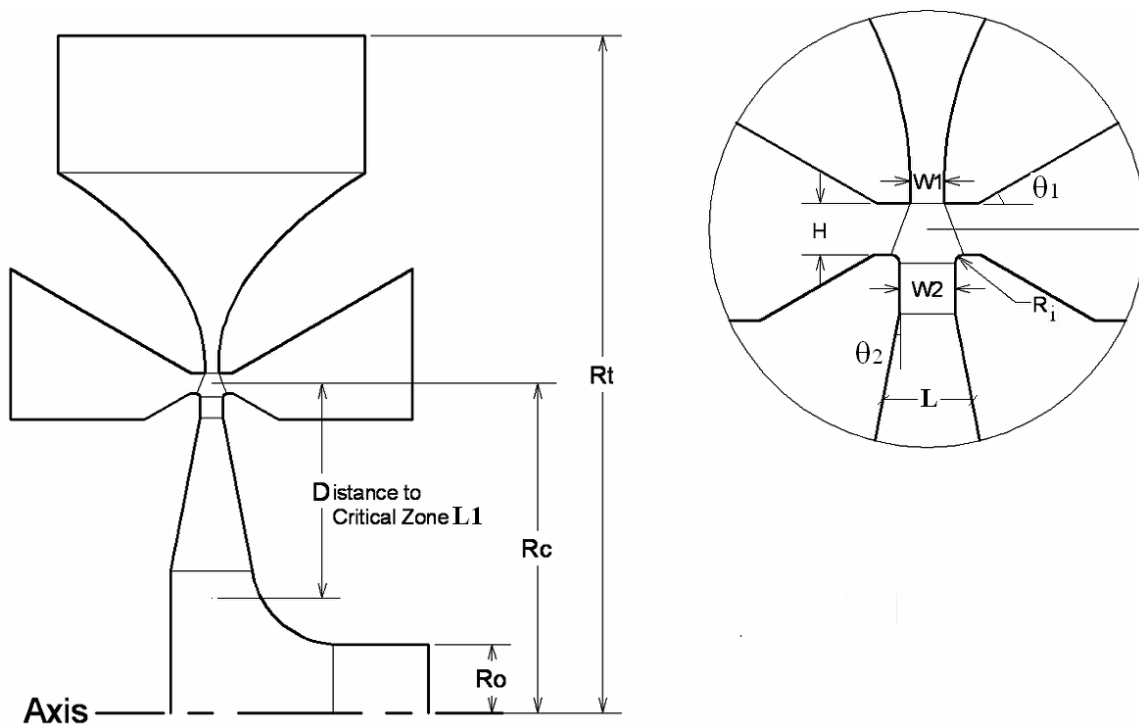

Figure 50 Side cross-section view of CSVI unit including dimensions

After the jet from the acceleration nozzle impinges into the receiver nozzle the minor flow (typically 10% of the sampled mass flow rate) will expand rapidly and the average velocity will decrease quickly. As the minor flow approaches the axis, it expands and has a larger width L as the radius R decreases, so the average air velocity will depend on the combination of these two dimensions. The flow Reynolds number is determined by the average velocity at the slot and it is in a laminar flow range for conditions used in this study. The particle Stokes number is determined by the jet velocity at slot and the width of the slot. When the flow rate is fixed, the slot width determines both the flow Reynolds number and the particle Stokes number.

$$U = \frac{\dot{Q}}{2\pi RL} \tag{68}$$

$$\mathrm{Re} = \frac{UW_1}{\rho_a \mu} \tag{69}$$

$$Stk = \frac{C_C \rho_P D_P^2 U}{9\mu W_1} \tag{70}$$

The slot width W_1 of the acceleration nozzle is used to calculate the particle Stokes number.

A study of optimum CSVI designs should consider the effect of these dimensions on the flow stability, wall loss, and upstream and downstream connection problems, etc. Most dimensions have different effects on flow stability and wall loss and the total effect is a coupling of the effects of all these dimensions. So, a set of optimum values for these dimensions must be selected considering the total coupling effects.

The ideal flow inside a CSVI should be stable, and uniformly travel towards the axis with no circumferential-direction velocity component. Considering boundary layer effects, the maximum velocity in the entire CSVI should be about 1.2 times the average velocity at the slot. If the CSVI flow is unstable, it may not flow toward the axis direction and could have a circumferential velocity component that results in a 3D flow, which may cause the maximum velocity inside the CSVI to increase to about 2-2.5 times the average velocity at the slot. In case of unstable flow, particle behavior is unpredictable, and the minor flow fractional efficiency is expected to be low. Stable flow is thus one of the important objectives in CSVI design.

Low wall loss is another important objective in the CSVI design. When the total flow splits after the critical zone, for the particles with sizes near the cutpoint, 50% should be discharged with the major flow and the other 50% should follow the minor flow. However, when the particles follow the major flow and make a turn, they could impact onto the wall and thereby contribute to wall loss. Generally, this takes place at the fillet corner of the receiver nozzle, which has a small typical radius of about $0.25W_1$. This transitional radius of the fillet is found to be important for the wall losses and the flow stability.

Low pressure drop across the CSVI is also important in the design because the pressure drop determines the ideal power consumption during operation. Small pressure drop is one of the special benefits of a CSVI. A goal of the CSVI development program is that for field operation, the CSVI devices could be battery operated, which implies the pressure loss would be less than about 2.5 kPa (10 inches of water).

5.3 Results and Discussion

5.3.1 10 L/min CSVI Unit, CSVI-10

The CSVI 10 series units have a design total flow rate of 10 L/min and a minor flow rate of 1 L/min, which results in an ideal aerosol concentration of 10X. The nominal cutpoint of the CSVI-10 unit is 2 μm, but based on Stokes scaling, it could be 1 μm if the unit were operated at flow rate of 40 L/min. There are two CSVI-10 units in this study which are named CSVI-10A and CSVI-10B. The latter one was developed to extend the dynamic range for particle collection in the minor flow region.

The general layout of CSVI-10A is shown in Figure 51. This unit has a slot width W_1 0.508 mm (0.020") and a small critical zone radius of about 3.81 mm (0.15"). The exhaust tube radius in the minor flow region is 1.42 mm (0.056"). Corresponding to a flow rate of 10 L/min, the jet velocity at the slot is 13.7 m/s and has a Reynolds number of 460. When the unit is operated at typical flow ratios, i.e., the minor flow rate is 1 L/min and major flow is 4.5 L/min through each port, simulation shows a stable flow inside this unit, Figure 52. The simulated flow field shows a uniform velocity distribution along the circumferential direction and there is no 3D flow, i.e. the velocity vector along the circumferential direction is zero. The air pathline, from a line at the inlet, shows that the air just flows towards the axis after the critical zone and goes out through minor exhaust tube.
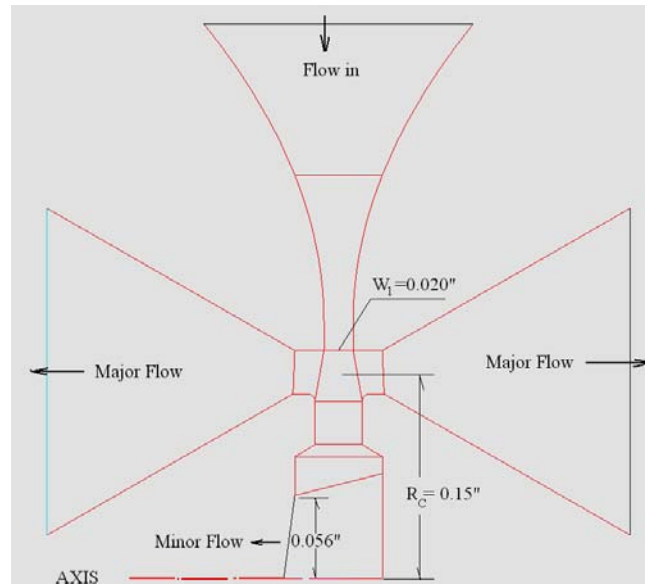
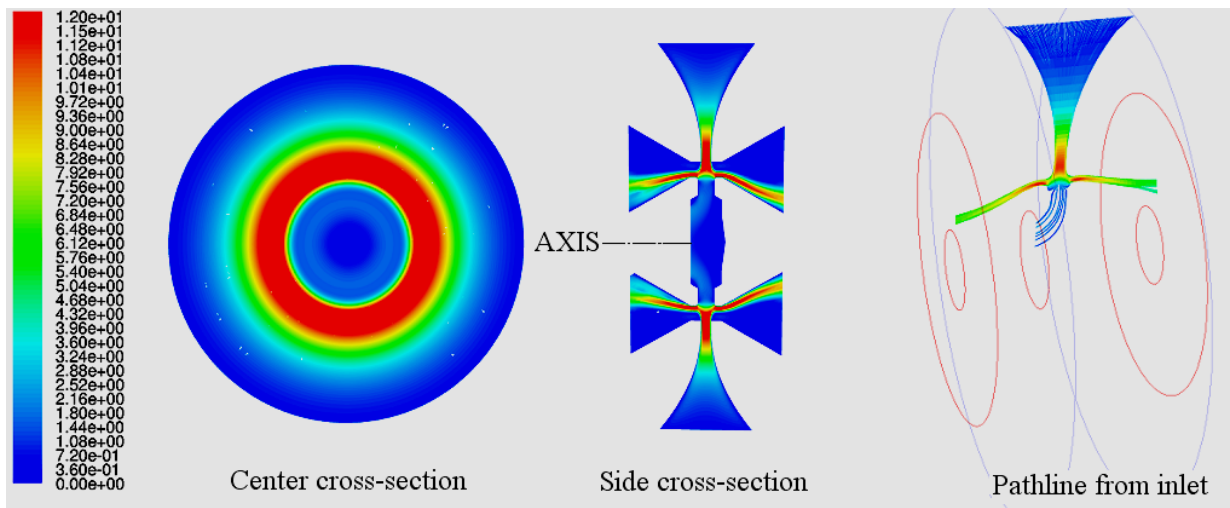Figure 51 Cross-section of CSVI-10A unit

Figure 52 Flow field in CSVI-10A unit

However, due to the small critical zone radius and minor exhaust tube size, the dynamic range is not wide as required. The stopping distance for 15 μm particles with initial velocity of 15 m/s is about 7.62 mm (0.30") which means that it needs about 7.62

mm (0.30") of distance in the space to allow the particles to decelerate and to make a turn to follow the main air flow.

$$S = V_O \tau = \frac{C_C \rho_P D_P^2 V_O}{18\mu} \tag{71}$$

The CSVI-10A unit has an exhaust tube diameter about 2.85 mm (0.112") from the minor flow region where the minor flow was taken out. The air velocity from the critical zone was high (about 14.6 m/s) so the stopping distance for 15 μm particles is about 7.62 mm (0.30"), which is much larger than the available deceleration distance inside the minor flow region. Large particles could be deposited on the opponent side wall of the exhaust tube. This is an opposite-side trajectory that is similar to the crossing trajectories caused by too large of initial velocities in small dimension devices. To reduce the wall loss potential, the minor region of the CSVI-10A unit needed to be re-designed.

The CSVI-10A unit was re-designed using Stokes scaling technology to enlarge the radius of the critical zone and the exhaust tube. However, when the critical zone radius is enlarged, the flow can become unstable. Indeed, simulation shows that when the critical zone radius reaches 8.382 mm (0.33"), the flow starts to become unstable. Thus, the critical zone radius was selected to be 7.62 mm (0.30") in the design for CSVI-10B. The unit is shown in Figure 53 which is a photograph of the external appearance of the unit.

0.3"

Figure 53 A photo of the CSVI-10B unit

$$Stk = \frac{C_C \rho_P D_P^2 U}{9 \mu W_1} = \frac{C_C \rho_P D_P^2}{9 \mu W_1} * \frac{\dot{Q}}{2 \pi R_C W_1} = \frac{Const}{R_C W_1^2} \tag{72}$$

The cross-section of the CSVI-10B unit is shown in Figure 54. Its acceleration nozzle has the same shape as that of the CSVI-10A unit and other configurations are also the same. With the 7.62 mm (0.30") critical zone radius, the averaged air velocity at the critical zone is about 9.8 m/s and the slot width is 0.3556 mm (0.014").
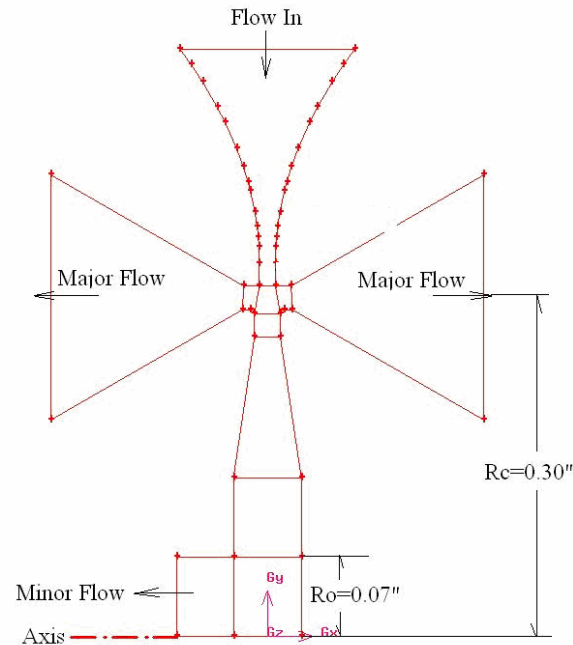
Figure 54 Cross-section with dimensions for CSVI-10B

A CSVI-10B unit was fabricated and tested and the results showed excellent fraction efficiency and robust performance (stability at different flow rates). The CSVI-10B unit has a wide dynamics range of about 100X and can operate at flow rates up to 40 L/min. Experimental results and numerical predictions are shown in Figure 55, where the excellent agreement with the experimental results exists at the four different flow rates from 10 to 40 L/min. All the tests were operated with a minor flow fraction of 10%. The numerical simulations can provide accurate predictions for all the different trends of minor fraction efficiency including the parts of the curve where the efficiency is increasing, constant, or dropping. The increasing region is a typical collection curve for inertial impaction where the efficiency increases as the Stokes number increases. The constant region is where the collection is maintained at a high value for the particles

having sufficient inertial, and the dropping portion of the curve is associated with internal wall losses of large particles. All the fraction efficiency points fit well into one curve which implies that the particle fraction performance is mainly determined by the particle Stokes number and is almost independent of the flow Reynolds number.
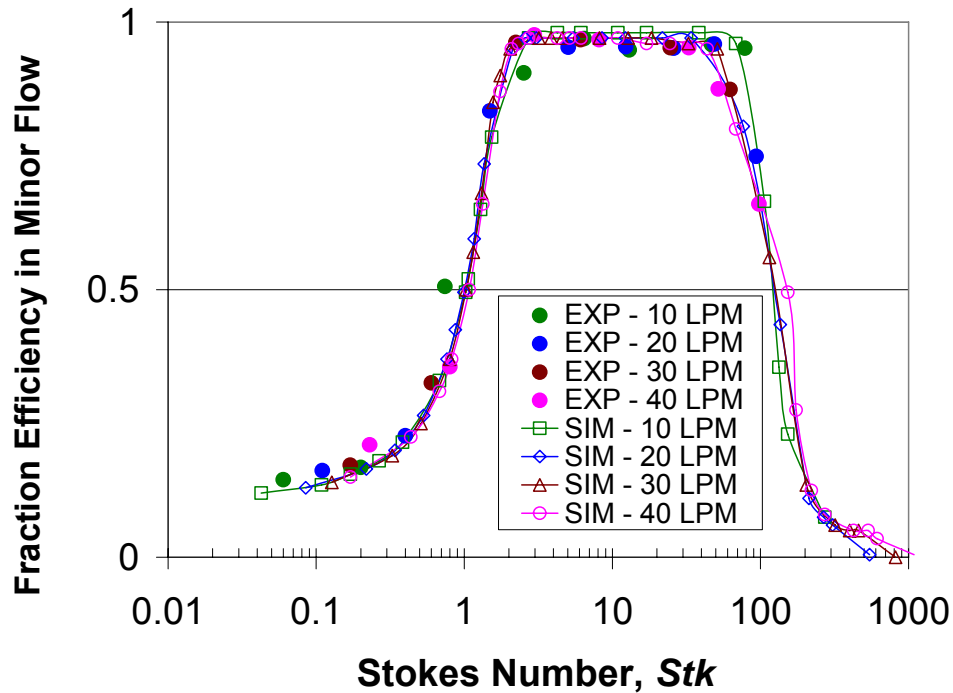

Figure 55 Performance of the CSVI-10B unit as a function of Stokes number, EXP (experiment) compared with SIM (numerical predictions)

The drop of the fractional efficiency curve for larger particles is typically caused by two kinds of cross-trajectories. The first cross-trajectory occurs in the inlet acceleration nozzle and receiver section. After acceleration in the inlet nozzle, a large particle, which has a relatively large stopping distance cannot follow the air flow and impacts on the other side of the cross-section, Figure 56. This figure shows typical trajectories in a CSVI unit for different particle sizes. Particles are released at points

located in one side of the inlet of the cross-section. Smaller particles, such as 5 μm, can follow the air flow and travel into the minor flow region of the CSVI, maintaining their location in the same side of the cross-section, Figure 56(a). However, when the particle size reaches 10 μm, it starts to exhibit a crossing-trajectory behavior, i.e. it crosses the center of the cross-section and travels into the opponent side of the minor region, Figure 56(b). Further, when the particle size reaches 22 μm, the crossing-trajectory effect can cause the particles to hit the wall of the receiver nozzle in the minor region, Figure 56(c). When the particle size reaches 30 μm, it can even hit onto the side wall of the acceleration nozzle as shown in Figure 56(d). Onset of the crossing trajectory can be delayed by a well-designed geometry of the acceleration nozzle.
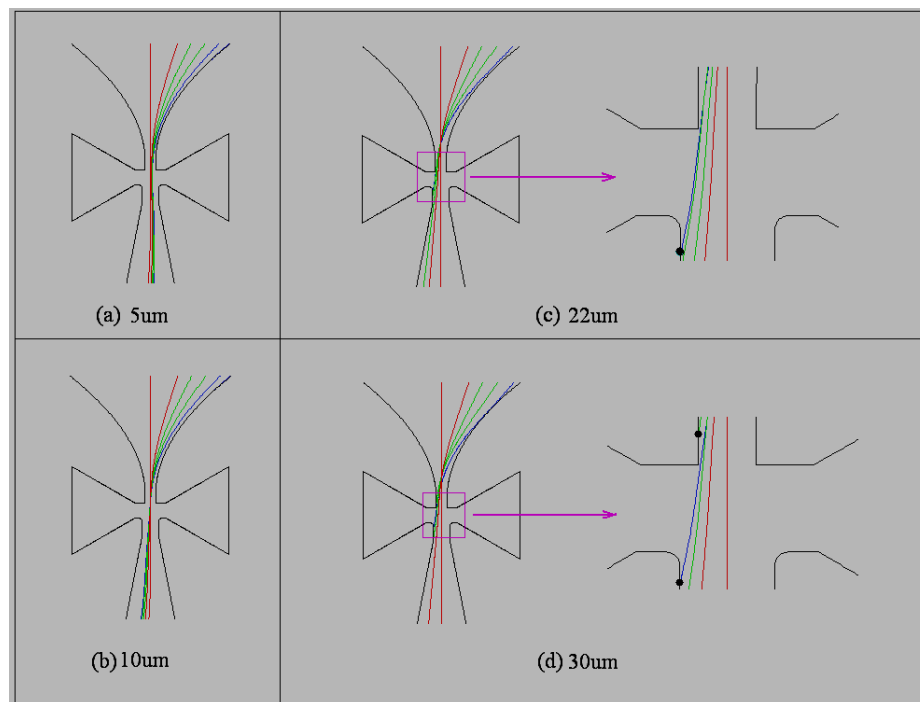

Figure 56 Crossing trajectories for large particles in a typical CSVI

The second crossing trajectory is the opposite-side trajectory, which happens near the exhaust tube of the minor region. Large particles, if not deposited by the crossing-trajectory phenomenon in the acceleration nozzle and the receiver nozzle, will enter into the minor region. However, if the particle is large enough, it could hit the opponent wall of the minor exhaust tube. Figure 57 shows these trajectories for 30 μm particles in the CSVI-10B unit. It can be seen that when 30 μm particles are introduced into the CSVI, they encounter a first cross-trajectory in the acceleration nozzle and the receiver nozzle near the slot; then a second opponent-side in the minor tube. These two trajectories combined together result in ever-increasing wall losses with increasing particle sizes.
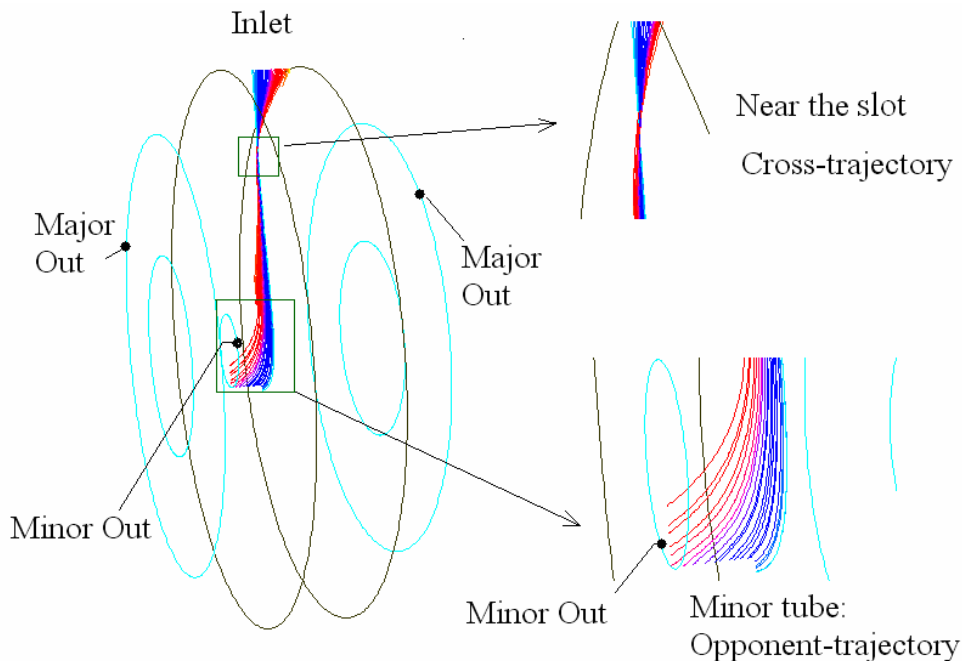

Figure 57 Opponent-side cross-trajectories in the CSVI-10B unit

Pressure drop is checked and compared with experimental measurements for major and minor flows for the CSVI-10B unit. The simulations employed the geometry shown in Figure 58, which includes a computational domain that starts at the inlet of the CSVI-10B unit and ends at the major/minor flow exhaust tubes. Because the downstream volume is relatively large compared to that in the CSVI, mixed cells are used in the mesh, which contains about 2 million cells.
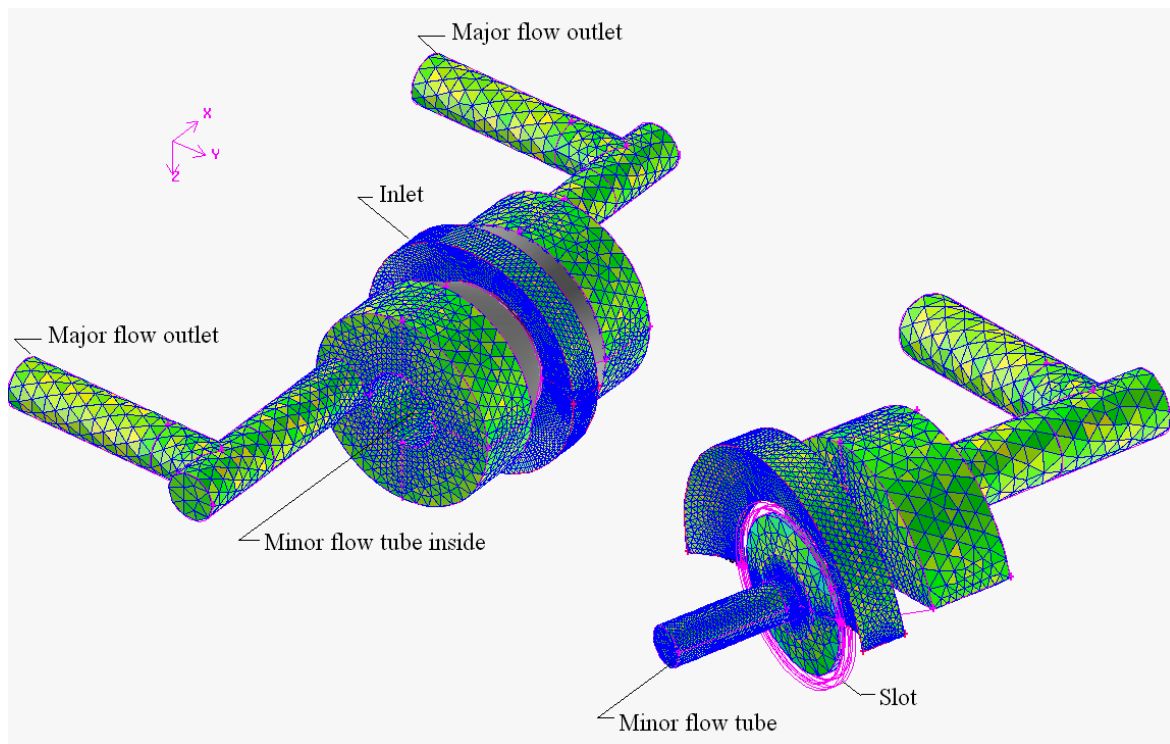

Figure 58 Computational domain in the simulation for the CSVI-10B unit

Two different diameters for the major flow exhaust tube were tested, namely, 5.59 mm (0.22") and 10.16 mm (0.4"). The 5.59 mm (0.22") is approximately the same as that of the real unit used in the experiments and the 10.16 mm (0.4") dimension is a

trial diameter with the expectation having smaller pressure drop. It can be seen that numerical prediction for pressure drop agrees well with the measurement data for the 5.59 mm (0.22") case, Figure 59. However, the predictions are slightly lower, possibly because the major flow exhaust tube size is not exactly the same as in the experiment, or perhaps there are some other losses in the experiment. However, when the major flow exhaust tube size is enlarged to 10.16 mm (0.4"), its pressure drop can decrease about 20-25%. A larger exhaust tube is required to decrease the pressure and it will also cause the volume of the unit to be larger.
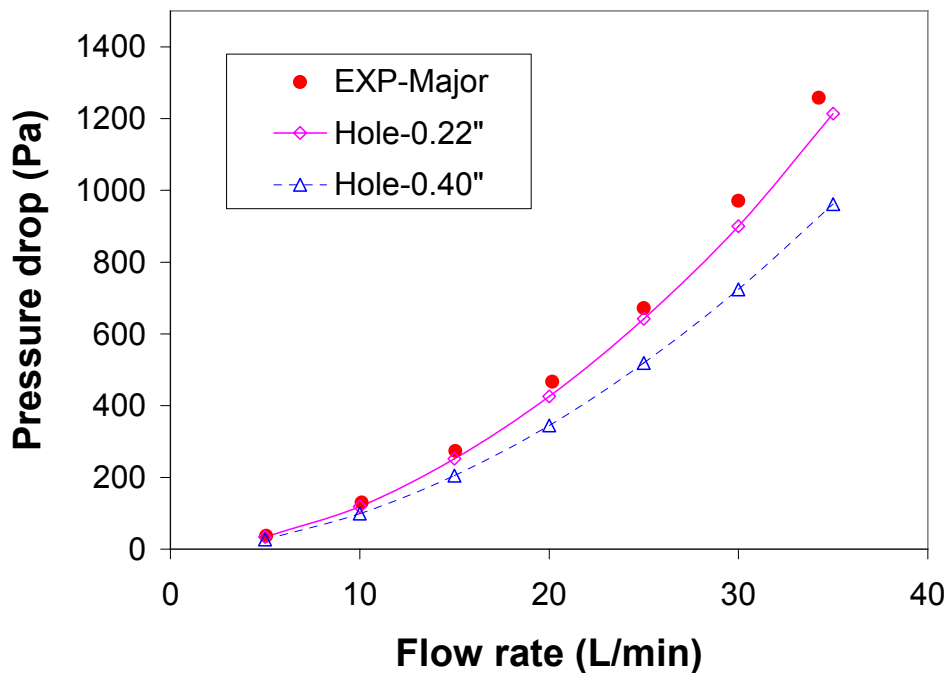

Figure 59 Prediction of pressure drop for CSVI-10B unit. Comparison of simulated and experimental results at different flow rates

When pressure coefficient is defined as Equation (65), the *K* value for CSVI-10B unit is about 2.0 at flow rate of 10 L/min. The *K* value is smaller for the CSVI unit as compared with other types of concentration devices like the cyclone, which has a *K* value above 3.0. When the major exhaust tube size is enlarged to 10.16 mm (0.4"), the *K* value of the CSVI at a flow rate of 10 L/min is reduced to be about 1.6, Figure 60.

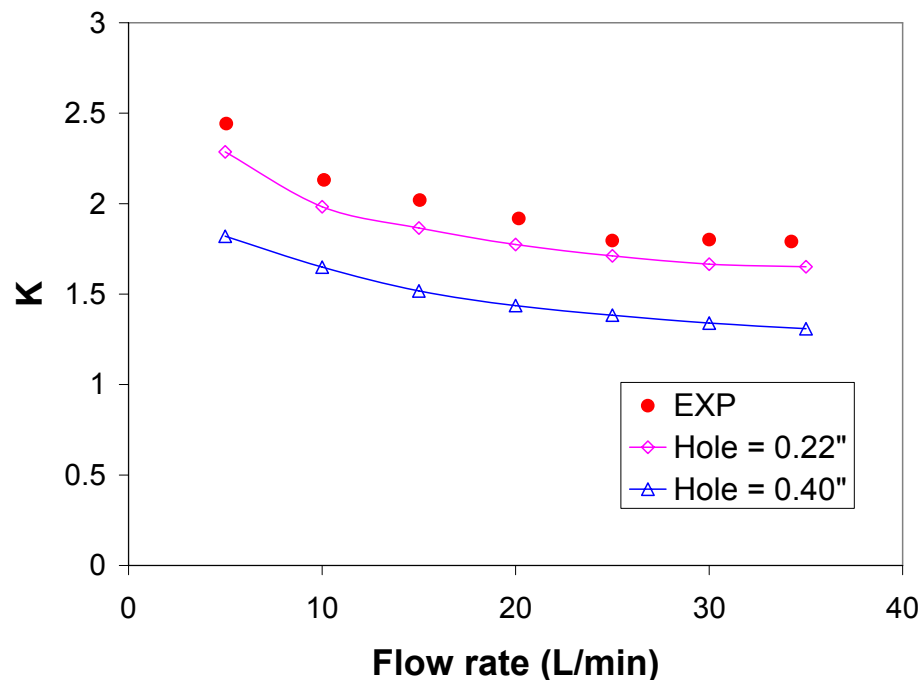Figure 60 Prediction of *K* value of pressure drop for CSVI-10B unit, compared with experiments at different flow rates

5.3.2 100 L/min CSVI Unit

An early 100 L/min unit, CSVI-100A, had a 35.56 mm (1.4") critical zone radius and a 0.508 mm (0.020") slot width. When operated at 100 L/min, it had an average air velocity of 14.6 m/s at the slot corresponding to a flow Reynolds number of 460. An

unusual phenomenon was observed during testing of this unit, namely, it generated a pulsing noise and its maximum experimentally measured minor fraction efficiency was about 30%. Deposition was observed on the internal surface walls of the unit when the unit was tested with sizes that should have been transported to the minor flow exhaust port.

Three-dimensional simulations were conducted to analyze the flow field and an unusual flow pattern was observed, Figure 61. For comparison with this unusual flow, the stable flow in CSVI-10A unit can be seen in Figure 52. The CSVI unit has an axisymmetric geometry and the flow should be circumferentially symmetric and the jet from the inlet acceleration nozzle should impinge directly into the receiver nozzle and develop symmetrically in the center of the minor region, i.e. the flow should only develop in the radial direction and there should be no circumferential flow if it is stable. This stability is predicted for both CSVI-10A and CSVI-10B units in which the flows were stable. However, the velocity contours in the CSVI-100A at different cross-sections showed strong asymmetric features in both the circumferential direction and along the center of minor region. The jet attached to one side of the wall of the CSVI-100A unit and developed non-uniformly in the minor region, and there was a strong flow in the circumferential direction.
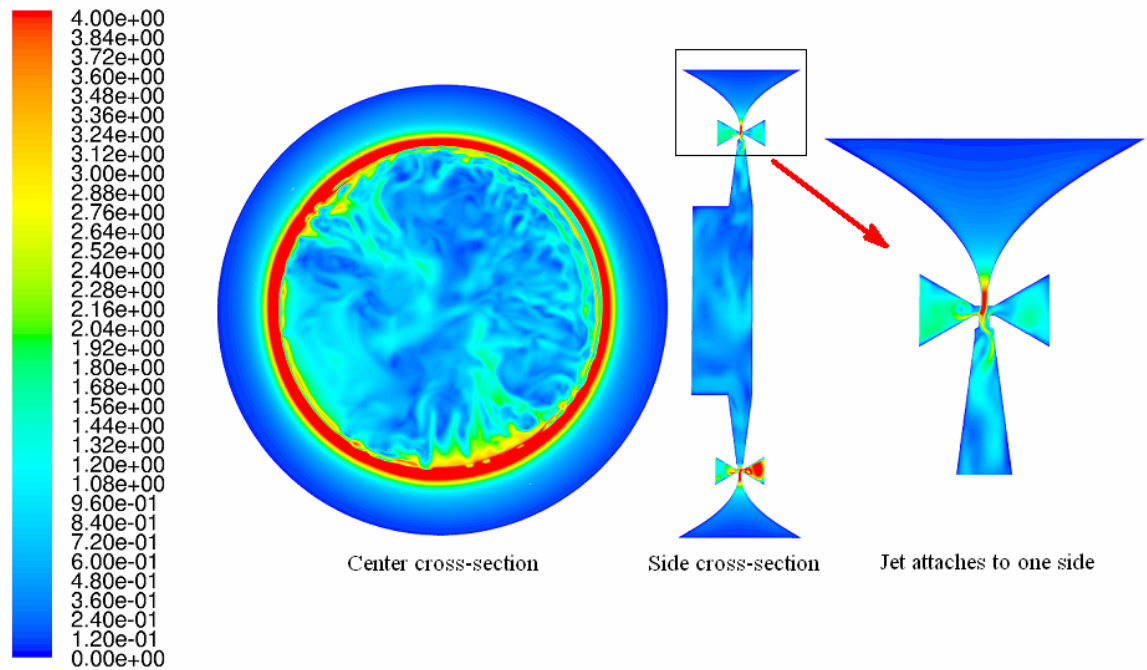
Figure 61 Velocity contours of the CSVI-100A unit at different cross-sections. Right figure is an enlarged view of the upper half of the center figure.

Figure 62 shows pathlines of air flow that originate from a line source at the inlet of the CSVI-100A unit. It can be seen that after the fluid gets into the minor region, it does not flow toward the center as expected, but diffuses and develops along the circumferential direction. This 3D flow could cause the internal flow velocity in the minor region to be much higher than the average velocity of the jet at the slot. When the flow is stable as in CSVI-10A, the maximum velocity is about 1.2X to that of average velocity in the slot. But it will increase to about 2~2.5X when the flow is unstable as in the CSVI-100A. For example, the averaged velocities at the slot of CSVI-10A and CSVI-100A are both 14.6 m/s. But the maximum velocity is about 18 m/s in the CSVI-10A with stable flow and 32 m/s in the CSVI-100A with unstable flow.
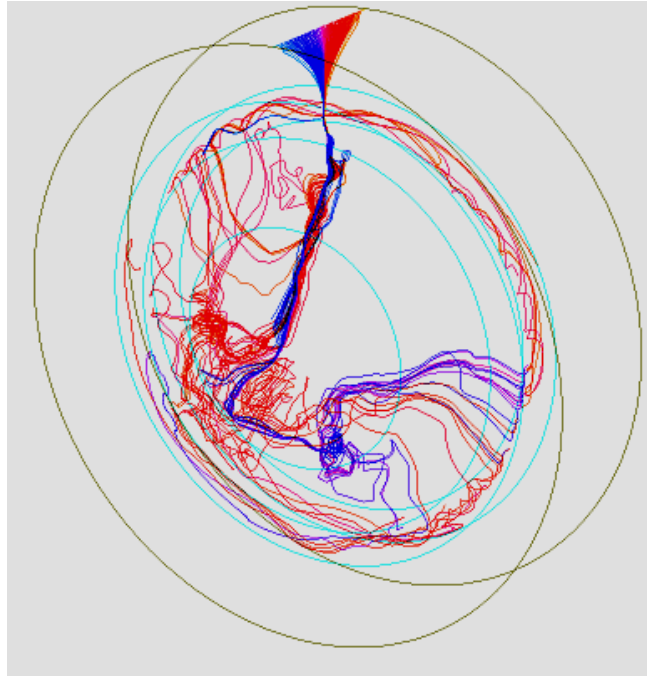
Figure 62 Pathlines of the air flowing from the entrance of the acceleration nozzle to the receiver nozzle of the CSVI-100A with unstable flow

Unsteady simulations for this unit were conducted to check the velocity contours near the critical zone in the side cross-section to observe if the flow changes with time and if the jet is fluctuating as it enters the critical zone. An unsteady flow study for CSVI-10A unit showed that the velocity contours in cross-sections were constant with time. Figure 63 shows a few contours of velocity at the side cross-section at different times for the CSVI-100A and it can be seen that the flow patterns in that device change with time. The different colors represent different velocities with the red color being the highest velocity. In this figure, it can be seen that the jet does not enter into the receiver nozzle symmetrically, but rather attaches onto one wall. With time, the jet also shifts slightly from right to left and it does not stay attached at the same place. Further, it can be observed that the flow inside the major region also varies with time and it

demonstrates asymmetry between the two major flow regions. Both the steady and unsteady studies showed that when the jet impinges into the minor region in the the CSVI-100A unit, it tends to attach to one side of the wall and has a fluctuating feature which may cause the unstable asymmetric flow in an axisymmetric geometry.

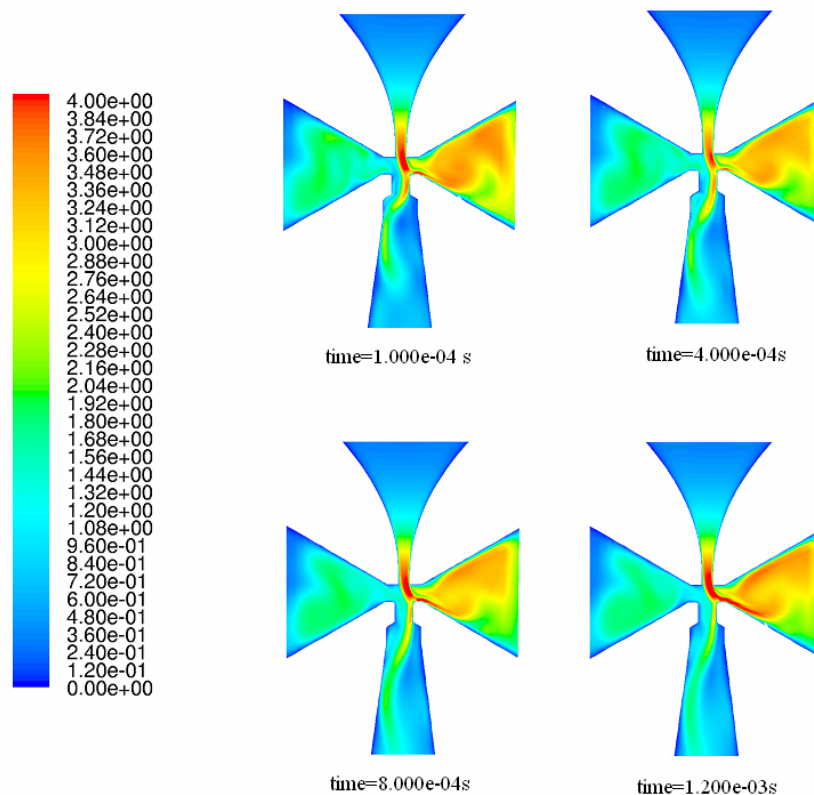Figure 63 Velocity contours at one cross-section at different times for the CSVI-100A unit

The average air velocity in the minor region for the CSVI-100A was calculated and compared with the CSVI-10A unit. The results are shown in Figures 64 and 65. Here the abscissa shows a distance to the critical zone (identified as L1 in Figure 50). It can be seen that when the flow is approaching the axis in the minor region of CSVI-10A, it is

accelerating and the average velocity is increasing because its radius R from the axis decreases faster than expansion of the width L. This implies there is a positive static pressure gradient (dP/dL) from the center of the critical zone toward the axis. In contrast, the average velocity is decreasing and the air is decelerating in the the CSVI-100A because the radius decreases slower than the width expansion, and this will produce a negative pressure gradient in the minor region, which is totally different from the pressure gradient in CSVI-10A. The positive pressure gradient could assist the flow to be stable while the negative one could make the flow unstable if the jet is not sufficiently strong. The different pressure gradient features in the CSVI-10A and CSVI-100A may be one reason for the difference in flow stability.
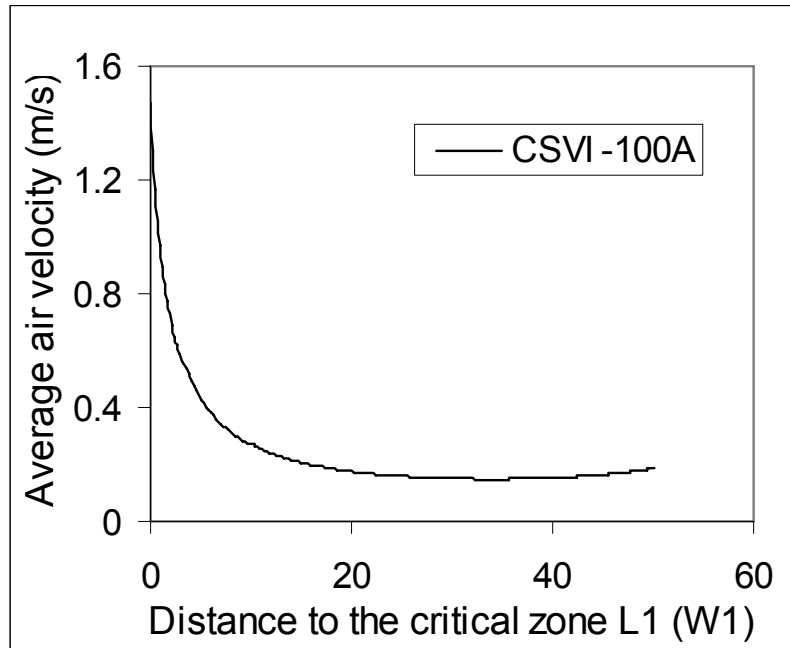

Figure 64 Average air velocity as a function of the distance from the center of critical zone in CSVI-100A
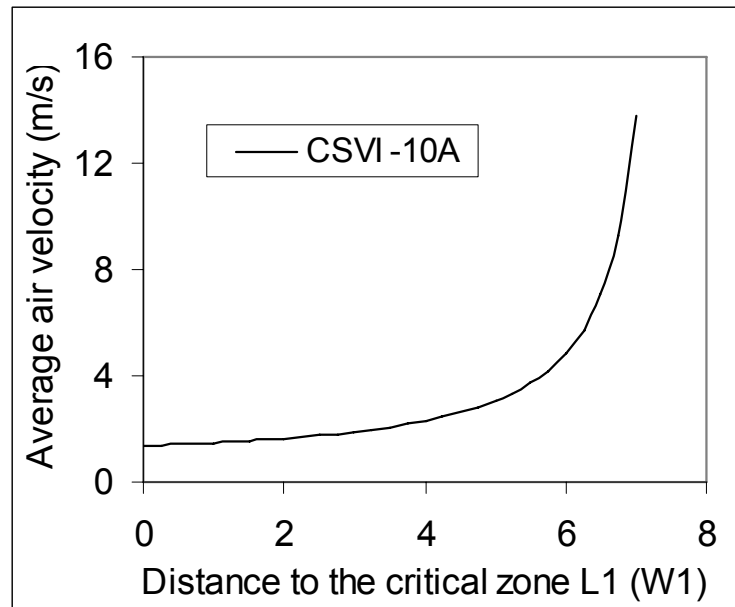
Figure 65 Average air velocity as a function of the distance from the center of the critical zone in the CSVI-10A

The pressure gradient in the minor flow region could be the dominant factor for flow stability in some cases. To verify the importance of the pressure gradient, two cases were simulated using different axisymmetric and planar-symmetric geometries with the same cross section configuration as the CSVI-10B unit, Figure 66. In the axisymmetric unit, the flow will accelerate significantly in the exhaust tube of the minor region due to the decreasing radius and there is a positive pressure gradient towards the axis. The simulation showed that the flow for this case was stable and that the jet impinges into the receiver symmetrically and develops smoothly. However, in the planar-symmetric case, the cross-section area of the flow does not decrease and the flow does not accelerate as much as in the axisymmetric unit. The flow shows an asymmetric feature in the major flow regions where the jet is attached to one side of the wall of the minor region and

does not impinge symmetrically. The two different flow conditions suggest that the positive pressure gradient could be an important factor to assist the stability of the flow in virtual impactors and that the CSVI should be essentially more stable than an LSVI unit under certain conditions.
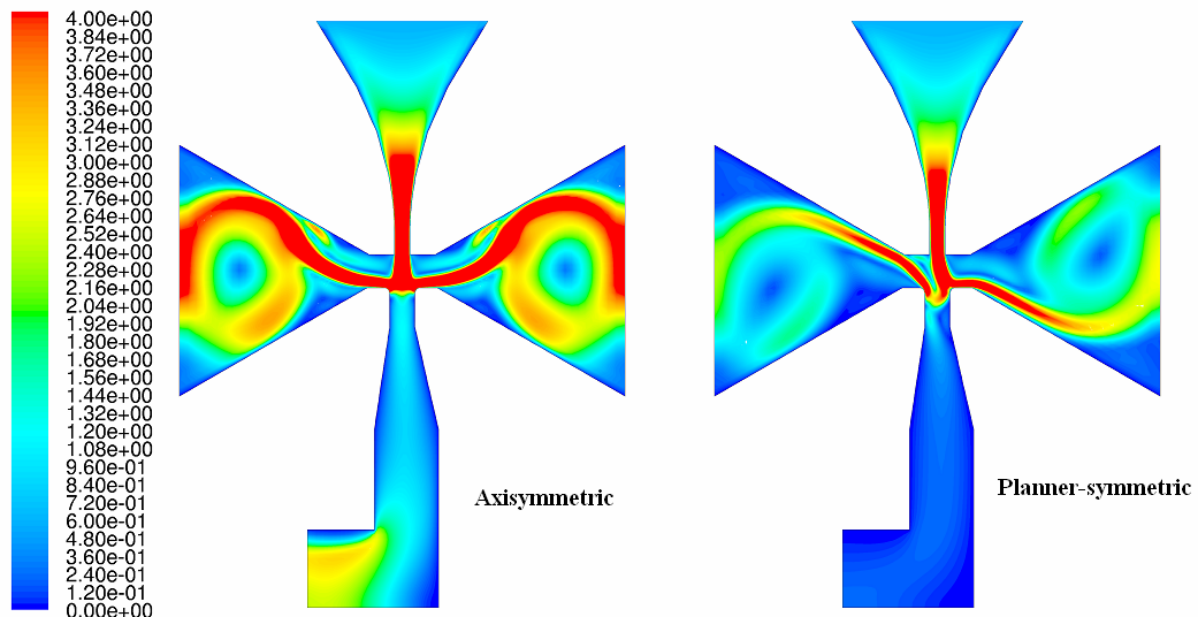
Figure 66 Different flow behaviors in axisymmetric and planar-symmetric geometries

Another possible reason for flow instability in the CSVI-100A unit is that it has a relatively large minor region volume where the jet from the critical zone develops. The jet in the minor flow region is composed of 10% of the total mass flow. The initial velocity is about 14.6 m/s but the jet expands and decelerates to have a velocity about 1.2 m/s in a short distance. Then, the 1.2 m/s jet continues to flow passing a 35.56 mm (1.4") distance towards the axis in the minor region during which the jet may break up.

The jet has a time scale τ to indicate its decaying feature which is determined by its original velocity. If a parameter is defined as $\dot{Q}\tau/V$, where $\dot{Q}$ is flow rate, V is minor region volume and τ is a jet time scale, it can be considered as the ratio of the dynamic jet momentum to the static inertia of all the air residing in the minor region, which has a volume V. It is reasonable to assume that if a developing jet has a larger value of $\dot{Q}\tau/V$, it can be more stable because it has a stronger initial momentum and could reach farther into the minor region before it breaks up. The value of $\dot{Q}\tau/V$ for CSVI-10A is about 25 times that of the CSVI-100A, which indicates that the minor region volume in CSVI-100A is too large relative to its jet characteristics.

Based on these considerations, a new unit CSVI-100B was designed and fabricated with a smaller $\dot{Q}\tau/V$ value by using a shorter 17.02 mm (0.67-inch) critical zone radius, and a smaller expansion angle (11°) in the minor region, and consequently a smaller minor region volume. The slot width is 0.711 mm (0.028") based on Stokes scaling. Also, the exhaust tube for the minor flow has a small size of about 3.556 mm (0.14") radius to generate a low pressure field in this tube and consequently a positive pressure gradient along the flow direction. To guide the flow near the minor exhaust tube, a small plug is inserted along the axis at the opposite side of the tube to eliminate a small region where flow recirculation may occur as shown in Figure 67. A photo of the CSVI-100B is shown in Figure 68. This unit has a total diameter of about 71.12 mm (2.8") which is much smaller than that of the CSVI-100A, 132.08 mm (5.2").
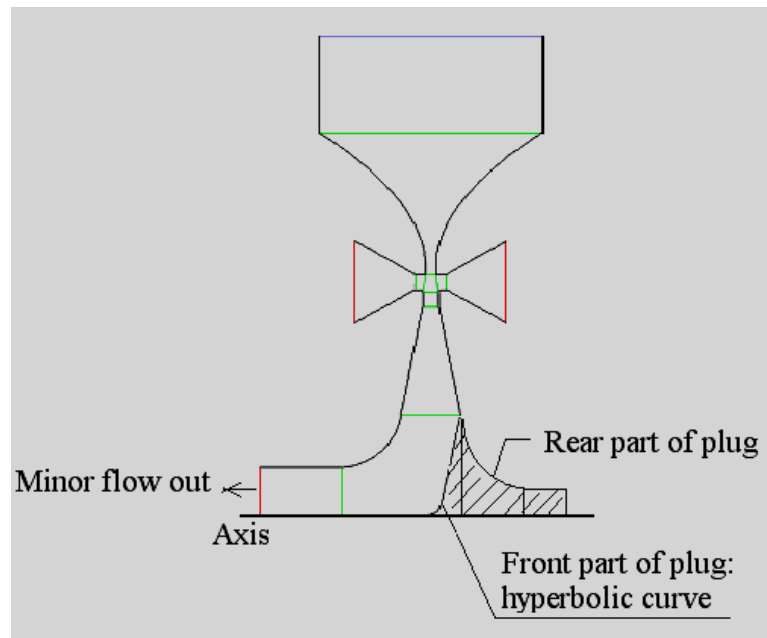
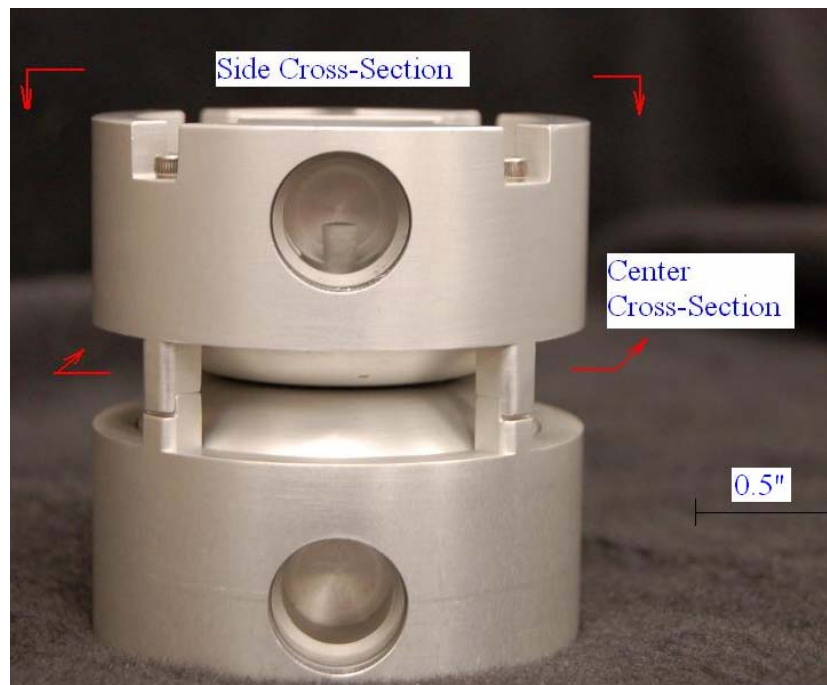Figure 67 General layout for the CSVI-100B unit

Figure 68 Photo of the CSVI-100B unit

The major dimensions of CSVI-100B are shown in Table 4 together with those of other CSVI units. Compared with the CSVI-100A, this new unit is more compact in size with a total diameter of about 71.12 mm (2.8"). Due to its smaller radius and expansion angle in the minor flow region, the velocity in the minor region is decreasing from the center of the critical zone for a short distance (about 6W1), and then starts to increase again. Its average velocities in the minor region at different locations are shown in Figure 69. The average velocity of the jet at slot W1 is about 21 m/s, which is larger than that in the CSVI-100A (14.6 m/s), which means that the jet in the CSVI-100B can reach farther than that of the CSVI-100A before the jet breaks up. These two aspects imply that the CSVI-100B unit could have a stable flow and this is verified in 3D simulation. Figure 70 shows that air pathlines starting at the inlet of the CSVI-100B unit, and the pathlines indicate clearly that the flow is stable inside this unit. All the air streams impinge into the minor flow region and develop along the radial direction. There is no air flowing in the circumferential direction and the total flow behaves in an axisymmetric manner.

Table 4. Major dimensions for CSVI units

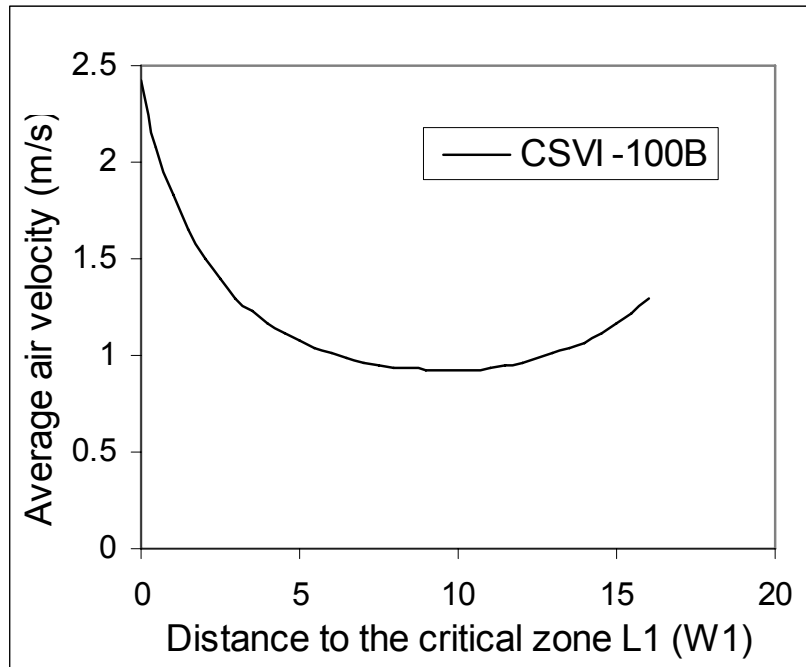| Unit	Rt (mm)	Rc (mm)	$W1$ (")	R/W1	Ro (mm)
CSVI-10A	20.32	3.556	0.508	0.25	1.422
CSVI-10B	20.32	7.62	0.508	0.25	1.778
CSVI-100A	66.04	35.56	0.508	0.25	15.24
CSVI-100B	35.56	17.018	0.7112	0.25	7.112

Figure 69 Average air velocity as a function of the distance from the center of the critical zone for the CSVI-100B
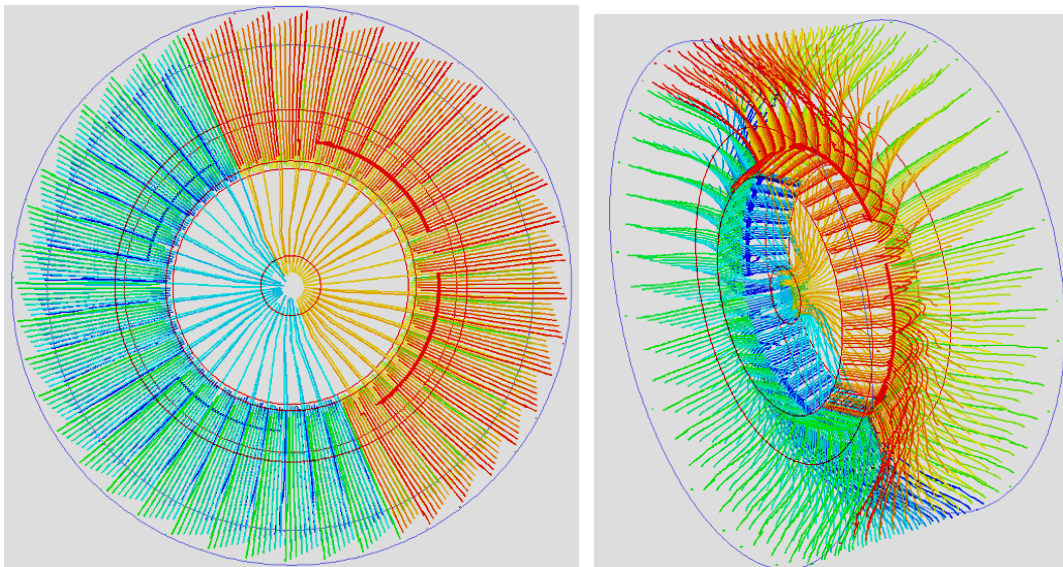

Figure 70 Air pathlines in the CSVI-100B

A CSVI-100B unit was fabricated and tested. There was no longer a noise during operation; however, the fractional efficiency for 6 μm AD particles was only increased to about 78%, which was lower than expected. When the internal wall deposition was checked, it was found that the majority of the wall was clean. But, a clear narrow strip of deposition was found downstream of each of the four posts, where the posts align and support the two halves of the CSVI, Figure 71. The posts have a width of about 7.112 mm (0.28") along the circumferential direction, which was suspected to be too large for a 17.018 mm (0.67") radius unit in which the wake flow downstream of the post could disturb the flow in the inlet accelerating nozzle and could propagate into the minor flow region. This was verified in a simplified numerical simulation in which the four posts were included in the geometry of the CSVI-100B unit. The velocity contour at the center cross-section of the CSVI unit is shown in Figure 72, which indicates a low-velocity flow downstream of each post. The low-velocity region has a velocity magnitude of about 0.4 m/s, which is lower than the nearby region value of about 2.8 m/s, and the velocity gradient can cause particles to deposit onto the surface in the low-velocity region.
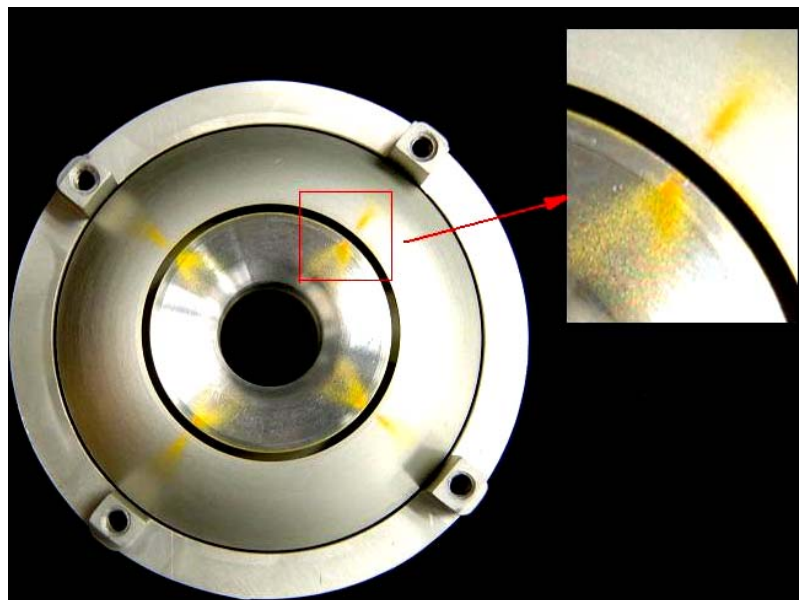
Figure 71 A photo taken in the experiment to show the particle deposition downstream of the posts in the CSVI-100B unit
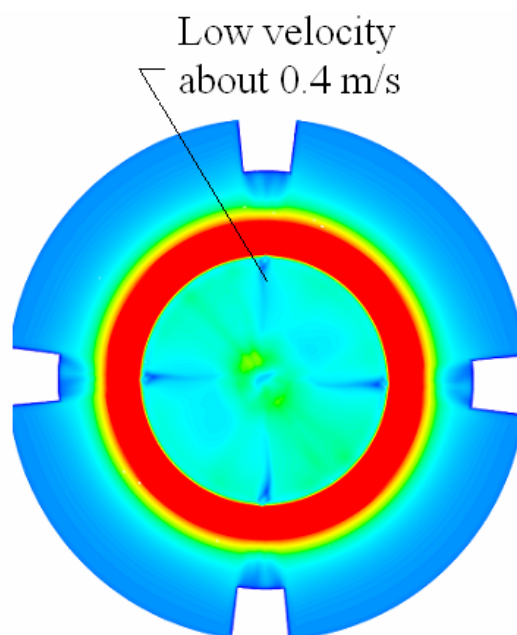

Figure 72 Velocity contour using numerical simulation to indicate a low velocity field corresponding to the particle deposition downstream of the posts

Numerical simulations were then conducted to optimize the size and location of the posts and the whole unit to reduce the effect of the wake flow of the posts. It could be a solution to increase the whole size of the unit and to reduce the inlet air velocity. However, this will also increase the length of the post to connect the two sections of the CSVI unit and the disturbance to the flow will also increase by the posts. It also could be a method to resolve this problem by a well-designed geometry of posts to guide the flow from the inlet of the CSVI and to reduce or eliminate the disturbance caused by the posts. Elliptical, triangular, and bullet-shaped posts were tried as shown in Figures 73 and 74 and it was found that the flow was stable with each of these posts. Figure 75 shows one of these results using elliptical-shape posts. Compared to the original rectangular posts with a low-velocity region of 0.4 m/s, the elliptical ones result in a little better flow with a low velocity region of 1.45m/s so it has a smaller velocity-gradient with the environmental flow. However, the low-velocity region can not be totally eliminated. This is probably due to the relatively large size of the posts and their close proximity to the critical zone. The posts are used to connect the two nozzles of the CSVI and each post contains a small bolt inside so the size of the post can not be reduced too much or it can not hold the bolt. When the posts are embedded inside of the CSVI, they blocked the area of the air in take with about 12° at each of the posts in the circumferential direction and the disturbance of the post is strong enough to propagate into the critical zone and the minor region of the CSVI with a small diameter.
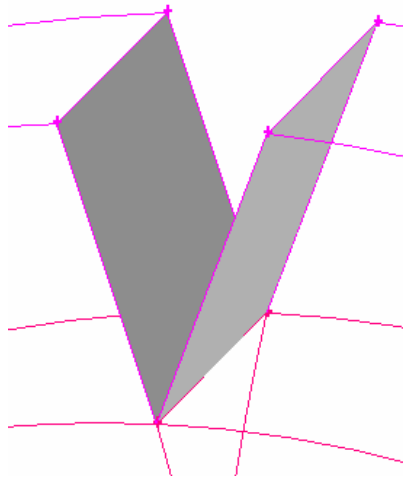
Figure 73 Triangular post
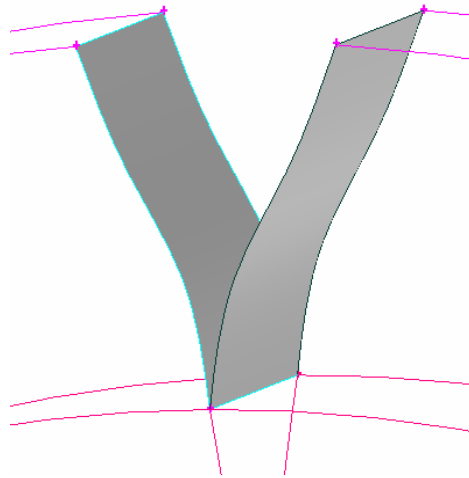
Figure 74 Bullet-shaped post
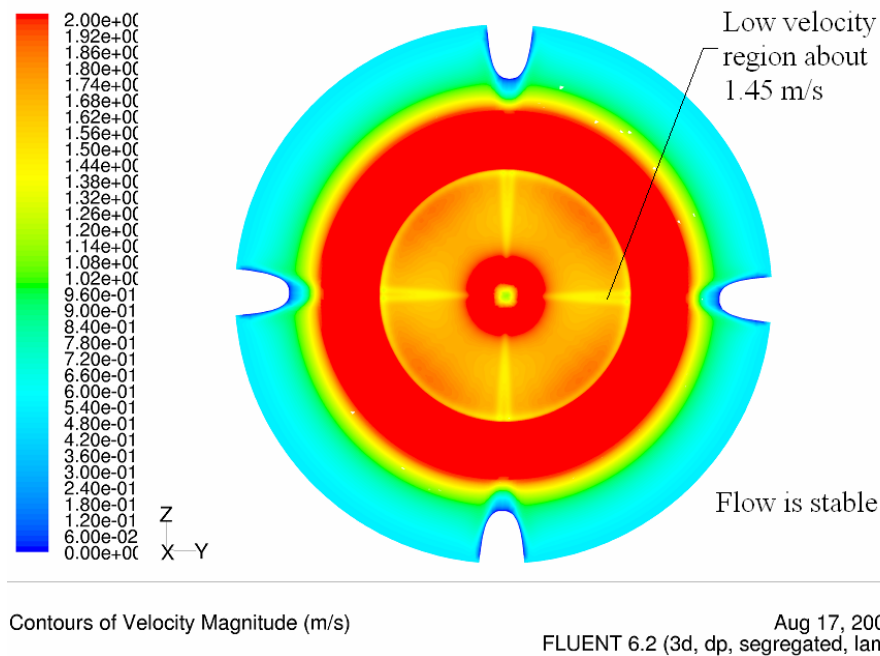
Figure 75 Velocity contour at the cross-section of the CSVI unit with elliptical-shaped posts

A new unit CSVI-100C was designed with the posts moved outwards about 11.94 mm (0.47") away from the CSVI unit so the incoming air will be taken into the CSVI unit with a much lower velocity around the posts and the wake effect of the posts will be decreased significantly, as shown in Figure 76. For comparison, the original concept of using the post inside of the CSVI is also shown in Figure 77. From these two figures, the locations of the posts can be found to be totally different. Simulation for the moved out post unit showed that the flow was very stable and the post had almost no effect on the flow and the disturbed low-velocity region is eliminated, Figure 78.
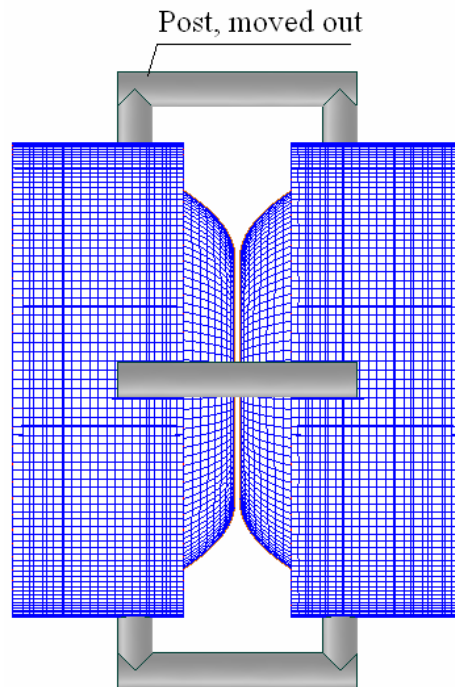
Figure 76 Post configuration for CSVI unit CSVI-100C after moving the posts
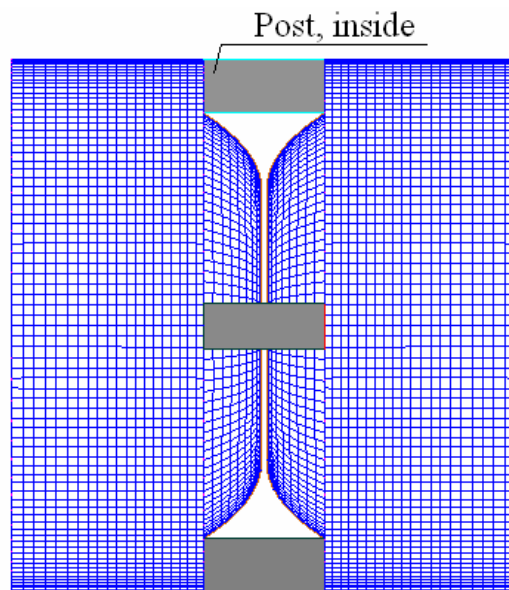
Figure 77 Post configuration for CSVI unit CSVI-100B before moving the posts

Contours of Velocity Magnitude (m/s)

Aug 28, 2006
FLUENT 6.2 (3d, dp, segregated, lam)
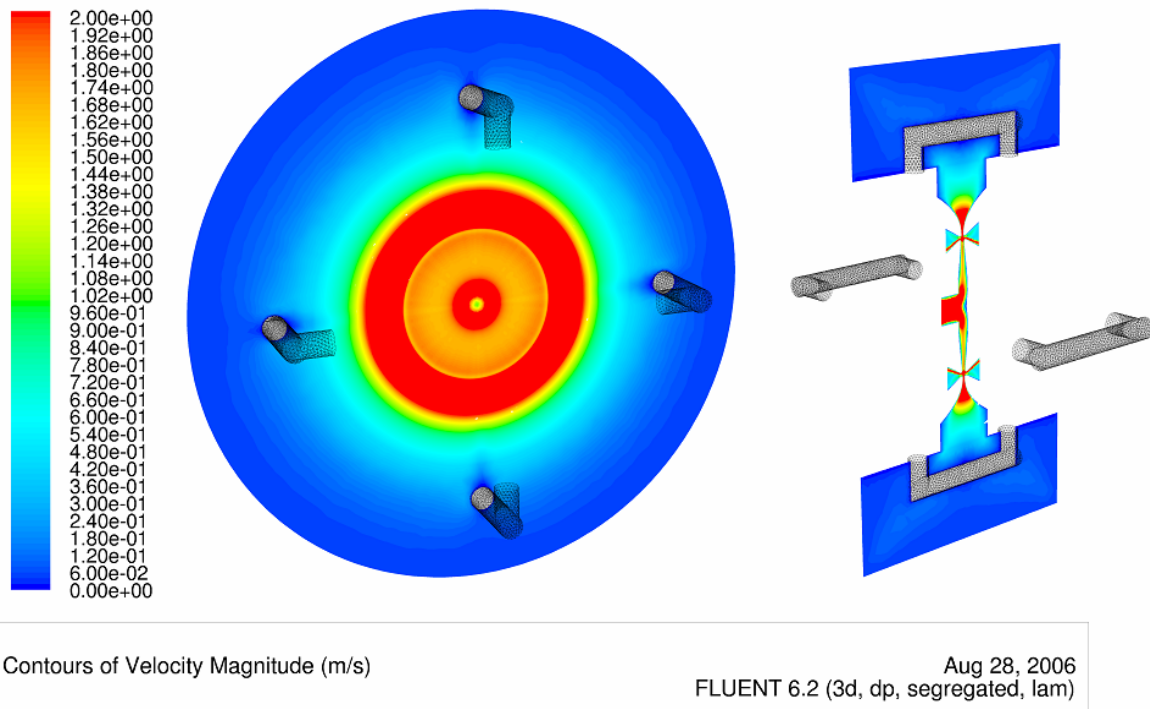
Figure 78 Velocity contours on cross section of the moved out post CSVI -100C unit, stable flow

The CSVI-100C unit was fabricated and tested. Comparing the post-inside unit CSVI-100B, the moved out post unit CSVI-100C has better minor flow collection efficiency than that of the CSVI-100B unit as shown in Figures 79 and 80. The fraction efficiency of CSVI-100C was found to increase to about 95% in a wide dynamics range about 10X while CSVI-100B has a maximum collection of only about 80%. Numerical predictions have good agreement with the experimental results for both units.
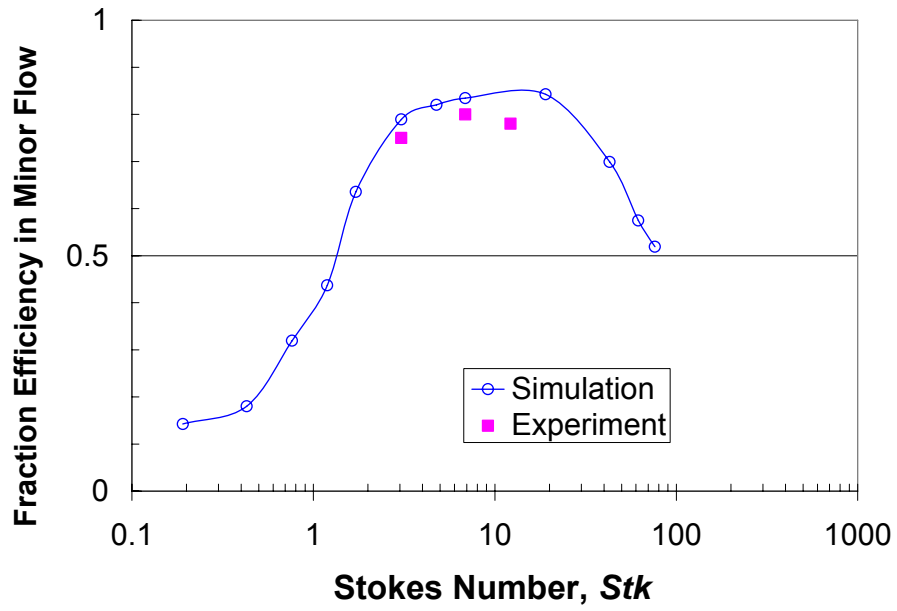
Figure 79 Performance of CSVI-100B unit
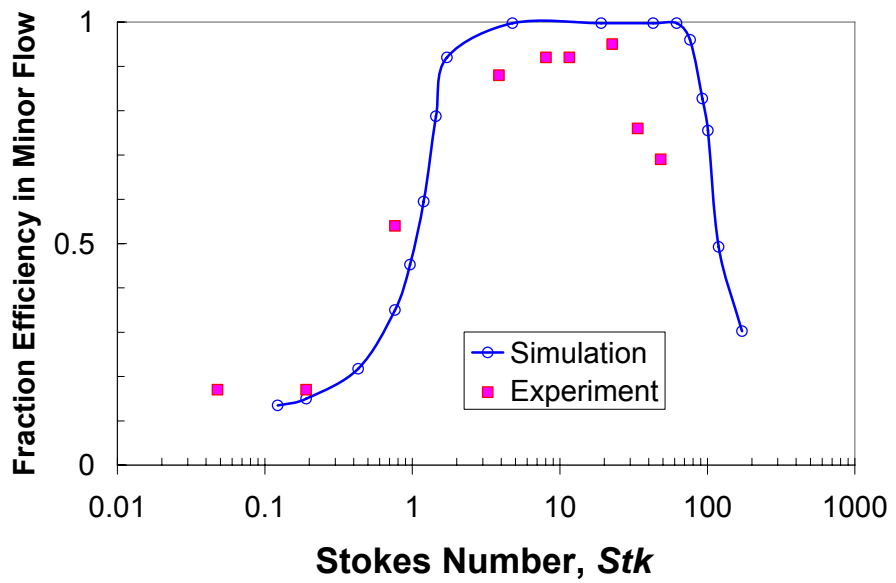
Figure 80 Performance of CSVI-100C unit

The performance of the virtual impactor was sensible to its dimensions and operation conditions (Marple 1980, Hari *et al.* 2006). From the viewpoint of the flow stability, these dimensions and operation conditions also have important effects. For the CSVI, another important performance is the wall loss which should be minimized and it indicates the percentage of the particle deposition on the internal wall of the impactor. In this study, five factors were varied to find the trend of their influence on the flow stability including the inlet nozzle curve, the receiver width W_1, critical zone radius R_C, round fillet radius in the receiver nozzle R_i, and minor flow ratio f. For each influence factor, the simulations started from an original case having the same cross-section configuration as the CSVI-100C unit which was tested and verified to be stable and the value of the factor was increased or decreased and then the flow was checked to be stable or not. At the same time, the wall losses were examined and compared to find the influence trend of the factors.

(1) Inlet nozzle curve

The curve of the inlet nozzle will determine the velocity distribution of the jet upstream of the critical zone. If the flow in the inlet nozzle was fully developed, the flow may tend to be unstable in the virtual impactor; if not fully developed, i.e., still developing, it tends to be stable. Part of the total flow expands to the minor flow in the receiver section and the exact expansion ratio of this stream of minor flow should be:

$$f = \frac{W_1}{W_i}$$

Here, W_i is the width of the partial flow in the jet upstream of the critical zone. The value of W_i may be different when the flow in the inlet acceleration nozzle is fully developed or not. It is straightforward to assume that W_i is shorter for fully developed flow than the developing one because the former flow has a sharper velocity distribution. In other words, the expansion ratio f for the fully developed flow could be larger than the developing one, in sequence, more possibly to be unstable.

In a development design for the inlet curve to improve the dynamic range, the shape of the curve has been developed from gradual to parabolic then to elliptical in different CSVI generations I to III correspondingly. GEN I has a gradual inlet curve, GEN II is parabolic, and GEN III is elliptical. The flow of the jet near the critical zone was adjusted to be more developed and the flow direction was aligned to be more vertically normal to the axis. The objective of these modifications was to modulate the cross-trajectory effect and guide the heavy particles to follow the jet impinging down into the receiver nozzle and to prevent them from cross-hitting to the other side of the wall. The dynamics range from GEN I to III was increased under careful design. Flows in GEN I and II were stable and the minor fraction efficiencies were high as expected. However, in GEN III, with the unit name CSVI-100A, the flow in the unit was found to be unstable. A conclusion may be made here that the curve of the inlet nozzle affects the flow velocity distribution of the jet and if it causes the flow to be more developed, the CSVI unit will be more unstable, and vice versa.

(2) Receiver width W_1

Based on similar analyses in (1), receiver width W_1 affects the flow expansion ratio f and it is reasonable to assume that the larger W_1 could cause the VI flow to be unstable.

(3) Critical zone radius R_C

Critical zone radius R_C will determine the jet velocity and in sequence, the jet time scale and the minor flow region volume when other conditions remain the same. Smaller radius units can have a stronger jet and smaller minor flow volume and the jet can reach farther and tends to be more stable in certain flow conditions. In contrast, large critical zone radius will decrease the jet velocity and increase the minor region volume. From the CSVI-100C unit, when the radius R_C was increased gradually, the flow was found to start to be unstable when the radius reached 0.8". However, while the smaller R_C can maintain a more stable flow, the wall loss tends to increase.

(4) Round fillet radius R_i

It was found that a larger round fillet radius R_i could result in unstable flow because the major flow makes a turn along a larger curvature. Based on the CSVI-100C unit, when the R_i increases from its 0.25W to 0.5W, the flow starts unstable behaviors. However, a larger R_i could decrease the wall loss at the receiver radius.

(5) Minor flow ratio f

The minor flow ratio f determines the concentration times and its typical value is 10% to obtain a 10X concentration. This ratio also determines the expansion ratio. Small

f means less mass of air flows into the minor region and results in a higher expansion ratio, consequently, an easier unstable flow.

5.4 Summary

An instability phenomenon in a CSVI unit was simulated using FLUENT and the possible reasons were analyzed. Reverse pressure and a too large volume of the minor flow region may cause the unstable flow in the CSVI and result in particle losses everywhere in the unit. CFD successfully designed a new CSVI unit which has a stronger jet to maintain a stable jet developing in the minor region. Post effect was also analyzed to find its influence on the flow and particle behavior in the CSVI and an improved design was suggested. The final design of the CSVI unit was found to have high collection efficiency in the minor flow and achieved a wide dynamic range of about 50X. The predicted performance of the CSVI was compared with experimental results and excellent agreement was obtained.

Five factors were analyzed to find the trend of influence on the stability of the CSVI including the inlet nozzle curve, the receiver width W_1, critical zone radius R_C, round fillet radius in the receiver section R_i, and minor flow ratio f. These can be used in the design of a more stable CSVI unit.

CHAPTER VI

CONCLUSION AND FUTURE WORK

In this study, CFD was used as the design basis for impactors, cyclones, and virtual impactors, with flow conditions that are both laminar and turbulent. Comparisons with experimental results show that CFD was able to successfully predict the particle behavior in the laminar flow and in some turbulent flows where turbulent dispersion is not dominant. The $k - \omega$ turbulent model is verified to be a suitable turbulent model to study particle behavior in low Reynolds turbulent flow. RSM is verified to be useful for the flow in complex curvature geometries. However, deposition studies still need to be improved for the small particles or particles with small Stokes numbers in turbulent flow in which turbulent dispersion is important.

Separated-mesh technology is also shown to be a useful approach to apply CFD to study complex geometries. This is reflected in the shell-volume technology for 3D VOF simulation and the turbulent heat transfer studies in the cyclones. Methodology discrepancies between DPM and experiments for particle trajectory calculations are analyzed and possible solutions are suggested.

Some special physical phenomenon are also analyzed. Secondary impaction was observed in the Jet-in-well impactor, a compound impaction was defined, and the effect of the ratio of well-to-jet on the total collection was studied, which could be used as a reference for the design of such impactors. A narrowing-jet inward spiral was found in the cyclone and CFD provides a vivid description for the special flow structure in the cyclone, which can explain the small cutpoint Stokes number and a special deposition

pattern of the cyclone. A model could be developed based on some other considerations for this narrowing jet concept to predict particle behavior inside cyclones with similar geometries. Unsteady 3D flow, cross-trajectory for heavy particles, and wake flow caused by support/alignment posts in the virtual impactors are analyzed with CFD to explain some problems in the experiment and then used for improvement design. In the future, CFD could be used for the systematic design for the CSVI units to be put inside plenums to achieve an optimum design for the size of the plenum.

REFERENCES

Akpinar, E.K. (2005), Evaluation of Convective Heat Transfer Coefficient of Various Crops in Cyclone Type Dryer, *Energy Conversion and Management,* 46: 2439-2454.

Ataki, A. and Bart, H.J. (2004). The Use of the VOF-Model to Study the Wetting of Solid Surfaces. *Chem. Eng. Technol*. 27(10):1109-1114.

Bergman, W., Shinn, J., Lochner, R., Sawyer, S., Milanovich, F., Mariella, Jr. R. (2005), High Air Flow, Low Pressure Drop, Bioaerosol Collector Using a Multi-Slot Virtual Impactor. *J. Aerosol Sci*., 36:619-638.

Biswas, P and Flagan, R.C. (1988). The Particle Trap Impactor. *J. Aerosol Sci.* 19(1):113-121.

Black, R.S. and Shaw, M.J. (2002). Presentation at the Scientific Conference on Obscuration and Aerosol Research. U.S. Army Research, Development and Engineering Command/Edgewood Chemical Biological Center, Edgewood, MD.

Burwash, W., Finlay, W., and Matida, E. (2006). Deposition of Particles by a Confined Impinging Jet onto a Flat Surface at Re=10^4. *Aerosol Sci. Technol*, 40:147-156.

Choudhury, D. (1993). *Introduction to the Renormalization Group Method and Turbulence Modeling*. FLUENT Inc., Technical Memorandum TM-107.

Erdal, F.M. and Shirazi, S.A. (2004). Local Velocity Measurements and Computational Fluid Dynamics (CFD) Simulations of Swirling Flow in a Cylindrical Cyclone Separator. *J. Energy Resources Technol.*, 126(4):326-333.

Fan, F. G., Ahmadi, G. (1993). A Sublayer Model for Turbulent Deposition of Particles in Vertical Ducts with Smooth and Rough Surfaces*, J. Aerosol Sci,* 24(1):45-64.

Fox, R.W., McDonald, A.T., and Prichard, P.J. (2005). *Introduction to Fluid Mechanics.* 6th Edition. J. Wiley & Sons, Inc., New York, NY.

Friedlander, S.K. and Johnstone, H.F. (1957). Deposition of Suspended Particles from Turbulent Gas Streams, *Ind. Eng. Chem.* 49, 1151-1156.

Fuchs, N.A. (1964). *The Mechanics of Aerosols*. Pergamon Press, New York, N.Y.

Gimbun, J., Chuah, T.G., Choong T.S.Y., and Fakhrul-Razi, A. (2005). Prediction of the Effects of Cone Tip Diameter on the Cyclone Performance. *J. Aerosol Sci.*, 36(8):1056-1065.

Gnielinski, V. (1976). New Equations for Heat and Mass Transfer in Turbulent Pipe and Channel Flow, Int. Chemical Engr., 16:359-368.

Gotoh, K. and Masuda, H. (2000), Improvement of the Classification Performance of a Rectangular Jet Virtual Impactor. *Aerosol Sci. Technol,* 32:221-232.

Gotoh, K. and Masuda, H. (2001). Development of Annular-Type Virtual Impactor. *Powder Technol*, 118:68-78.

Griffiths, W.D. and Boysan, F. (1996). Computational Fluid Dynamics and Empirical Modeling of the Performance of a Number of Cyclone Samplers. *J. Aerosol Sci.*, *27*(2):281-304.

Gu, F., Liu, C.J., Yuan, X.G., and Yu, G.C. (2004). CFD Simulation of Liquid Film Flow on Inclined Plates. *Chem. Eng. Technol*., 27(10):1099-1104.

Gupta, A.V.S.S.K.S. and Nag, P.K. (2000), Prediction of Heat Transfer Coefficient in the Cyclone Separator of a CFB. *International Journal of Energy Research*, 24:1065-1079.

Haglund, J.S. and McFarland, A.R. (2004). A Circumferential Slot Virtual Impactor. *Aerosol Sci. Technol*, 38:664-674.

Han, R., and Moss, O R. (1997). Flow Visualization Inside a Water Model Virtual Impactor. *J. Aerosol Sci.* 28:1005–1014.

Hari, S. (2003). *Computational Fluid Dynamics (CFD) Simulations of Dilute Fluid-Particle Flows in Aerosol Concentrators*. Ph.D. Dissertation, Department of Nuclear Engineering, Texas A&M University, College Station, TX.

Hari, S., Hassan, Y.A., and McFarland, A.R. (2005). Computational Fluid Dynamics Simulation of a Rectangular Slot Real Impactor's Performance. *Nuclear Engineering and Design*. 235:1015-1028.

Hari, S., Hassan, Y.A., and McFarland, A.R. (2006). Optimization Studies on a Slot Virtual Impactor. *Particulate Sci. Technol*. 24:105-136.

Hinds, W.C. (1999). *Aerosol Technology, Properties, Behavior, and Measurement of Airborne Particles*. 2nd Edition. John Wiley & Sons, New York, NY.

Hoekstra, A.J., Derksen, J.J., and Van Den Akker H.E.A (1999). An Experimental and Numerical Study of Turbulent Swirling Flow in Gas Cyclones. *Chem. Engr*., 54(5):2055-2065.

Huang, C.H. and Tsai, C.J. (2002). Influence of Impaction Plate Diameter and Particle Density on the Collection Efficiency of Round-Nozzle Inertial Impactors. *Aerosol Sci. Technol*, 36:714-720.

Jasuja, A.K. (1979). Atomization of Crude and Residual Fuel Oils. *ASME J. Eng. Power*, 101(2):250-258.

John, W. (1999). A Simple Deviation of the Cutpoint of an Impactor. *J. Aerosol Sci.* 30(10):317-1320.

Kenny, L.C. and Gussman, R.A. (2000). A Direct Approach to the Design of Cyclones for Aerosol-Monitoring Applications. *J. Aerosol Sci.*, 31:1407-1420.

Kim, D.S., Lee, K.W. and Kim, Y.J. (2006). Characterization of a Particle Trap Impactor. *J.Aerosol Sci.* 37:1016-1023.

Kim, C.H. and Lee, J.W. (2001). A New Collection Efficiency Model for Small Cyclones Considering the Boundary-Layer Effect. *J. Aerosol Sci.*, 32:251-269.

Lapple, C.E. (1951). Processes Use Many Collector Types. *Chem. Engr.*, 58(5):144-151.

Lefebvre, A.H. (1989), *Atomization and Sprays*, Hemisphere Publishing Corporation, New York, NY.

Lin, Y.L., Shih, T.I.-P., and Stephens, M.A. (2001). A Numerical Study of Flow and Heat Transfer in a Smooth and Ribbed U-Duct with and without Rotation, *Journal of Heat Transfer*, Vol. 123 (2):219-232.

Liu, B. Y. H. and Aganval, J. K. (1974). Experimental Observation of Aerosol Deposition in Turbulent Flow, *J. Aerosol Sci.* 5, 145-155.

Loo, B.W., and Cork, C.P. (1988). Development of High Efficiency Virtual Impactors, *Aerosol Sci. Technol.* 9:167–176.

Marple, V.A. and Liu, B.Y.H. (1974). Characteristics of Laminar Jet Impactors. *Environ. Sci. Technol.* 8:648-654.

Marple, V.A., and Chien, C.M. (1980). Virtual Impactors: A Theoretical Study, *Environ. Sci. Technol.* 14:976–985.

Masuda, H., Hochrainer, D., and Stober, W. (1979). An Improved Virtual Impactor for Particle Classification and Generation of Test Aerosols with Narrow Size Distributions. *J. Aerosol Sci.* 10:275–287.

Matida, E.A., Finlay, W.H., Lange, C.F., Grgic, B. (2004). Improved Numerical Simulation of Aerosol Deposition in an Idealized Mouth-Throat. *J. Aerosol Sci.* 35:1-19.

Mathur, S.R. and Murthy, J.Y. (1997). A Pressure-Based Method for Unstructured Meshes. *Numerical Heat Transfer*, Part B, 31:195-215.

McFarland, A.R. and Ortiz C.A. (1982). A 10um Cutpoint Ambient Aerosol Sampling Inlet. *Atmosphere Environment*. 16(12):2959-2965.

Mills, A.F. (1999). *Heat Transfer*. 2nd Edition. Prentice Hall, Upper Saddle River, New Jersey.

Moncla, B.W. (2005). *A Study of Bioaerosol Sampling Cyclones*. M.S. Thesis, Department of Mechanical Engineering, Texas A&M University, College Station, TX.

Moore, M.E. and McFarland, A.R. (1990). Design of Stairmand-Type Sampling Cyclones. *Am. Ind. Hyg. Assoc. J.,* 51(3):151-159.

Moore, M.E. and McFarland, A.R. (1993). Performance Modeling of Single-Inlet Aerosol Sampling Cyclones. *Environ. Sci. Technol,* 27:1842-1848.

Patankar, S.V. (1980). *Numerical Heat Transfer and Fluid Flow.* Hemisphere, Washington, D.C.

Peters, T.M., Vanderpool, R.W., and Wiener, R.W. (2001). Design and Calibration of EPA PM2.5 Well Impactor Ninety-six (WINS), *Aerosol Sci. Technol.*, 34:389-397.

Petukhov, B.S. (1970). Heat Transfer and Friction in Turbulent Pipe Flow with Variable Physical Properties, *Advances in Heat Transfer*, Vol. 6., J. P. Hartnett and T. F. Irvine, eds., Academic Press, New York.

Shirolkar, J.S., Coimbra, C.F.M., and McQuay, M.Q. (1996). Fundamental Aspects of Modeling Turbulent Particles Dispersion in Dilute Flows. *Prog. Energy Combust. Sci.* 22:363-399.

Vandoormaal, J.P. and Raithby, G.D. (1984). Enhancements of the SIMPLE Method for Predicting Incompressible Fluid Flows. *Numer. Heat Transfer*, 7:147-163.

Wang, J.J., Wang, L.Z., and Liu, C.W. (2005). Effect of a Stick on the Gas Turbulence Structure in a Cyclone Separator. *Aerosol Sci*. T*echnol*, 39:713–721.

Wang, Q., Squires, K.D., Chen, M., and McLaughlin, J.B. (1997). On the Role of the Lift Force in Turbulence Simulations of Particle Deposition, *Int. J. Multiphase Flow,* 23(4):749-763.

Whitaker, S. (1972). Forced Convection Heat Transfer Correlations for Flow in Pipes, Past Flat Plates, Single Cylinders, Single Spheres, and for Flow in Packed Beds and Tube Bundles, *AIChE Journal*, 18:361-371.

Yang, H.T., Chen, H.C., and Han, J.C. (2006). Turbine Rotor with Various Tip Configurations Flow and Heat Transfer Prediction, *Journal of Thermophysics and Heat Transfer*, 20(1):80-91.

Zhu, Y., and Lee, K.W. (1999). Experimental Study on Small Cyclones Operation at High Flow Rates. *J. Aerosol Sci.* 30:1303-1315.

VITA

Shishan Hu, third son of Xinfu Hu and Xiulan Luo, was born on March 25, 1971 in Jiangsu Province, China. Graduated from Yangzhou High School in 1989, he was accepted by Tsinghua University, Beijing, China. He spent five years in the Thermal Engineering Department and received a Bachelor of Science degree in 1994. As a joint-education graduate student at Tsinghua University and Shantou University, he received his Master of Science degree in 1997, focusing on the optimum design of wind turbines. He then worked at the Instrument and Control (I&C) Department of the East China Electrical Power Design Institute (ECEPDI) and became a project engineer and manager focusing on fossil power plant design and research. In September 2003 he enrolled in the Department of Mechanical Engineering at Texas A&M University, where he pursued a Ph.D. with a specialty in aerosol mechanics. His dissertation was supervised by Dr. Andrew R. McFarland, and he received his Ph.D. in May 2007.

His research interests include CFD and experimental studies on aerosol sampling, concentration, and transportation. He has used FLUENT and Gambit to study the particle behaviors in laminar and turbulent flows. His studies on particle behavior encompass devices and systems for bioaerosol sampling including sampling probes, inlets, inline impactors, compound impactors, cyclones, and circumferential slot virtual impactors.

Dr. Hu's permanent address is: Room 702, No. 8, Lane 947, Meichuan Road, Shanghai 200333, China.